IMPROVEMENT TO THE TWO-PHASE MODELING OF ANNULAR FLOWS IN CTF

REFINEMENT AND TESTING OF CTF FOR ANNULAR FLOW REGIME AND INCORPORATION OF FLUID PROPERTIES

BY

USAMA SHAHID, B.Sc., UNENE Graduate Diploma

A THESIS

SUBMITTED TO THE DEPARTMENT OF ENGINEERING PHYSICS

AND THE SCHOOL OF GRADUATE STUDIES

OF MCMASTER UNIVERSITY

IN PARTIAL FULFILMENT OF THE REQUIREMENTS

FOR THE DEGREE OF

MASTER OF APPLIED SCIENCE

TITLE:	REFINEMENT AND TESTING OF CTF FOR ANNULAR FLOW REGIME AND INCORPORATION OF FLUID PROPERTIES
AUTHOR:	Usama Shahid McMaster University, Hamilton, Canada
SUPERVISOR:	Dr. **David R. Novog**
PAGES:	iv – 91

Lay Abstract

COBRA-TF (CTF) is a thermalhydraulic code, based on the historical code COBRA-TF, used for subchannel analysis of nuclear power reactors. Subchannel analysis can be used to predict the local fuel temperatures and coolant conditions inside a complex nuclear fuel assembly. CTF is a transient code which simultaneously solves conservation equations for mass, momentum, and energy for the three coolant phases present, i.e. vapor, continuous liquid, and entrained liquid droplet phases.

The scope of the current study includes 1) testing the code for conditions relevant to CANDU accident analysis, 2) refinement of the models that are used in two-phase interfacial friction calculations, and 3) inclusion of alternate fluid properties. The testing of CTF is performed with different experimental databases covering CANDU thermalhydraulic conditions. The refinement is done by improving the pressure drop prediction in the annular flow regime by using different interfacial friction factor correlations from earlier studies in the literature. The current CTF version includes water and liquid salt properties (FLiBe) for coolant fluids. Freon (R-134a) fluid properties have been added in CTF in order to broaden the testing range of CTF for different experimental database using R-134a as working fluid.

Abstract

The current study focuses on improving and testing the CTF thermalhydraulics computer code. CTF is a thermalhydraulic code used for subchannel analysis of nuclear power reactors developed as part of the US DOE CASL program and distributed by North Carolina State University. Subchannel analyses are used to predict the local fuel temperatures and coolant conditions inside a complex nuclear fuel assembly. Such calculations are used to improve designs of nuclear fuel, improve operating margins, or perform safety analysis. An important part of the code development process is the verification and validation for its intended use. In this work validation activities are performed using the RISO experiments are modeled in CTF for adiabatic and diabatic cases in annular flow regimes and a limited set of tests in CANDU geometries. The CTF predictions significantly overpredicted the pressure drop for cases involving annular flow conditions. Depending on the application, such overprediction can result in significant errors in the computation of fuel element dryout and other figures of merit. For example, an analysis using fixed pressure boundary conditions CTF predicts much lower subchannel flows and hence fuel element temperatures may be overestimated. On the other hand, for a scenario with mass flux and inlet pressure as boundary conditions, the impact of pressure drop discrepancies on dryout predictions may be lower. Therefore, there is a particular focus in this thesis on the two-phase pressure drop models and the RISO experiment specifically, since the RISO tests involve a range of annular flow conditions which is prototypical of many CANDU accident analysis conditions.

In addition to the RISO experiments, 28-element CANDU full scale rod bundle experiments are modeled in CTF for single-phase and two-phase flow conditions. Cases are modeled for crept and uncrept conditions with different bearing pad heights i.e., 1.17 mm and 1.35mm. Pressure drop predictions are compared with the experimental results where single-phase comparisons are in

good agreement while an overprediction of ~25% is observed for two-phase conditions. The effect of bearing pads on the subchannel local parameters, like mass flow rate, are also studied. Furthermore, the effect of turbulent mixing rate on subchannel enthalpy distribution in the bundle and CHF in different subchannels is also analyzed.

Based on the comparison to the RISO and CANDU 28 element test databases, the overprediction of pressure drop in the annular flow regime needs improvement in the current version of CTF. This overprediction of the frictional pressure drop results from either wall drag or interfacial shear stress phenomena. In this study, it is demonstrated that the issue occurs mostly as a result of interfacial friction factor modelling this work examines several alternative approaches. The results show the Ju's and Sun's interfacial friction factor better predicts the results among all the other six correlations implemented in CTF.

The major impediment in further testing of CTF is that it lacks the capability to simulate R-134a fluids. Given there is a large database of R-134a two-phase tests, another aspect of this thesis is to extend CTF for application and validation using refrigerants. The current CTF version only supports fluid properties for water and FLiBe salts. By adding R-134a fluid properties the testing and validation range of CTF is broadened for different experiments performed using R-134a fluids. CHF experiments are modeled in CTF and results are compared with experimental data. For local conditions correlation, 2006 water LUT are used to predict CHF and DNBR. The fluid-to-fluid scaling method is applied in CTF when using CTF with R-134a fluid properties for CHF and DNBR predictions to account for the difference in fluid properties between R-134a and the CHF look-up table.

To my parents, brother, and sisters

I am able to achieve all this only because of your support, prayers and guidance

Acknowledgements

I would like to thank my supervisor Prof. Dr. David R. Novog for accepting me as an M.A.Sc student under his supervision and providing his support, feedback, invaluable help and guidance all along my master's research.

I would also like to thank Dr. Agustin Abarca and Dr. Robert Salko for their help and guidance during my research.

Finally, I would like to thank my parents, family members, and friends without their prayers, support and help it would not have been possible.

Table of Contents

List of Tables

List of Figures

Acronyms

ASSERT	**A**dvanced **S**olution of **Subchannel E**quations in **R**eactor **Thermalhydraulic**s
BEIN	**B**undle **E**nthalpy **I**mbalance **N**umber
BWR	**B**oiling **W**ater **R**eactor
CANDU	**CAN**adian **D**eutrium **U**ranium
CATHENA	**C**anadian **A**lgorithm for **Thermalhydraulic N**etwork **A**nalysis
CHF	**C**ritical **H**eat **F**lux
COBRA	**CO**olant **B**oiling in **R**od **A**rrays
CTF	**COBRA**-**T**wo **F**luid
DNBR	**D**eparture from **N**ucleate **B**oiling **R**atio
RELAP	**R**eactor **E**xcursion and **L**eak **A**nalysis **P**rogram
SIMPLE	**S**emi-**I**mplicit **M**ethod for **P**ressure-**L**inked **E**quations
TRACE	**T**RAC/**R**ELAP **A**dvanced **C**omputational **E**ngine

Symbols

A	Void fraction	$\widehat{\varepsilon_k}$	Non dimensional roughness
δ	Film thickness	D	Diameter
ṁ	Mass flow rate	F	Friction factor
m_g^+	Dimensionless liq. Film thickness	Fr	Froude's number
σ	Surface tension	G	Mass flux
τ	Shear stress	K.E	Kinetic Energy
U_{SG}^*	Dimensionless superficial gas velocity	Re	Reynold's number

$N_{\mu f}$	Viscosity number	We	Weber number

Subscripts

Cric	Critical	lf	Liquid film
Fric	Friction	SG	Superficial gas
G	Gas	SL	Superficial liquid
gc	Gas core	spl	Single-phase liquid
H	Hydraulic	spv	Single-phase vapor
I	Interfacial	TP	Two-phase
ISO	Isothermal	v	Vapor
L	Liquid	w	wall

1 Introduction

1.1 Background

CTF is a computational thermalhydraulic code which was originally developed in 1980's by Pacific Northwest Laboratory and evolved from COBRA III-C, COBRA-IV, COBRA-TF and then CTF (Salko, et al., 2019). It uses a time dependent, two-fluid (vapor and liquid), three field (i.e. liquid, entrained droplets, and vapor) modeling approach for subchannel analysis of nuclear power reactors (i.e., it forms a system of 9 coupled partial differential equations). CTF can predict flows, temperatures and other thermalhydraulic parameters within complex nuclear fuel assemblies through the solution of the one-dimensional field equations within each subchannel and additional conservation equation to address lateral transfer of mass, momentum and energy between subchannels.

Recently the code has seen many updates and improvements in its computational performance and prediction accuracy. The Consortium for Advanced Simulation of Light Water Reactors (CASL) energy innovation-hub was established by US DOE in 2010 (CTF21). The main aim of CASL is to address the challenges in modelling of existing nuclear power reactors and in development and preparation of next generation nuclear power reactors. CTF was built from its legacy COBRA-TF; and is adapted in CASL with numerous improvements. These improvements include implementation of new closure models in support of CASL challenge problems, extensive verification and testing of the codes and numerical refinements. Furthermore, coupling of neutron transport codes such as MPACT, MAMBA, and the fuel performance code BISON, etc., parallelization of codes using message-passing interface (MPI), and integration into VERA environment were added to CTF. However, there are still certain areas which need improvements

for more accurate prediction, one of which is CTF's pressure drop prediction in the annular flow regime.

In CTF, conservation equations are solved for mass, momentum, and energy for each of the three coolant fields and for each subchannel. A subchannel is defined as the coolant flow area between fuel rods, bounded by rods and the imaginary lines linking adjacent rod centers (Carver, et al., 1995). A subchannel view is shown below in Figure 1-1.

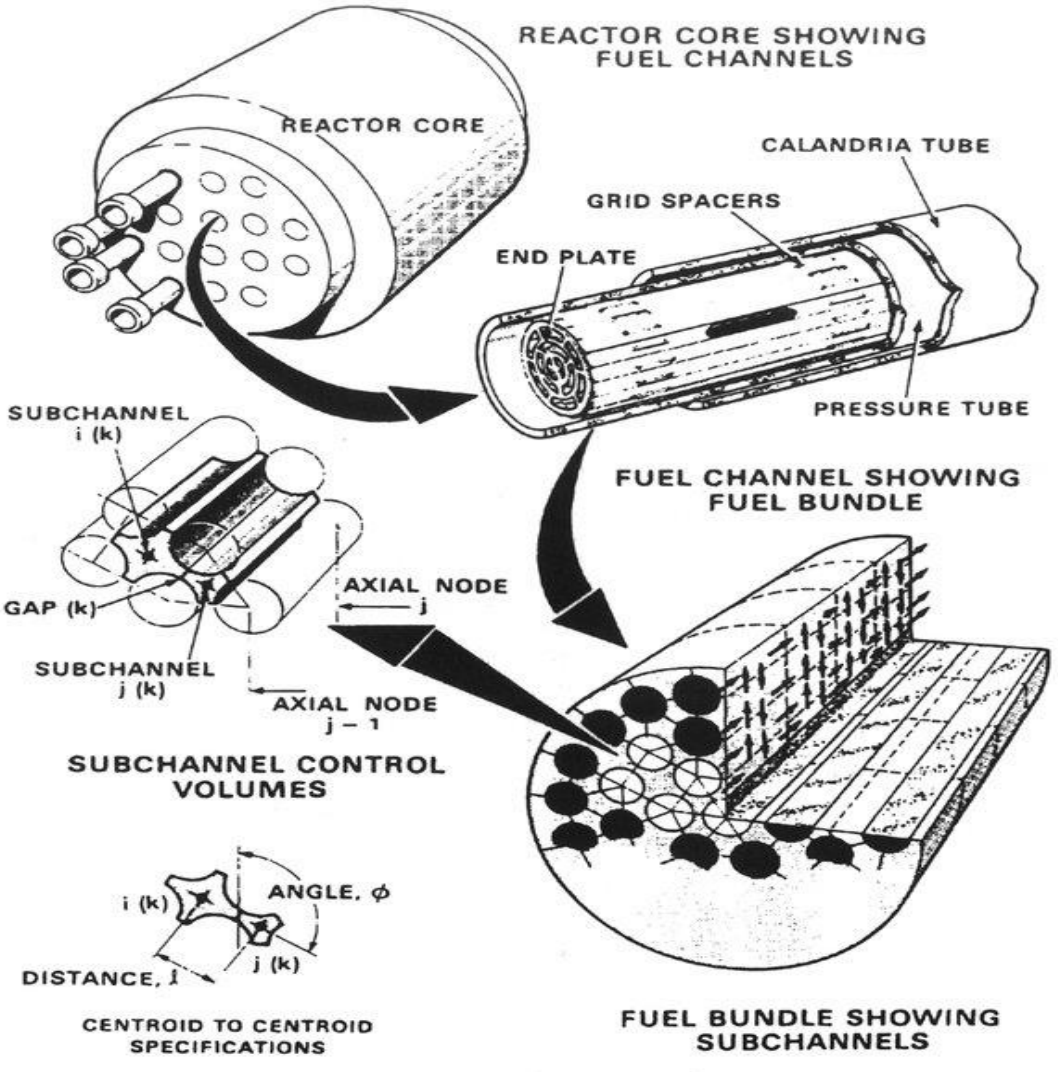

Figure 1-1 Definition of subchannel geometry in a CANDU reactor *(Carver, et al., 1995)*

Depending on the reactor designs (PWR, BWR and CANDU), the coolant (light water, heavy water) under normal operating condition can either be in single-phase or two-phase flow. The heat transfer from fuel to coolant is sufficient to ensure that fuel cladding temperature remains acceptable and is generally greater than the coolant temperature by 10s of Centigrade. During accidents changes in coolant conditions and fuel power may cause the surface heat flux to exceed the critical heat flux (CHF) which can cause high fuel sheath temperatures and a possible fuel sheath failure. CHF phenomena are therefore an important aspect of thermalhydraulic calculations and are in-turn dependent on aspects such as mass flow rate, local quality and pressure. The prediction of these local parameters is dependent on the flow regime within the furl channel. The annular flow regime is of particular importance to CANDU reactors since it is most likely to occur under various accident scenarios.

In the annular flow regime, the fuel sheath is covered with continuous liquid film while the vapor flows in the core (center) of the tube (Wallis, 1969). The liquid-vapor interface may either be smooth or rough depending on the flow conditions. For low film to vapor relative velocity conditions the interface may be relatively smooth. With sufficient liquid to core velocity differences instabilities may develop at the interface causing wave formation and making the interface more complex. At high gas-core velocities, the vapor may shear off some of these waves hence introducing entrained droplets in the vapor core. Such a flow regime is called annular/mist flow regime.

1.2 Flow regimes

In two-phase flow theory, when two-phase liquid and vapor flow simultaneously in a pipe, different flow regimes occur. Typically there are approximately 7 different flow regimes. These flow regimes are highly dependent on fluid properties, hydraulic diameter, liquid-vapor mass flow

rates and orientation/geometry of the test section. Experimental and visual studies have also shown that the dependence of flow regimes also lies on the test section's inlet conditions (e.g., can depend of the presence of flow obstructions, elbows, etc. in addition to the parameters discussed previously). There is a large body of literature on empirical and physical based flow regime models, the review below provide a cross section of the available works

(Holland, et al., 1995) has presented different flow regimes in vertical, upward, concurrent liquid-vapor flows. While many authors have reported studies on flow regime transitions, the description of Holland is used here for brevity.

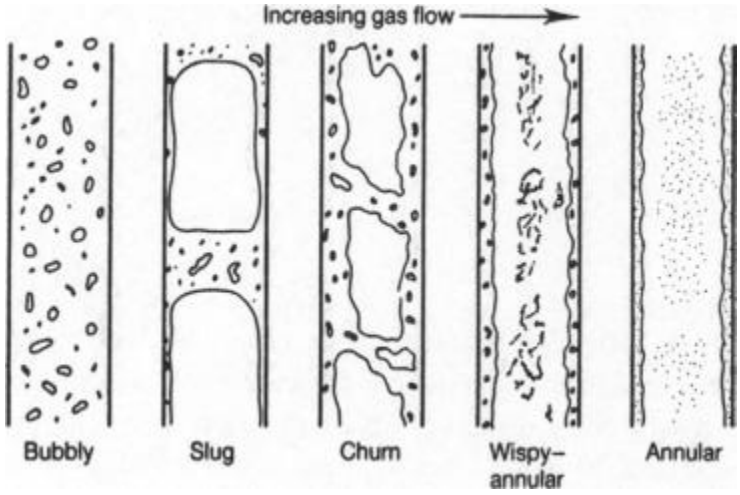

Figure 1-2 Flow regimes in vertical liquid-gas flow *(Holland, et al., 1995)*

Figure 1-2 shows the sequence of flow regimes visually observed by increasing the gas-to-liquid flow rate ratio.

In the bubbly flow regime, which occurs for flows at low superficial gas velocities or void fractions, vapor bubbles of variable sizes are distributed along the flow length. For larger void fractions or gas superficial velocities these bubbles will coalesce together to form larger bubbles. Such a flow regime is called slug flow. The flow pattern transition from slug to churn flow may

occur either by increasing vapor flow rate (adiabatic conditions) or by continuous formation of large bubbles (i.e. diabatic conditions), which cause the formation of vapor bubbles within the liquid slugs along with liquid/droplet entrainment in the gas bubbles. This flow is also mentioned as chaotic flow by (Holland, et al., 1995) since there is increased agitation of the liquid and gas phases. Upon further increasing the gas flow rates, the initiation of phase separation occurs. During this phase separation, the liquid flows on the solid surfaces while vapor flows as the vapor core. As a result of the phase separation there is considerable slip between the phasic velocities. This flow topology is called annular flow. At still higher vapor relative velocities, waves are formed on the liquid film. Due to high vapor core velocities, the shearing off of waves leads to an entrainment process. As a result, these entrained liquid droplets flow in the vapor core which is often referred to as annular-mist flow. The focus of this thesis is primarily on annular and annular-mist flows since they are an important flow regime in CANDU safety assessments.

1.3 Annular flow regime

(Wallis, 1969) describes annular flow as liquid film which flows on the channel walls whereas gas flows in the core or central region of the channel. The liquid film thickness in annular flow is a strong function of the ratio of liquid film to gas core mass flow rate. In diabatic annular flows the phase change process occurs primarily at the interface between the liquid film and gas core because often the liquid film is very thin and conduction through this thin film prevents sufficient superheat required for nucleation (thus preventing nucleation). In some circumstances such as thicker liquid films or liquid with low thermal conductivity, nucleation may also be observed in liquid film as a result of nucleate boiling (Zeigarnik, 2011). This phenomenon is rare, or limited to the initial locations where annular flow originates (where the liquid film is thickest) because the liquid film becomes so thin that the liquid evaporates from interface without nucleation.

The visual representation of annular flow regime is shown in Figure 1-3.

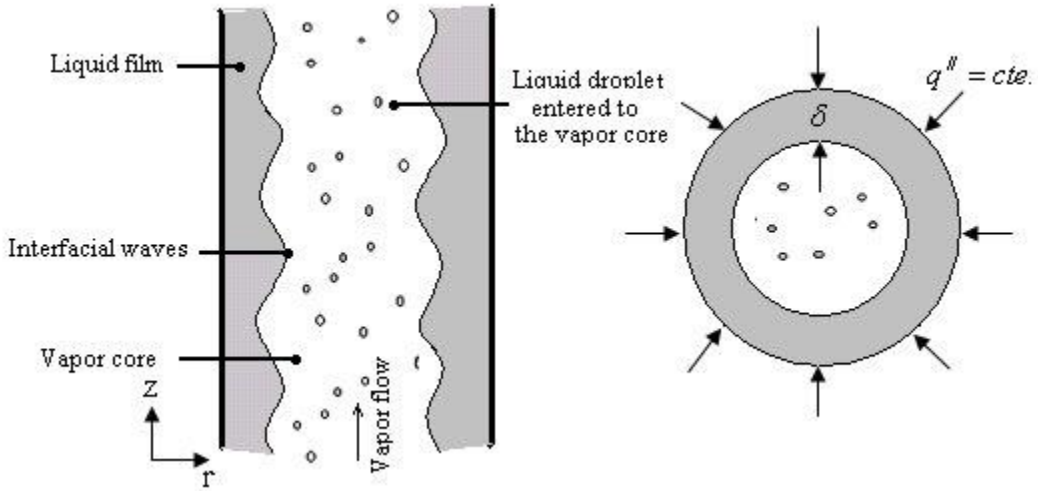

Figure 1-3 Schematic of annular regime of two-phase flow *(Baniamerian, et al., 2012)*

In vertical concurrent flows, the film thickness can be uniform. But in case of horizontal flows, the film thickness may be non-uniform due to gravity. During the boiling process, the evaporation at liquid-vapor interface acts to deplete the liquid film causing it to become thinner as it progresses down the channel. For annular flow with no interfacial waves or entrainment, the velocity profile in the vapor core obeys the logarithmic law (Zeigarnik, 2011) while for a droplet rich core the velocity profile can significantly deviate from the log-law relationship.

Annular flow occurs in oil-gas pipelines, chemical plants, nuclear power reactors, steam generators and in many other two-phase industrial applications. In the nuclear field, annular flow occurs primarily in BWR and CANDU type reactors. At different combinations of thermalhydraulic parameters such as pressure, linear heat rate, mass flow rate, enthalpy etc., the liquid film thickness becomes very thin such that continuous liquid contact at the surface cannot be maintained. Once the local heat flux exceeds the critical heat flux, this leads to the phenomena of 'dryout' since there insufficient liquid and the surface gets exposed to steam core conditions. This annular film dryout

occurs at high qualities and at corresponding lower wall heat fluxes than Departure from Nucleate Boiling (DNB). At the onset of dryout, the heat transfer from fuel sheath to coolant reduces which causes an increase in fuel element temperature. If the temperature becomes significantly high the fuel sheath surrounding the fuel element may undergo oxidation or bundle structural brazing may fail. If the fuel element remains in dryout for a prolonged period of time, or if the temperature become excessive, then the fuel sheath may fail. Thus predicting the occurrence of dryout in complex fuel geometries is an important part of safety analysis.

1.4 Motivation

From the beginning of 20^{th} century the world has seen great accomplishments in the field of science, medicine and technology. With every passing day the pace of human achievements is sky rocketing. In order to continue these advancements we need to fulfill our energy needs in the most economic, safest, and climate-friendly manner. Among all the current alternatives, nuclear power is the one which fits the best since it can reliably produce large amounts of energy over a long period of time with very small carbon footprint. Given the importance of safety to nuclear power there has been, and continues to be, large international efforts to enhance knowledge related to nuclear power plant phenomena.

The prime focus of nuclear reactor designers and operators is to maintain the integrity of the radiation barriers that protect the public from radioactivity contained in the fuel. The primary barriers towards radiation protections are the;

1) Fuel element UO_2 solid matrix which contains most of the fission products and would need to be damaged to cause significant release.

2) Fuel sheath which is a sealed boundary around the fuel which prevent radionuclides from escaping.
3) Pressure boundary of the primary heat transport system which is sealed and hence prevents any radio-nuclides that might escape the first two barriers from being released.
4) Containment which prevents or reduces any radioactive release to the environment.
5) Exclusion zone which provided a safe distance for radio-nuclides to disperse and reduce the concentrations to acceptable levels and is important for cases when all other physical barriers have failed.

These radiation barriers help to contain fission products from being released to the surroundings. Therefore, a sufficient but not necessary criterion to limit dose to the public is to maintain the fuel and sheath barriers. To ensure fuel sheath integrity, one needs to demonstrate adequate cooling of fuel element and thus preventing dryout is one approach to ensure fuel sheath integrity.

There are different computational codes currently used to simulate nuclear power reactor transients and to accurately predict the parameters in focus. CTF is one of those computational codes used for thermalhydraulic subchannel analysis of nuclear reactors. In order to improve and validate CTF, the code results are compared with different experimental databases. Past experience with CTF suggests that in the annular flow regime it significantly overestimates the pressure drop and hence it can lead to significant uncertainties in the prediction of dryout. The improvement in annular flow pressure drop prediction is important for analyzing CANDU transients. Furthermore, adding more options for fluids, like R-134a, in CTF will broaden the testing and validation opportunities.

2 Literature Review

2.1 CTF theory

The current version of CTF is based on a two-fluid model, which takes into account three separate fluid fields i.e. liquid, entrained droplets and vapor (Salko, et al., 2019). Hence, CTF is categorized as a three-field, two-fluid, and one-dimensional subchannel thermalhydraulics code. Thus CTF solves the conservation equations for mass, momentum, and energy for each of the three coolant fields in the axial direction. While the code uses a one-dimensional formulation, it accounts for the differences laterally across the assembly by solving the flows in each subchannel separately along with lateral transfer equations. The liquid and entrained droplet fields share the same energy conservation equation as they are assumed to be in thermal equilibrium. The conservation equations are concurrently solved using the Semi-Implicit Method for Pressure Linked Equations (SIMPLE) (Salko, et al., 2019). The general momentum conservation equation defined in CTF is given below:

$$\frac{\partial}{\partial t}\left(\alpha_k \rho_k \overrightarrow{V_k}\right) + \frac{\partial}{\partial x}\left(\alpha_k \rho_k u_k \overrightarrow{V_k}\right) + \frac{\partial}{\partial y}\left(\alpha_k \rho_k u_k \overrightarrow{V_k}\right) + \frac{\partial}{\partial z}\left(\alpha_k \rho_k w_k \overrightarrow{V_k}\right) = \alpha_k \rho_k \vec{g} - \alpha_k \nabla P + \nabla.\left[\alpha_k\left(\tau_k^{ij} + T_k^{ij}\right)\right] + \vec{M}_k^L + \vec{M}_k^d + \vec{M}_k^T \quad (1)$$

The L.H.S of momentum conservation equation represents the time rate of change of momentum, and momentum advection terms. While the R.H.S represents gravitational force, pressure force, viscous shear stress and turbulent shear stress, momentum source/sink due to phase change and entrainment, interfacial drag forces, and momentum transfer due to turbulent mixing terms (Salko, et al., 2019) whereas, the turbulent shear stress term is not modeled in CTF. Mass conservation equations are used as a pressure-corrector method as part of the typical SIMPLE algorithm.

One of the aims of this thesis is to improve the accuracy in pressure drop prediction for annular flow regime. Via several investigations of single-phase flows, it was determined that the fluid-to-wall shear stress were generally predicted well (Zhao, et al., 2017). Hence, the focus is on interfacial drag term prediction accuracy. This phenomenon is considered in the momentum equation of each coolant field. The wall shear stress and interfacial drag terms as defined in CTF are explained below.

The wall shear stress comprises of frictional and form loss models.

$$\tau_{w,x} = k_{w,x}\, \dot{m} \Delta X \tag{2}$$

Where '$\dot{m}$' is the coolant field mass flow rate (ML^{-1}), '$k_{w,x}$' is the wall drag coefficient. The wall drag coefficient is defined as:

$$k_{w,x} = \left(\frac{dP}{dX}\right)_{fric} \frac{1}{\dot{m}} + \left(\frac{dP}{dX}\right)_{form} \frac{1}{\dot{m}} \tag{3}$$

The frictional pressure drop in CTF is calculated as; (Wallis, 1969);

$$\left(\frac{dP}{dX}\right)_{fric,x} = \frac{f_w G_x^2}{2 D_h \rho} \emptyset^2 \tag{4}$$

$$\emptyset = \begin{Bmatrix} 1/\alpha_l & for\ normal\ wall\ cond. \\ 1/\alpha_v & for\ hot\ wall\ cond. \end{Bmatrix} \tag{5}$$

Where G_x, D_h, ρ represents field mass flux ($ML^{-1}T^{-2}$), hydraulic diameter (L), and field density (ML^{-3}) respectively. 'f_w' represents wall friction factors and is defined in terms of Reynold's number and surface roughness. Table 2-1 shows different friction factor correlations options in CTF. The term '$\emptyset$' is the two-phase multiplier. The two-phase multiplier in Eq. 5 is defined based

on Wallis work (Wallis, 1969). There are four different wall friction factor correlations and one user defined correlation in CTF which will allow the user to select any of the above options.

Table 2-1 CTF friction factor correlations *(Salko, et al., 2019)*

Input deck option	**Correlation Name**	**Correlation**
1	Original correlation	$f_w = max\begin{cases} 64.0/Re & ,Laminar \\ \max(1.691Re^{-0.43}, 0.117Re^{-0.14}) & ,Turbulent \end{cases}$
2	McAdam's correlation	$f_w = max\begin{cases} 64.0/Re & ,Laminar \\ 0.204Re^{-0.2} & ,Turbulent \end{cases}$
3	Zigrang-Sylvester correlation	$f_w = max\left\{\left(-2.0log\left(\frac{\varepsilon}{3.7D}+\frac{2.51}{Re}\left[1.14-2log\left(\frac{\varepsilon}{D}+\frac{21.25}{Re^{0.9}}\right)\right]\right)\right)^{-2}, 64.0/Re\,, Laminar, Tu$
4	Churchill correlation	$f_f = 2\left[\left(\frac{8}{Re}\right)^{12}+\frac{1}{(a+b)^{\frac{3}{2}}}\right]^{1/12}$ Where, $a = \left(2.475ln\left[\frac{1}{\left(\frac{7}{Re}\right)^{0.9}+0.27\left(\frac{\varepsilon}{D}\right)}\right]\right)^{16}$ $b = \left(\frac{3.753x10^4}{Re}\right)^{16}$
5	User defined	$f_w = max\begin{cases} 64.0/Re & ,Laminar \\ A+BRe^C & ,Turbulent \end{cases}$

Where in option 5, A, B, and C are user defined coefficients.

The wall friction factor correlations are not flow regime dependent, while most of the interfacial drag models and interfacial heat transfer models are flow regime dependent. In CTF, the flow

regime maps are divided into two different types; 'normal wall' map and 'hot wall' map. During normal wall map, when $T_w < T_{CHF}$, the liquid phase contributes all the wall drag unless the void fraction is very high (i.e. the wall shear stress is dominated by liquid as it is touching the solid wall surface). However, for hot wall map, $T_w > T_{CHF}$, all the wall drag is attributed to the vapor phase. To accomplish such behavior in the code, the wall drag loss coefficients are multiplied with multiplication factors, F_l and F_v for liquid and vapor phase respectively. The multiplication factors F_l and F_v are defined in CTF as:

$$F_l = \begin{cases} (1 - F_{spv}) & Normal\ wall\ regimes \\ F_{spl} & Hot\ wall\ regimes \end{cases} \tag{6}$$

$$F_v = \begin{cases} F_{spv} & Normal\ wall\ regimes \\ (1 - F_{spl}) & Hot\ wall\ regimes \end{cases} \tag{7}$$

Where F_{spv} and F_{spl} are calculated as:

$$F_{spv} = max\left\{ min\left\{ \frac{\alpha_v - 0.9990}{0.9999 - 0.9990}, \begin{matrix} 1.0 \\ 0.0 \end{matrix} \right. \right. \tag{8}$$

$$F_{spl} = max\left\{ min\left\{ \frac{\alpha_v - 0.001}{0.0001 - 0.001}, \begin{matrix} 1.0 \\ 0.0 \end{matrix} \right. \right. \tag{9}$$

The flow regime selection logic in CTF, which is largely driven by void fraction is shown in Figure 2-1.

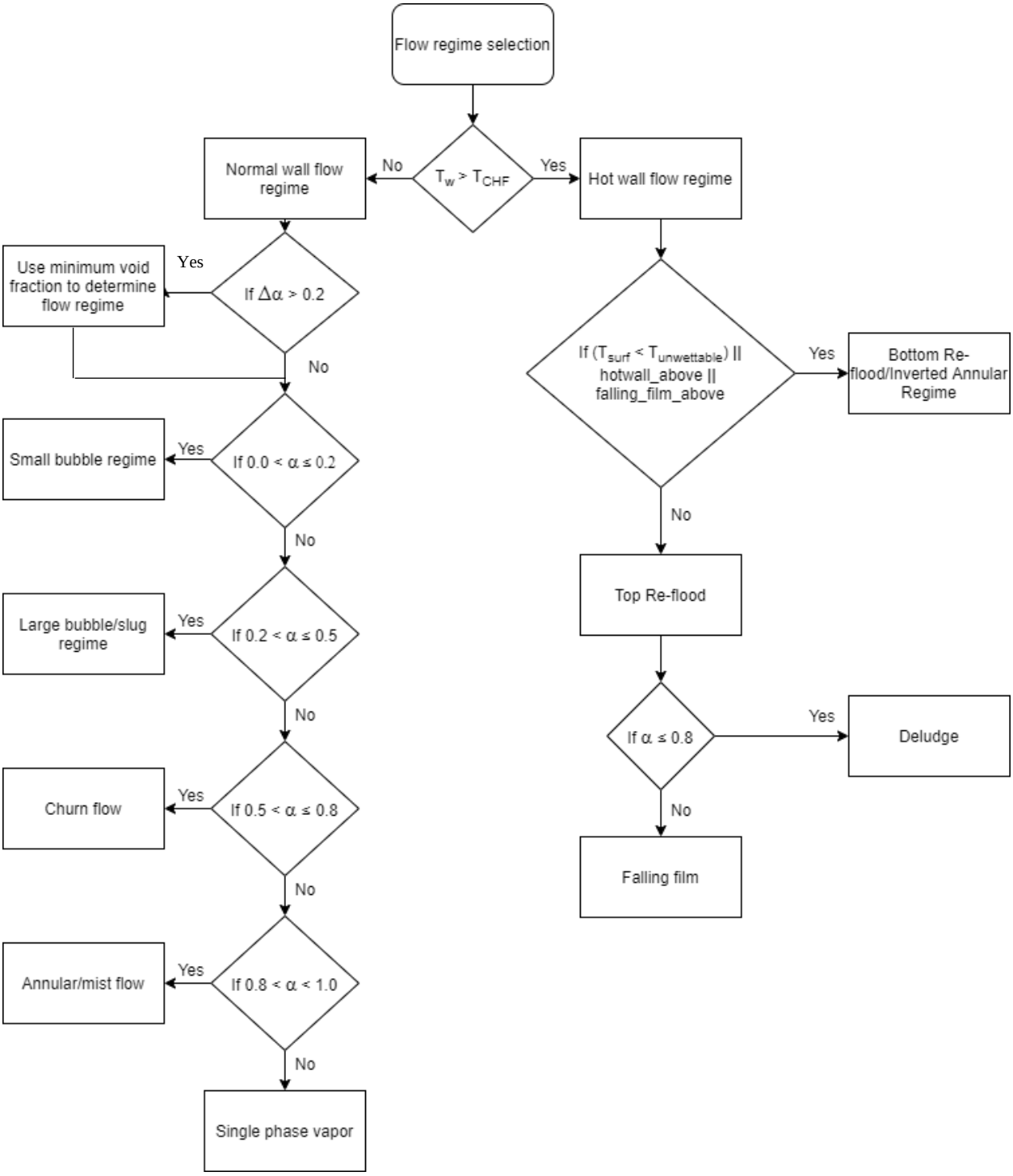

Figure 2-1 Flow regime selection logic in CTF

The flow regime selection logic is modeled in CTF module '**INTFR.f90**'.

Liquid film thickness determination, entrainment and de-entrainment (i.e., deposition) are major phenomena affecting the interfacial shear stress which, in turn, determines the pressure gradient in the annular flow regime. In CTF, the liquid film thickness is computed from the solution of the continuous liquid field and using the geometric dimensions and the calculated liquid volume fraction. However, this computation assumes that the liquid film is uniformly distributed around the wall. This assumption is reasonable for flows in circular/symmetrical flow area, whereas it becomes unreasonable for non-circular flow paths or where gravity driven asymmetries are significant. The liquid film thickness is calculated as:

$$\bar{\delta} = \frac{D_H}{4}\alpha_l \tag{10}$$

In calculation of liquid film interfacial area, the vapor core is assumed to be cylindrical in shape. The interfacial area for liquid film is calculated as:

$$A_{i,f} = \frac{4\sqrt{\alpha_v + \alpha_e}A_x\Delta X}{D_h} \tag{11}$$

The annular/mist region may or may not contain entrained droplets in vapor core. In CTF, the entrained droplet diameter is calculated using the droplet interfacial area, which is calculated using the interfacial area transport equation in the POST3D subroutine. Droplet diameter is calculated as:

$$D_d = max\begin{cases} \dfrac{6\alpha_e}{A'''_{i,d}} \\ 0.0005\ ft \end{cases} \tag{12}$$

$$A_{i,d} = A'''_{i,d}A_x\Delta X \tag{13}$$

The droplet diameter is used in the calculation of interfacial drag on entrained droplets and to calculate the volumetric addition to the liquid film for deposition. The interfacial area for liquid film and entrained droplet is calculated separately and then summed.

The entrainment process for annular/mist flow regime is calculated for two cases in CTF: entrainment in co-current flow and entrainment in counter-current flow. In both the cases, the phenomenon is the same for entrainment from the liquid film. The model is based on the formulation of waves that are created on liquid film due to hydrodynamic and surface tension forces. Mechanistically the entrainment process occurs when the pressure differential over the waves exceed the surface tension forces. This will cause the waves to break and liquid to be entrained. For counter-current flow, the droplet field will comprise all liquid in excess of a predefined critical liquid flow rate. Most relevant to this thesis is the co-current flow phenomena. The Wurtz dimensionless group is used in CTF for entrainment calculation of co-current flows (Wurtz, 1978).

$$S_E = [0.41\ lbm\ ft^{-2}\ s]\left[\frac{k_s \tau_i \overrightarrow{U_v} \mu_l}{\sigma^2}\right] P_w \Delta X \tag{14}$$

Where $k_s, \tau_i, \overrightarrow{U_v}, \mu_l, \sigma, \Delta X, and\ P_w$ represents roughness parameter, interfacial shear stress, dimensionless velocity, dynamic liquid viscosity, surface tension, cell height and wetted perimeter.

De-entrainment in CTF is defined as the deposition of entrained droplets onto the liquid film. This phenomenon occurs due to the random turbulent motion of droplets in the gas core which causes some of the droplets to impact the liquid film and get deposited. In CTF, the de-entrainment is calculated using the Cousins correlation (Cousins, 1965).

$$S_{DE} = k_0 C P_w \Delta X \tag{15}$$

The droplet concentration, C [ML^{-3}] is calculated as:

$$C = \frac{\alpha_e \rho_l}{\alpha_e + \alpha_v} \tag{16}$$

The mass transfer coefficient, k_0 [$ft\text{-}s^{-1}$], is correlated by Whalley as follows:

$$k_0 = max\begin{cases}3.0492\ X\ 10^{12}\sigma\text{^}5.3054 \\ 12.491\sigma\text{^}0.8968\end{cases} \quad (17)$$

Where surface tension, σ is in units lbf-ft^{-2}.

2.2 Interfacial friction factor in earlier versions

The earlier versions of CTF which are reviewed in this section are COBRA-IIIC/MIT Code, COBRA-IV-PC, and COBRA/TRAC. The intent in this review is to study the evolution of the CTF in general, and the changes to interface modelling specifically. The following is based on open literature and does not include the developments of proprietary versions of COBRA that may be used in industry.

COBRA-IIIC/MIT Code (SLIZ, et al., 1983): The COBRA-IIIC/MIT code solves the finite difference equations of mass, momentum, and energy to calculate flow and enthalpy within interconnected subchannels. The mathematical models may be used for either steady state or transient calculations. Turbulent mixing and diversion crossflows from subchannel to subchannel are accounted for in these models. In formulating the model one-dimensional, two-phase, separated and slip-flow are assumed to exist during boiling (SLIZ, et al., 1983). The void fraction is calculated using the Smith correlation in conjunction with the Levy subcooled model. The pressure drop for single and two-phase flow is calculated using an isothermal friction factor correlation along with viscosity and two-phase friction multipliers correlation. The isothermal friction factor correlation and relationship for its heating effects correction are as follows:

$$f_{ISO} = 0.184Re^{-0.2} \quad (18)$$

$$\frac{f_H}{f_{ISO}} = 1.0 + \frac{Heated\ Perimeter}{Wetted\ Perimeter}\left[\left(\frac{\mu_{wall}}{\mu_{bulk}}\right)^{0.6} - 1.0\right] \quad (19)$$

For two-phase flow conditions, the friction multipliers are calculated using Baroczy two-phase multiplier correlation. These friction multipliers are then used to determine the heated friction factor (f_H).

COBRA/TRAC (Thurgood, et al., 1983): COBRA/TRAC is a computational code that was developed for thermalhydraulic analysis of nuclear reactor for small and large-break loss of coolant (LOCA) accidents. COBRA/TRAC is the result of merging two computational codes; COBRA-TF and TRAC-PD2. COBRA-TF is a subchannel analysis computational code that uses three-dimensional, two-fluid, three-coolant field similar to CTF. Whereas, TRAC-PD2 is a system code which models reactor primary system featuring special models for each component such as accumulator, pumps, valves, pipes, pressurizers, steam generators, and the reactor vessel. Response of all these components, except the reactor vessel internals, is modeled using the five-equation drift flux model in TRAC. The vessel component thermalhydraulic response to transient is modeled using two-fluid, three-field modeling approach in COBRA. Different physical models are modeled in the code for different physical phenomenon such as interfacial drag, interfacial mass transfer, liquid-vapor drag, wall and interfacial heat transfer, entrainment and de-entrainment, and mixing length turbulence model. The interfacial friction factor model is selected based on the stability of the film, i.e., the interfacial friction factor calculation for annular flow is dependent on the stability of the film in annular flow regime. (Wallis, 1970) correlation is used for calculating interfacial friction factor for stable liquid films where as Henstock and Hanratty correlation is being used for calculating friction factor of unstable liquid films (Thurgood, et al., 1983).

COBRA-IV-PC: This is a legacy version of COBRA developed for performing calculations on a PC. In this code version simple two-phase friction multipliers are used for calculating two-phase

pressure drop. The available options include the homogeneous or Armand models pressure drop calculations (Webb, 1976).

2.3 Interfacial friction factor in CTF

The interfacial drag force, in CTF, is defined as the product of empirical coefficient, relative velocities and momentum cell height. The following description is given by Salko, 2019.The interfacial drag for axial direction between liquid and vapor phase is as follows:

$$\tau_{i,vl} = k_{vl,x} U_{vl,x} \Delta X_j \tag{20}$$

Where, $k_{vl,x}, U_{vl,x}, and\ \Delta X_j$ represents drag coefficient, relative velocities, and momentum cell height in Eq. 20.

In annular/mist flow regime, the liquid film flows on the walls with entrained droplets in the vapor core. The film drag coefficient is defined as:

$$k_{vl,x} = \frac{1}{2} f_i \rho_v |u_v - u_l| \frac{A_{ix}}{\Delta X} \tag{21}$$

The interfacial area, A_{ix}, is used to calculate the drag on the liquid film. In CTF, geometry is considered to be cylindrical for interfacial area calculations. The interfacial area is calculated by Eq. 11 and Eq. 13.

In CTF the calculation of interfacial friction factor is dependent on the stability of the film, similar to the COBRA predecessors. The pressure drop and interfacial friction factor for unstable liquid film are significantly larger than that for stable liquid films. This is due to the wave formation on liquid film which leads to the increase in liquid film interfacial roughness. The parameters for defining the stable liquid film regime are: liquid void fraction and critical liquid void fraction. The liquid film is unstable when the difference between the liquid and critical liquid void fraction is greater than zero. On the other hand, if the difference is less than or equal to zero, the film is stable.

$$\begin{cases} (\alpha_l - \alpha_{l,crit}) > 0; \;\; Unstable\ film \\ (\alpha_l - \alpha_{l,crit}) \leq 0; \;\; Stable\ film \end{cases}$$

Where $\alpha_{l,crit}$ is calculated as:

$$\alpha_{l,crit} = 2\frac{\sigma}{\rho_v \vec{U}_{vl}^2 D_h} \tag{22}$$

Where $\sigma, \rho_v, \vec{U}_{vl}^2, and \;\; D_h$ represent surface tension, vapor density, relative velocity, and hydraulic diameter in Eq. 22.

Figure 2-2 presents the interfacial friction factor selection logic used in CTF. The stability of the liquid film is determined first. If the film is stable the interface friction, F_i, is based on the Wallis correlation for the axial momentum equations. Whereas, for calculating the unstable film friction factor, F_{iu}, the larger value of either Henstock-Hanratty correlation or five-times the Wallis correlation is used for the solution of vertical momentum equation. However, the Wallis correlation is used to calculate friction factor for both stable and unstable liquid film for solving transverse (lateral subchannel-to-subchannel transfer) momentum equations.

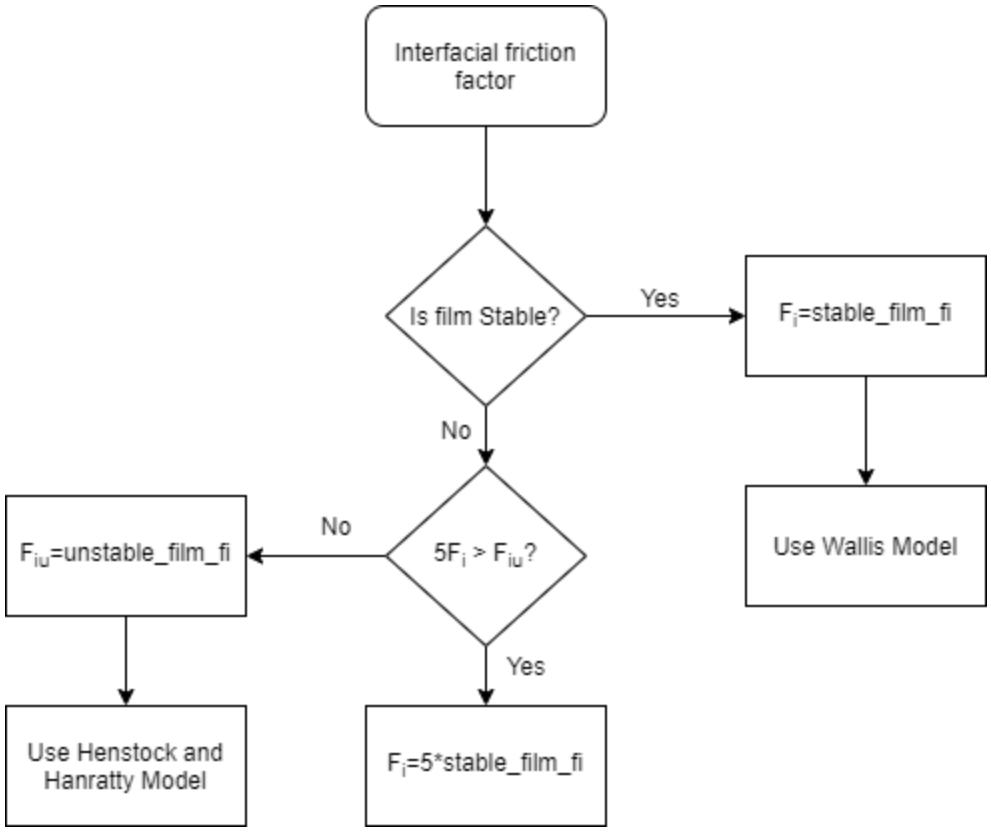

Figure 2-2 Interfacial friction factor calculation logic for vertical momentum equations in CTF

In order to determine the phase change in the continuity/energy conservation equation solution, appropriate interfacial heat transfer terms are used. These equations are solved in the CTF subroutine 'XCHEM'. The interfacial heat transfer coefficient and interfacial heat transfer area are flow regime dependent. In the annular flow regime there may exist two field interfaces which are liquid/vapor and droplet/vapor interfaces. In CTF, interfacial heat transfer coefficients are calculated for these two interfaces and for four different possible cases: 1) Subcooled liquid 2) Superheated liquid 3) Subcooled vapor 4) Superheated vapor. Figure 2-3 shows the interfacial friction factor calculation scheme for film and droplet in annular flow.

Droplet calculations: This calculates the droplet interfacial area, droplet drag force coefficient and droplet interfacial heat transfer coefficient. The interfacial heat transfer coefficient is based on four

different possible scenarios: 1) Subcooled liquid 2) Superheated liquid 3) Subcooled vapor 4) Superheated vapor. The modified Anderson correlation (Anderson correlation (Andersen, 1973) multiply by 2.7) is used for subcooled regimes and the superheated liquid calculations use the modified Lee-Ryley correlation.

Film calculations: This follows the same approach as droplet calculations except that the correlations applied are specific for film flows. The Colburn analogy is used to calculate interfacial heat transfer coefficient for subcooled liquid and subcooled vapor. The approach taken for superheated vapor and liquid is explained below.

Superheated vapor: Colburn analogy is used to calculate the interfacial heat transfer coefficient for superheated vapor. Unlike subcooled liquid case, Wallis (for stable film) and Hanratty (for unstable film) methods are used to determine the friction factors within the heat transfer calculations.

$$h_{i,spv} = f_i \rho_v C_{p,film} \overrightarrow{u_{vl}} Pr^{-2/3} A_{i,film} \quad (23)$$

Where $f_i, \rho_v, C_{p,film}, \overrightarrow{u_{vl}}, Pr, A_{i,film}$ represents interfacial friction factor, vapor density, vapor specific heat capacity at film temperature, vector relative velocity, Prandtl number and film interfacial area respectively.

Superheated liquid: Three possible expression are used to determine interfacial heat transfer coefficient for superheated liquid which are: 1) constant value 2) conduction through the film 3) Colburn analogy using Hughmark correlation for the film friction factor. The minimum value of expression '1' and '2' is selected. This resulting value is compared with expression '3'. The maximum value between them is used for the interfacial heat transfer coefficient. This is mathematically presented as follows:

$$h_{i,shl} = max\left[h_{i,shl,colburn}, min\left(278\,{}^{BTU}/_{ft^2.sec.°\mathrm{F}}, h_{i,shl,cond}\right)\right] \quad (24)$$

Where conductive heat transfer term is defined as:

$$h_{i,shl,cond} = \frac{2k_f}{\delta_l} P_w \Delta X \quad (25)$$

Where k_f and δ_l represent saturated liquid conductivity and liquid film thickness respectively. The Colburn analogy is:

$$h_{i,shl,colburn} = f_{HM}\rho_l C_{p,l}|u_{vl}|Pr^{-2/3}A_{i,film}f_{ai} \quad (26)$$

f_{ai} is multiplication factor, f_{HM} is Hughmark friction factor and is defined as:

$$f_{HM} = 3.850Re^{-2/3}, \quad if\ Re_l < 1000 \quad (27)$$

$$f_{HM} = 0.5402Re^{-0.38}, \quad if\ Re_l \geq 1000 \quad (28)$$

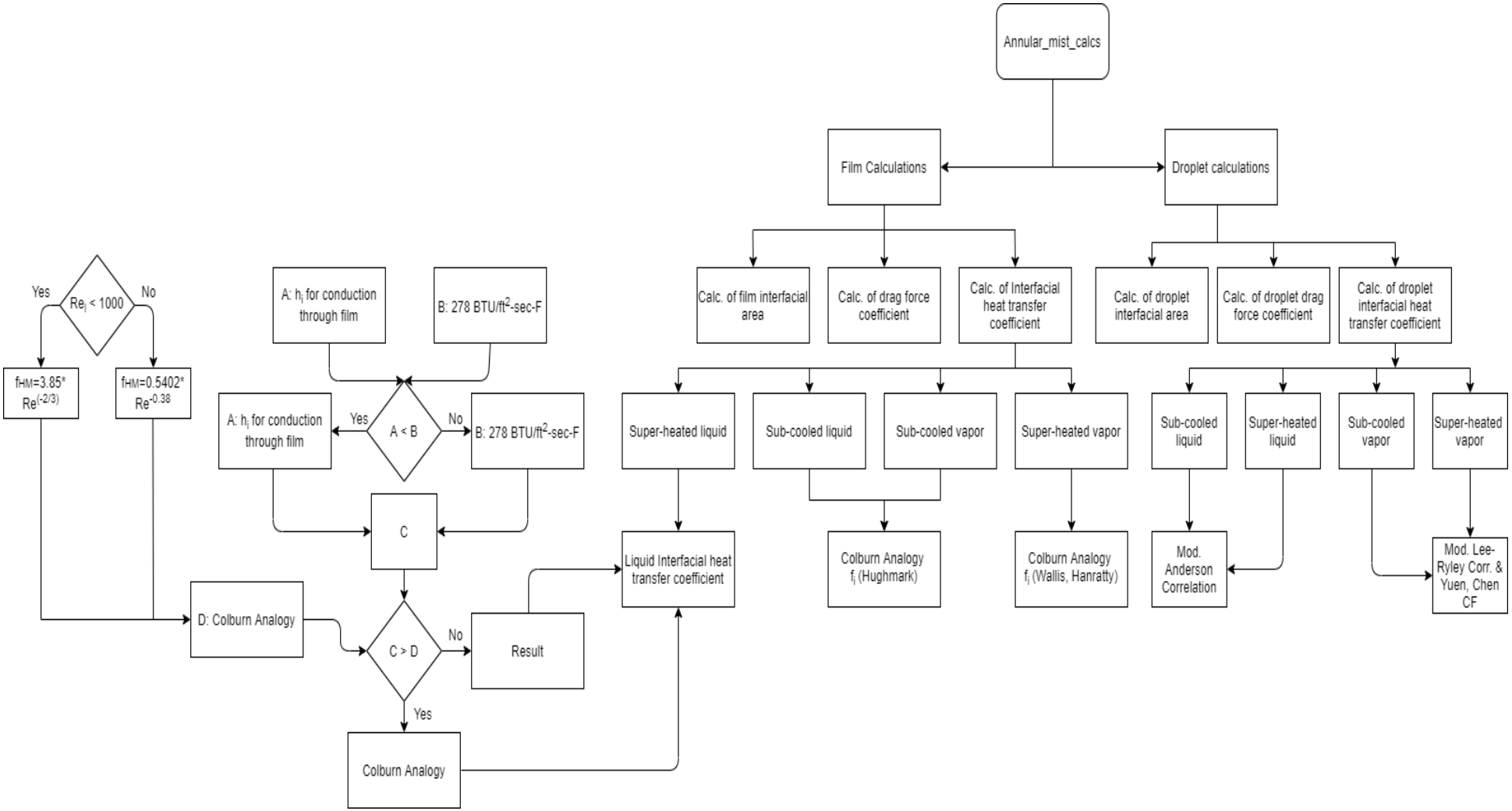

Figure 2-3 Flow chart for interfacial heat transfer calculations for film and droplets in annular flow in CTF

2.4 Interfacial friction factor correlations in literature

The following section presents a summary of the available two-phase flow interface friction studies from literature. A major drawback of these studies are that each is primarily based on the correlations on air-water experimental measurements (with the exception of one study using Refrigerants), and hence there may be some uncertainty in the application to the high-pressure steam-water diabatic flows in a nuclear fuel assembly.

2.4.1 Wallis

This thesis focuses on interfacial friction factor and interfacial shear stress in annular two-phase flow. Many of the models and options in CTF rely on methods developed by (Wallis, 1970). The primary formulation for the liquid film fraction in this flow regime is:

$$1-\alpha = 1-\frac{(D-2\delta)^2}{D^2} = \frac{4\delta}{D}\left[1-\frac{\delta}{D}\right] \tag{29}$$

Where D, and δ in Eq. 29, represents mean diameter of vapor core and liquid film thickness. The mean diameter of vapor core is given as:

$$D\sqrt{\alpha} = D-2\delta \tag{30}$$

The liquid-vapor interface is assumed to be stationary with respect to the gas core since the vapor velocity is far greater than the liquid velocity $V_g \gg V_f$.

For relatively small gas velocities, the liquid film is smooth and hence the interface friction factor can be approximated as that of smooth pipe. Whereas, for high gas velocities, waves initiate on the liquid film causing the interface to become rough. This phenomenon also leads to shearing off the waves which causes liquid droplets to be entrained in the vapor core.

Wallis obtained a linear relationship between interfacial friction factor and dimensionless film thickness. This relationship was obtained from air-water vertical and horizontal flows.

$$f_i = 0.005\left[1 + 300\frac{\delta}{D}\right] \quad (31)$$

$$f_i = 0.005[1 + 75(1 - \alpha)] \quad (32)$$

The rough pipe correlation of Nikursade and Moody for the wall shear can be approximated as follows:

$$f_i \approx 0.005\left[1 + 75\frac{k_s}{D}\right] \; 0.001 < \frac{k_s}{D} < 0.03 \quad (33)$$

2.4.2 Asali et al

(Asali, et al., 1985) discussed the effect of wave height and parameters effecting the wave height, $m_g^+ = m\left(\frac{\tau_i}{\rho_G}\right)^{-\frac{1}{2}}/\nu_G$, on interfacial friction factor for unstable (i.e., wavy) films. (Hewitt, et al., 1970) suggested that for thick liquid films the wave surface is assumed to have the same effect as a fully roughened surface. Hence, the friction factor is defined as $f_i \sim m/d_t$. While, for thin liquid films the wave surface would behave in the same manner as a smooth wall, so the friction factor is defined as $f_i = f_s$. In this treatment the height of the film is related to the mass flow rate in the film, the void fraction, and the geometry of the channel.

Subsequent studies on the friction factor showed that for high vapor velocities the tube diameter and vapor velocity have no significant effects on f_i/f_s. For high vapor velocities (U_G > 25 m/sec), with no entrainment in the vapor core the interfacial friction factor correlation suggested by Asali is:

$$\frac{f_i}{f_s} - 1 = 0.045(m_g^+ - 4) \quad (34)$$

Whereas for the vapor velocity, $U_G \cong 20\ m/sec$, Eq. 35 fits the experimentally obtained datasets better.

$$\frac{f_i}{f_s} - 1 = 0.065(m_g^+ - 4) \quad (35)$$

For the results with entrainment in the vapor core, interfacial friction factor was found to be a function of Re_G and m_g^+. To further improve the results Asali included the group $m_g^+ Re_G^{-0.2}$ in the correlation, as it includes the diameter effect on liquid film. This relationship was given as;

$$\frac{f_i}{f_s} - 1 = 0.45\left(m_g^+ - m_{gC}^+\right) Re_G^{-0.2} \tag{36}$$

A critical liquid film thickness 'm_{gC}^+' value of '4' and '5.9' was suggested for vertical upwards and downward flows respectively below which one can assume $f_i = f_s$.

To have better accuracy in interfacial friction factor calculation, different friction factor equations were derived for ripple regime and roll wave regime (i.e., the unstable liquid film regime was further divided). At low liquid flow rates ($Re_{LF} < Re_{LFC}$) in annular flows, the liquid film surface is smooth with the exception being the relatively well behaved waves superimposed on the base liquid film flow. Such a behavior is called a ripple regime. Whereas, for high liquid flow rates ($Re_{LF} > Re_{LFC}$), the liquid film is highly agitated and roll-type waves initiate. This regime is called a roll wave regime. Table 2-2 summarizes the interfacial friction factor and, film thickness formulations

Table 2-2 *(Asali, et al., 1985)* interfacial friction factor for Ripple and Roll wave regime

Regime	$\frac{f_i}{f_s} - 1$	m_g^+	C_1 **and** $\frac{\tau_i}{\tau_C}$
Ripple regime $(Re_{LF} < Re_{LFC})$	$C_1(m_g^+ - 4)$	$0.34 Re_{LF}^{0.6} \frac{\nu_L}{\nu_G}\left(\frac{\rho_L}{\rho_G}\frac{\tau_i}{\tau_C}\right)^{1/2}$	$C_1 = \begin{cases} 0.045; u_g > 25\ m/s \\ > 0.045; u_g < 25\ m/s \end{cases}$ $\frac{\tau_i}{\tau_C} \cong 1$
Roll wave regime $(Re_{LF} > Re_{LFC})$	$0.45 Re_G^{-0.2}(m_g^+ - 4)$	$0.19 Re_{LF}^{0.7} \frac{\nu_L}{\nu_G}\left(\frac{\rho_L}{\rho_G}\frac{\tau_i}{\tau_C}\right)^{1/2}$	

2.4.3 Wongwises

(Wongwises, et al., 2001) work focused on the determination of two-phase pressure drop, interfacial shear stress, and interfacial friction factor in the annular flow regime for two-phase air-water upward co-current flow. The experiment was performed in a tubular test section which was 29 mm in diameter and 3 m in length. While this involves tube diameters much larger than those in a nuclear subchannel nevertheless it is often cited in subchannel literature. In this work a new interfacial friction factor was developed for vertical upward air-water annular flow with entrainment in the core and with thick liquid films.

The interfacial shear stress in annular flow regime with entrained vapor core is presented as:

$$\tau_i = E_E U_E - E_D U_D - \frac{1}{S_c}\left[A_c \frac{dP}{dy} + U_G \frac{d\dot{m}_E}{dy} - \left(\frac{\rho_c A_c U_G^2}{P}\right)\frac{dP}{dy} + \rho_c A_c g\right] \quad (37)$$

If there is no entrainment in vapor core Eq. 37 takes the following form:

$$\tau_i = -\frac{A_c}{S_c}\left[\frac{dP}{dy} + \rho_c g\right] \quad (38)$$

The criteria for the existence of annular flow shows dependency on dimensionless superficial gas velocity (U_{SG}^*). The flow is said to be annular if $U_{SG}^* > 1$ where U_{SG}^* is defined as:

$$U_{SG}^* = U_{SG}\left[\frac{\rho_G}{(\rho_L - \rho_G)gD}\right]^{1/2} \quad (39)$$

The main findings were: a) The liquid film thickness decreases as the superficial vapor velocity is increased while keeping the liquid flow rate constant, b) the pressure drop increases with the increasing superficial gas Reynolds number, c) the shear stress increases with increasing liquid film thickness due to the increase in disturbance waves and interface roughness. These findings show that superficial gas Reynolds number and relative thickness are important parameters for the interfacial friction factor. Wongwises proposed an empirical correlation for interfacial friction factor as:

$$f_i = aRe_{SG}^{b}\left(\frac{\delta}{D}\right)^{c} \tag{40}$$

Where $a = 17.172, b = -0.768, c = -0.253$. The experimental results when compared with the empirical correlation, gives the insight that majority of data lies within $\pm 25\%$ of the proposed correlation. While their results were not divided into stable and unstable films, it is likely that most of their experimental conditions are covered regions of wavy film flow/unstable film conditions given the high superficial gas velocities in the experiment.

2.4.4 Quiben et al

(Quiben, et al., 2007) used phenomenological modeling approach to develop interfacial friction correlation for different flow regime in horizontal flow. The proposed advantage of their phenomenological model is that it may be applicable beyond the available experimental range, whereas purely empirical correlations should not be extended beyond their experimental bases. The experimental database consisted of 1745 experimental points for fluids R-22, R-134a, and R-410a with test section hydraulic diameters of 8mm and 13.8 mm. Quiben proposed the interfacial friction correlation for annular flow regime as:

$$f_i = 0.67\left[\frac{\delta}{2R}\right]^{1.2}\left[\frac{(\rho_l - \rho_g)g\delta^2}{\sigma}\right]^{-0.4}\left[\frac{\mu_g}{\mu_l}\right]^{0.08}[We_l]^{-0.034} \tag{41}$$

Where g, μ_g, μ_l, R, We_l, and σ represent gravitational acceleration, vapor dynamic viscosity, liquid dynamic viscosity, radius, liquid Weber number and surface tension. The annular flow regime was simplified by neglecting the entrainment phenomena and assuming the liquid film to have a uniform thickness around the circumference. 'δ' represent liquid film thickness was defined as:

$$\delta = \frac{\pi D(1-\epsilon)}{2(2\pi - \theta_{dry})} \tag{42}$$

Where 'D' is the hydraulic diameter and θ_{dry}= 0 for annular flows. 'ϵ' represents the void fraction and is calculated using Steiner version of Rouhani's drift flux model and is given as:

$$\epsilon = \frac{x}{\rho_g}\left[\left(1 + 0.12(1-x)\right)\left(\frac{x}{\rho_g} + \frac{1-x}{\rho_l}\right) + \frac{1.18(1-x)\left[g\sigma\left(\rho_l - \rho_g\right)\right]^{0.25}}{G\rho_l^{0.5}}\right]^{-1} \quad (43)$$

Where 'x' is the flow quality and 'G' is the mass flux.

The experimental results when compared with Quiben's correlation show that 82.3% of the data lies within $\pm$30%.

2.4.5 Schubring

(Schubring, et al., 2009) studied horizontal, air-water, two-phase annular-wavy flow conditions in 8.8 and 15.1 mm inner diameter tubes which reasonable corresponds to the range of hydraulic diameters in nuclear fuel subchannels. A wide range of superficial velocities for vapor and liquid were selected with ranges 10-86 m/s and 0.03-0.30 m/s respectively.

These results showed that for higher superficial vapor velocities (U_{sg} >30 m/s) the average film thickness is symmetrical in the horizontal assembly. Whereas at lower superficial vapor velocities, the liquid film is thicker along the bottom of the section and some corrections to the measurements taken from the mid-pipe position were needed. Furthermore, at higher flow rates the wave frequency increased with increasing liquid velocity. They observed that the two main phenomena in the annular type flows are film thickness and wave behavior. Hence, Schubring proposed a two-phase friction factor based on gas superficial kinetic energy and flow quality:

$$f_{TP} = \frac{\frac{dP}{dz}Dx}{KE_{sg}} \quad (44)$$

2.4.6 Belt et al

(Belt, et al., 2009) focused on interfacial shear stress in vertical annular flow. Their study shows the effective interface roughness is proportional to the wave height in the channel. They assumed that major contribution to interfacial friction resulted from roll-type waves hence the interface velocity can be taken as the velocity of roll waves C_W. The data used in the study was obtained from air/water flows in a pipe of 50 mm diameter at atmospheric pressure which is much larger than typical nuclear fuel subchannels. The gas and liquid superficial velocity ranges were between 22-42 m/s and 0.01-0.08 m/s respectively. They also assumed that the centerline entrained liquid droplets velocity is equal to gas bulk velocity. The proposed interfacial friction factor correlation is given below where 'δ' is local film thickness:

$$C_{f,i} = 1.158\frac{\delta}{D} + 3.413 * 10^{-4} \tag{45}$$

2.4.7 De Paula Junior

(de Paula Junior, et al., 2017) compared interfacial friction factor correlations against experimental data. Their results extend the work of (Pedras, 1993) who observed that the drag force for the liquid droplets is directly proportional to the liquid-vapor interfacial friction factor, and hence correlation of the interfacial friction can be done using observed droplet velocities. The 2017 results concluded that (Pedras, 1993) correlation demonstrates better agreement with the experimental data however this may result from the fact that their validation used data from the same facility. However, the good agreement may also stem from the inclusion of the gas drift velocity and liquid phase properties in the correlation.

The interfacial friction factor proposed by Pedras is as follows:

$$f_i = -0.0078 + 52\left(1 - \sqrt{\emptyset_G}\right)N_\rho Re_{V,G}^{2/5} \tag{46}$$

2.4.8 Aliyu et al

(Aliyu, et al., 2017) performed vertical annular two-phase upward flow experiments in large diameter pipes with internal diameter of 101.6 mm and with gas and liquid superficial velocities ranges between 11-29 m/s and 0.1-1.0 m/s respectively. While this study includes additional experimental data, the tube diameter is so much larger than the characteristic dimensions of a fuel assembly it is difficult to assess the applicability. A total 332 data were collected for this experiment and were combined with data obtained from 12 other sources with pipe ID ranging 5 – 127 mm. Hence some of the data used in their modeling does cover the range of dimensions relevant to a nuclear fuel bundle, however, the authors do not provide a breakdown of the models performance for the low end of the sizes used. The results showed that the liquid film thickness increases with increasing superficial liquid velocities and is inversely proportional to the superficial gas velocities, similar to many previous studies. Furthermore, interfacial friction increased with an increasing gas-liquid interfacial slip and/or superficial gas velocity, also similar to the other literature discussed previously.

They retained t/D in the interfacial friction correlation hence preserving Wallis correlation form which works well for thin and smooth film conditions. The inclusion of Reynold's number accounts for inertial effects/changes in the gas core while the Froude number captures the effect of the gravitational force. Non-linear least squares regression with the entire experimental database yields the following interfacial friction factor correlation:

$$f_i = f_s \left[1 + 0.3 \left(\frac{t}{D}\right)^{0.12} Re_g^{0.54} Fr_g^{-1.2}\right]^{1.5} \tag{47}$$

Where $f_s = 0.046 Re_g^{-0.2}$. Eq. 44 can also be used for cases when dimensionless diameter (D^*) is greater than 2.

$$D^* = \frac{D}{\sqrt{\frac{\sigma}{g(\rho_l - \rho_g)}}};\ D^* < 2\ corresponds\ to\ D < 5mm \tag{48}$$

2.4.9 Sun et al

The (Sun, et al., 2018) study covered six different experimental data base with diameters ranging between 19 – 50.8 mm, superficial gas Reynolds number Re_{sg} from 7770 to 186,000, and the superficial liquid Reynolds number Re_{sl} from 80 to 12,350. They used the Berna correlation for average film thickness and Kataoka correlation for entrainment rate calculations. Ten interfacial friction factor correlations were used for comparison purposes, however the value of this comparison is limited since interfacial roughness was assumed based on the data, and not directly calculated using a model. Given that there are significant deviations in each correlation's methodology for determining the liquid wave height, the true scatter of the correlations was likely under-estimated.

They suggested that the interfacial roughness (k_s) increases with increasing Re_{sl} for constant Re_{sg} whereas there can be seen a notable increase in k_s due to wave formation at low Re_{sg} and high Re_{sl}. After the onset of disturbance waves, the entrained droplets affect the turbulence in the gas core dependent on droplet interfacial area. Overall, for configurations that increase the gas core turbulence there is an increase in interfacial shear stress. The proposed correlation for interface roughness before disturbance wave occurrence is:

$$\frac{k_s}{d} = 1.4637 * 10^7 Re_{sg}^{-0.0332} Re_{sl}^{-1.2011} \left(\frac{u_{sl}}{u_{sg}}\right)^{1.8353} \left(\frac{\rho_l}{\rho_g}\right)^{0.1252} \tag{49}$$

After the onset of disturbance wave, the roughness can be determined from:

$$\frac{k_s}{d} = 1.4637 * 10^7 Re_{sg}^{-0.0332} Re_{sl}^{-1.2011} \left(\frac{u_{sl}}{u_{sg}}\right)^{1.8353} \left(\frac{\rho_l}{\rho_g}\right)^{0.1252} \tag{50}$$

The interfacial friction correlation is adopted from Haaland correlation and is calculated by substituting interfacial roughness for undisturbed and disturbed regimes.

$$\frac{1}{\sqrt{f_i}} = -3.6log\left[\frac{6.9}{Re_{gc}} + \left(\frac{k_s}{3.7D}\right)^{1.11}\right] \quad (51)$$

While comparing the results with other ten correlations the mean absolute percentage error (MAPE) was than 23%.

2.4.10 Ju et al

(Ju, et al., 2019) proposed replacing film thickness in the interfacial friction correlations by a dimensionless number in order to increase the application potential of the correlations. In their work annular flow was sub-divided into two regimes; with entrainment and without entrainment. In these annular flows, the vapor core may or may not contain droplets. Similarly the liquid film may or may not have waves. These waves can be categorized either as ripple waves or disturbance waves (which were defined similar to the more chaotic "roll-waves" in other literature). The proposed dimensionless film thickness correlation is:

$$\frac{\delta}{D} = 0.071tanh\left(14.22We_f^{0.24}We_g''^{-0.47}N_{\mu_f}^{0.21}\right) \quad (52)$$

Where $We_f, We_g, and\ N_{\mu_f}$ represents liquid weber number, gas weber number, and viscosity number respectively. In order to incorporate the effect of entrained droplets in the vapor core the gas weber number was modified to include the density ratio between the droplets and vapor. They hypothesized that the interfacial friction factor decreases as We_g'' increases for constant We_f. This is due to that fact that for constant We_f, as We_g'' increases the film thickness decreases which reduces the interface roughness. The friction factor increases as We_f increases for same We_g'', as We_f increases the film thickness increases which tends to increase the interface roughness hence

increasing the interfacial friction factor. Based on four collected data bases the interfacial friction factor proposed by Ju for disturbance wave regime is:

$$f_i = 0.0028 + 4.28We_f^{0.28}We_g''^{-0.53}N_{\mu_f}^{0.25} \quad (53)$$

The gas weber number tends to decrease the interfacial friction factor whereas liquid weber number and viscosity number tend to increase the friction factor. The mean absolute error was found to be 15% for all of the data considered.

2.5 Interfacial friction factor summary

Table 2-3 summarizes the literature available on interfacial friction factor formulations. A significant limitations in these correlations is that most focus is on air-water mixtures and diameters much larger than the characteristic dimension of a subchannel. The experimental database for interfacial friction factor includes the measurement of liquid film flow rates, liquid film thickness, interfacial shear stress and pressure gradient. The interfacial friction factors are then determined by substituting interfacial shear stress in the correlations. With all these experimentally measured parameters there are certain phenomena which are assumed hence increasing further uncertainty in interfacial friction factor prediction. Some main assumptions which are common in some studies are: a) No entrainment in the gas core b) Rate of entrainment is equal to rate of deposition c) Entrainment droplet velocity to be twice as of mean liquid film velocity while droplet deposition velocity is 80% of the mean gas velocity. The accurate prediction of these aforementioned parameters is of great significance as it plays a vital role in momentum transfer to and from liquid film to gas core.

Table 2-3 Summary of literature reviewed interfacial friction factor correlation along with the working fluids and their applicability range/experimental conditions

Correlation	Interfacial friction correlation	Fluids	Applicability range
(Wallis, 1970)	$f_i = 0.005\left[1 + 300\frac{\delta}{D}\right]$ $f_i = 0.005[1 + 75(1-\alpha)]$ $f_i \approx 0.005\left[1 + 75\frac{k_s}{D}\right]\ 0.001 < \frac{k_s}{D} < 0.03$	Air-Water	Diameter: 50.8mm and 76.2 mm
(Asali, et al., 1985)	$\frac{f_i}{f_s} - 1 = C_1(m_g^+ - 4);\ m_g^+ = 0.34Re_{LF}^{0.6}\frac{\nu_L}{\nu_G}\left(\frac{\rho_L}{\rho_G}\frac{\tau_i}{\tau_C}\right)^{1/2}$ Ripple Regime $\frac{f_i}{f_s} - 1 = 0.45Re_G^{-0.2}(m_g^+ - 4);\ m_g^+ = 0.19Re_{LF}^{0.7}\frac{\nu_L}{\nu_G}\left(\frac{\rho_L}{\rho_G}\frac{\tau_i}{\tau_C}\right)^{1/2}$ Roll wave Regime Ripple Regime: $Re_{LF} < Re_{LFC}$ Roll Wave Regime:$Re_{LF} > Re_{LFC}$	Air-Water, Air-water-glycerine	Diameter: 22.9 and 42 mm Viscosity: 1.1-5.0 mPa.s
(Pedras, 1993)	$f_i = -0.0078 + 52\left(1 - \sqrt{\emptyset_G}\right)N_\rho Re_{V,G}^{2/5}$	Air-Water	Diameter: 27.1 mm Pressure: 96.167-98.014 kPa J_L: 0.02333-0.07065 m/s J_G: 13.24-35.51 m/s
(Wongwises, et al., 2001)	$f_i = 17.172Re_{sg}^{-0.768}\left(\frac{t}{D}\right)^{-0.253}$	Air-water	Diameter: 29 mm Pressure: 100 kPa
(Quiben, et al., 2007)	$f_i = 0.67\left[\frac{\delta}{2R}\right]^{1.2}\left[\frac{(\rho_l - \rho_g)g\delta^2}{\sigma}\right]^{-0.4}\left[\frac{\mu_g}{\mu_l}\right]^{0.08}[We_l]^{-0.034}$	R22, R-134a, R-410a	Diameter: 8mm and 13.8mm
(Schubring, et al., 2009)	$f_{TP} = \frac{\frac{dP}{dz}Dx}{KE_{sg}}$	Air-Water	Diameter: 8.8 mm, 15.1 mm; $V_{sg}\ (10 - 86\ m/s)$ $V_{sf}(0.03 - 0.30\ m/s)$
(Belt, et al., 2009)	$C_{f,i} = 1.158\frac{\delta}{D} + 3.413 * 10^{-4}$	Air-Water	Diameter: 50 mm Pressure: 101.325 kPa $V_{sg}\ (22 - 42\ m/s)$ $V_{sf}(0.01 - 0.08\ m/s)$
(Aliyu, et al., 2017)	$f_i = f_s\left[1 + 0.3\left(\frac{t}{D}\right)^{0.12}Re_g^{0.54}Fr_g^{-1.2}\right]^{1.5}$	Air-water	Diameter: 16-127 mm Pressure: up to 600 kPa Also applicable for Diameter > 5mm
(Sun, et al., 2018)	$\frac{1}{\sqrt{f_i}} = -3.6log\left[\frac{6.9}{Re_{gc}} + \left(\frac{k_s}{3.7D}\right)^{1.11}\right]$	Air-water	Diameter: 19-50.8 mm Re_{sg}: 7,770 − 186,000

	$Undisturbed\ Wave: \frac{k_s}{d} = 1.4637 * 10^7 Re_{sg}^{-0.0332} Re_{sl}^{-1.2011} \left(\frac{u_{sl}}{u_{sg}}\right)^{1.8353} \left(\frac{\rho_l}{\rho_g}\right)^{0.1252}$ $Disturbed\ wave: \frac{k_s}{d} = 6.5048 * 10^{10} Re_{gc}^{-2.4414} Re_{lf}^{0.1967} \left(\frac{u_{sl}}{u_{sg}}\right)^{0.2122} \left(\frac{\rho_l}{\rho_g}\right)^{-0.0208}$		$Re_{sl}: 80 - 12{,}350$
(Ju, et al., 2019)	$f_i = 0.0028 + 4.28 We_f^{0.28} We_g''^{-0.53} N_{\mu_f}^{0.25}$ (Correlation only for disturbance wave)	Air-water	Diameter: 9.4 – 50.8 mm $0.0264 \leq We_f \leq 37.9$ $146 \leq We_g'' \leq 29100$ $0.00019 \leq N_{\mu_f} \leq 0.0232$

2.6 Lane model

(Lane, 2009) in his Ph.D. dissertation focused on the comprehensive annular flow modeling in CTF. The interfacial friction faction used in CTF-Lane model is derived from the work by (Hurlburt, et al., July 2006). This method partitions the annular film into two sub layers, a wave layer and an underlying film zone. Overall, the interfacial friction factor in Lane's work depends on test section/subchannel geometry and the flow conditions. As a result the friction factor correlations are different for circular and planar geometries. In order to attain numerical stability in CTF lower and upper limits were set for the key interfacial parameters to limit non-physical predictions during the iterative routine until a converged solution is reached. Unfortunately the code does not display active warning when these limits are being reached. The lower limit is 0.005 which corresponds to smooth fully turbulent flow and the upper limit is five times that of the value obtained by (Whalley, et al., 1978) correlation. The interfacial friction factor for circular geometry being used is:

$$f_{i,k,tube}\left(c_{B,k},\widehat{\varepsilon_k}\right)=\left[\frac{0.58}{-\frac{ln\widehat{\varepsilon_k}}{(\widehat{\varepsilon_k}-1)^2}-lnc_{B,k}+1.05+\frac{1}{2}\frac{(\widehat{\varepsilon_k}+1)}{(\widehat{\varepsilon_k}-1)}}\right]^2 \tag{54}$$

Where the non-dimensional roughness is defined as $\widehat{\varepsilon_k}=\frac{\varepsilon_k}{R-\delta_{min}}$. The interfacial friction factor for planar geometries is determined as:

$$f_{i,k,duct}\left(c_{B,k},\widehat{\varepsilon_k}\right)=\left[\frac{0.58}{\frac{ln\widehat{\varepsilon_k}}{\widehat{\varepsilon_k}-1}-lnc_{B,k}+1.05}\right]^2 \tag{55}$$

The film thickness in CTF-Lane version is determined as:

$$\bar{\delta}=\frac{1}{2}\left(D_H-D_{gc}\right) \tag{56}$$

Rearranging Eq. 56:

$$\frac{\bar{\delta}}{D_H}=\frac{1}{2}\left(1-\frac{D_{gc}}{D_H}\right) \tag{57}$$

Where gas core void friction is defined as:

$$\alpha_{gc}=1-\alpha_l=\frac{A_{gc}}{A_x}=\frac{D_{gc}^2}{D_H^2} \tag{58}$$

Substituting the ratios of diameter from Eq. 58 in Eq. 57 leads to Eq. 59 which is the dimensionless film thickness expression used in Lane's model.

$$\frac{\bar{\delta}}{D_H}=\frac{1}{2}\left[1-\sqrt{(1-\alpha_l)}\right] \tag{59}$$

Figure 2-4 and Figure 2-5 shows the predicted pressure drop results vs. experimental measurements from the RISO facility for adiabatic and diabatic cases respectively. While there is some improvement in annular film pressure drops using the Lane model as compared to the other CTF models, our testing shows significant discrepancies for diabatic tests. This likely resulted from the limits of the derivation of the model where only adiabatic test cases with outlet flow quality greater than 20% were considered for Lane model development.

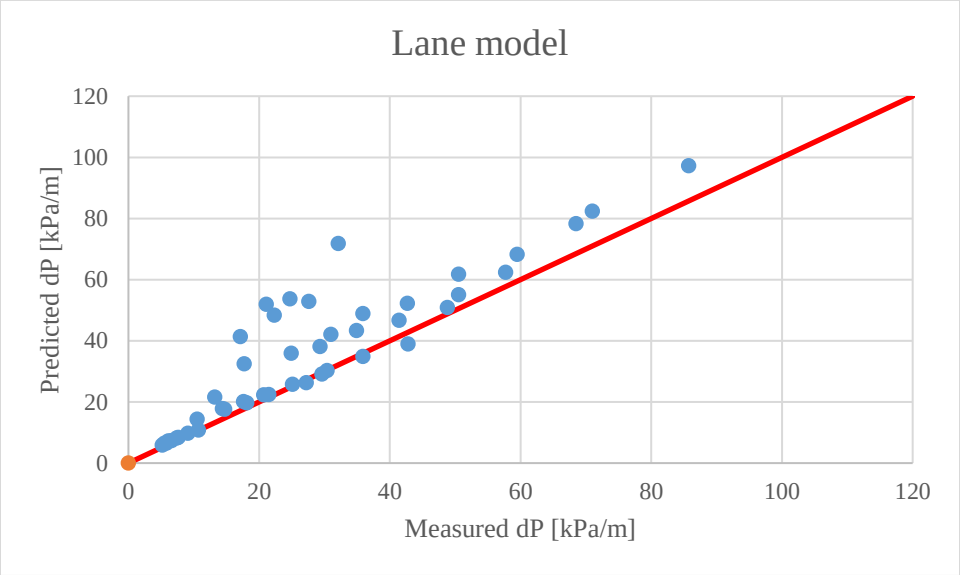

Figure 2-4 Predicted vs. measured pressure drop for RISO experiment using Lane model [Adiabatic]

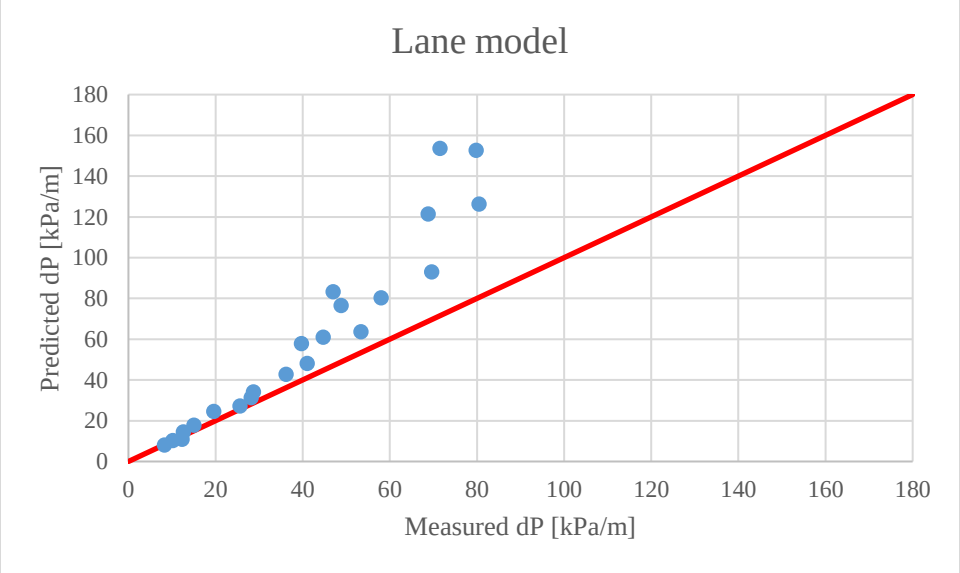

Figure 2-5 Predicted vs. measured pressure drop for RISO experiment using Lane model [Diabatic]

2.7 Bundle Enthalpy Imbalance Number

In a fuel channel there are different arrangement of subchannels with subchannels having different flow areas and heat inputs. Subchannel mixing phenomena act to transport fluid from one subchannel to another depending on the local conditions and geometries. Depending on the conditions and geometries this can lead to difference between the local subchannel quality, void fractions and velocities. It is well observed from the experimental results that CHF dependent on local conditions and hence prediction of the individual subchannel conditions is paramount (McPherson, 1971).

The bundle enthalpy imbalance number (BEIN) is defined as the relative difference between the maximum and mean enthalpy rise rate to that of mean enthalpy changes (McPherson, 1971). It is represented mathematically as:

$$BEIN = \frac{(dH/dL)_{max} - (dH/dL)_{mean}}{(dH/dL)_{mean}} \tag{60}$$

For the tests in this thesis that examine 28-element fuel channel flows the BEIN is used to characterize the changes in bundle lateral imbalance observed for different correlation options. While the intent of this thesis was not to examine the lateral mixing phenomena (void drift, turbulent mixing) which may dominate subchannel imbalance, it was important to demonstrate how the changes in interfacial modeling also affect gross parameters such as BEIN.

3 Methods

3.1 Pressure drop calculation using CTF

Accurate prediction of the pressure drop is an important aspect of thermalhydraulics used in safety assessments. There are various computational tools used for pressure drop predictions in the nuclear industry ranging from one-dimensional two-fluid system codes like RELAP, one-dimension homogenous codes like RAMONA, to subchannel codes like CTF. Such tools use empirically derived correlations from experiments either directly to get the two-phase pressure drop, or within their models used to predict interphase phenomena. In terms of thermalhydraulics codes, they are often classified either as system level codes or subchannel codes. The system codes like REPLAP5, CATHENA, and TRACE are focused on modeling thermalhydraulic phenomenon over the entire primary and/or secondary head transport system under a wide range of operating and design-based conditions.

The subchannel codes such as CTF and ASSERT are focused on modeling thermalhydraulic phenomenon in nuclear reactor subchannels. These simulations provide a detailed knowledge about subchannels parameters like pressure drop, CHF margins, void fraction, quality etc. locally within a bundle, which support for the design and safety analysis of nuclear reactors. A major activity in qualifying these codes is the comparison to experimental results obtained from various sources. This thesis does the CTF predictions comparison to several available experiments in literature with a particular focus on conditions relevant to CANDU reactors.

3.1.1 RISO experiment

In the current study the pressure drop calculations are focused on the annular flow regime in CTF, primarily because such conditions can occur in CANDU reactors during accident analysis. (Wurtz,

1978) performed experiments studying the pressure gradients, film thickness, film flow rates, wave frequencies and velocities in vertical tubular and annular geometries under conditions which give rise to annular liquid films. A total of 250 experiments were performed by Wurtz for adiabatic and diabatic conditions at different pressures, mass fluxes and heat fluxes.

For this experiment the vertical tubular test section modeled in CTF is 0.01 m in diameter and 9.0 m in length. A total of 70 test cases in adiabatic conditions and 22 diabatic conditions are selected for CTF simulations. For the adiabatic experiments the pressure, inlet sub-cooling, and mass flux ranges are 30 – 90 [bar], 8 – 60 [%], and 500 – 3000 [kg/m^2-sec] respectively. Whereas, all the 22 diabatic conditions cases are performed at 70 bar pressure with inlet sub-cooling, mass flux, and heat flux ranges at 16 – 80 [%], 500 – 3000 [kg/m^2-sec], and 50 – 150 [kW/cm^2] respectively. A study of the test conditions and comparison to several vertical flow regime maps in the following paragraphs indicated that all of the considered cases have predominantly the annular flow regime. The flow regime expressions for two different flow regime maps in vertical flow regime; Fair (1960) and Hewitt and Roberts (1969) are obtained from (Thome , et al., 2015) and used to ensure that the regime in the experiment are annular.

Expressions from the Fair (1960) flow regime map are implemented in computer simulation (MATLAB). In order to utilize the map, firstly the values of x-axis 'X_F' and total mass flux 'Y_F' are calculated. Eq. 61 and Eq. 62 represent x-axis 'X_F' and y-axis 'Y_F' respectively.

$$X_F = \left(\frac{x}{1-x}\right)^{0.9} \left(\frac{\rho_l}{\rho_g}\right)^{0.5} \left(\frac{\mu_g}{\mu_l}\right)^{0.5} \tag{61}$$

$$Y_F = G\ [\frac{kg}{\mathrm{s}^2 - m}] \tag{62}$$

The calculated values are used to determine if the flow is bubbly, slug, annular or mist. Eq. 63 – Eq. 65 present the transition thresholds between these flow regimes.

The expression for bubbly to slug flow is:

$$Y_F = 80.6{X_F}^{-1.492} \; for\ the\ range\ 0.2 \leq X_F \leq 3 \; and \; 15.6 \leq Y_F \leq 879 \quad (63)$$

The expression for slug flow to annular flow is:

$$Y_F = 503{X_F}^{-1.231} \; for\ the\ range\ 0.5 \leq X_F \leq 18 \; and \; 14.6 \leq Y_F \leq 1221 \quad (64)$$

The expression for annular to mist flow is:

$$Y_F = 2988{X_F}^{-1.044} \; for\ the\ range\ 3 \leq X_F \leq 90 \; and \; 28.3 \leq Y_F \leq 976 \quad (65)$$

Hewitt and Roberts (1969) map uses the ratio of the square of phasic mass flux to phasic density of vapor and liquid phase for y-axis and x-axis respectively. The x-axis 'X_H' and y-axis 'Y_H' for Hewitt and Roberts (1969) map are defined by Eq. 66 and Eq. 67 respectively.

$$X_H = \frac{G_l^2}{\rho_l} \; [\frac{kg}{s^2 - m}] \quad (66)$$

$$Y_H = \frac{G_v^2}{\rho_v} \; [\frac{kg}{s^2 - m}] \quad (67)$$

Similar to the Fair (1960) map, the transition threshold expressions are obtained from Thom's study for Hewitt & Roberts map (Eq. 68 – Eq. 76). In Hewitt flow regime map there is no distinct transition line between slug flow and bubbly-slug flow hence these flows are grouped together. Furthermore, in some literature regarding flow regime map the annular flow regime is not divided into annular and wispy-annular, whereas Hewitt's map contains this division. Hence, Hewitt's map annular and wispy-annular flow are both considered as annular flow.

The transition expressions for slug to churn flow are:

$$Y_H = 0.021X^{1.278}; where\ 10 \leq X_H \leq 90 \; and \; 0.4 \leq Y_H \leq 6.8 \quad (68)$$

$$Y_H = 0.092{X_H}^{0.963}; where\ 90 \leq X_H \leq 500 \; and \; 6.8 \leq Y_H \leq 35 \quad (69)$$

$$Y_H = 2.18{X_H}^{0.4489}; where\ 500 \leq X_H \leq 1000 \; and \; 35 \leq Y_H \leq 48 \quad (70)$$

$$Y_H = 33.4{X_H}^{0.051}; where\ 1000 \leq X_H \leq 6000 \; and \; 48 \leq Y_H \leq 52.5 \quad (71)$$

The transition expressions for churn to annular flow are:

$$Y_H = 219{X_H}^{-0.399}; where\ 1.3 \leq X_H \leq 10 \; and \; 90 \leq Y_H \leq 200 \quad (72)$$

$$Y_H = 90; where\ 10 \leq X_H \leq 50000 \quad (73)$$

The transition expressions for annular flow to wispy annular flow are:

$$X_H = 1000; where\ 90 \leq Y_H \leq 900 \quad (74)$$

$$Y_H = 2 * 10^{-9} {X_H}^{3.894}; where\ 1000 \leq X_H \leq 1300\ and\ 900 \leq Y_H \leq 2500 \quad (75)$$

$$Y_H = 0.439 {X_H}^{1.217}; where\ 1300 \leq X_H \leq 3000\ and\ 2500 \leq Y_H \leq 7000 \quad (76)$$

For all the CTF runs of the RISO experiment, Thome correlation and CTF specific correlation are selected for nucleate boiling and rod friction factor calculations, respectively. In order to select these correlations; option '2' is selected for rod friction factor in Card Group 1.1 and option '1' is selected for nucleated boiling correlation in Card Group 8.1 in CTF input file. All the cases run are for pseudo-transient conditions for a sufficient length of time such that steady state is achieved.

For the diabatic experiments there was an unheated entrance length followed by the heated portion of the test section. The diabatic length defined by Wurtz is the distance between the inner sides of power clams. The diabatic length used for these cases is 4.02m. Therefore, in the CTF simulations of diabatic cases, the heated length starts at 4.88 m from the inlet and ends at 8.9 m. The results presented in Chapter 4 show that the pressure drop predicted by CTF is significantly overpredicted.

This overprediction in the pressure drop for annular flow conditions can either be due to wall drag models or interfacial shear stress models. In the wall drag models, frictional pressure drop play an important role whereas for interfacial shear stress, interfacial friction factor has a decisive role. In current CTF version the Wallis interfacial friction correlation is used for the stable film and Henstock and Hanratty model is used for unstable film conditions.

Given that the wall friction models are consistent with many other codes, and that single-phase predictions shows acceptable accuracy, there is interest in explicitly assessing the interfacial friction components. After an extensive literature review several interfacial friction factor correlations are selected for consideration. The selection criteria is mostly dependent on their applicability range and their prediction results when used for different databases. These

correlations are implemented in the CTF source code and the results are compared with the experimental datasets in subsequent chapters. The selected interfacial friction correlations are as follows;

1. Wongwises correlation (Wongwises, et al., 2001)
2. Quiben correlation (Quiben, et al., 2007)
3. Belt correlation (Belt, et al., 2009)
4. Aliyu correlation (Aliyu, et al., 2017)
5. Sun correlation (Sun, et al., 2018)
6. Ju correlation (Ju, et al., 2019)

3.2 CANDU 28-element rod bundle

An additional source of benchmarking data for the studies is from full scale test conducted at Stern Labs located in Hamilton, Ontario. The horizontal 28-element CANDU fuel channel experiment contains all of the relevant geometry an electrically heated fuel element simulators and can operate at CANDU conditions. The fuel channel is divided into 12 bundles with each bundle length of approximately 0.5 m. In order to achieve the geometric similarity, heater elements are divided into 12 bundles, each having length of 495.3 mm (Novog, 2019). The heated length of heater element for each bundle is ~ 480.12 mm with the remaining ~ 15.18 mm of unheated length. The outer diameter of the fuel element simulator is 15.34 mm. The axial heat flux distribution is cosine shaped. The radial power profile is such that the outer pins provides the relative power where the specified power for the pins are; 1.104, 0.902, and 0.780 for outer, middle and inner circle pins respectively. Figure 3-1 shows the bundle length and the pressure tap locations. While, Figure 3-2 presents the cross sectional view of the fuel channel with 28 fuel elements and 41 subchannels.

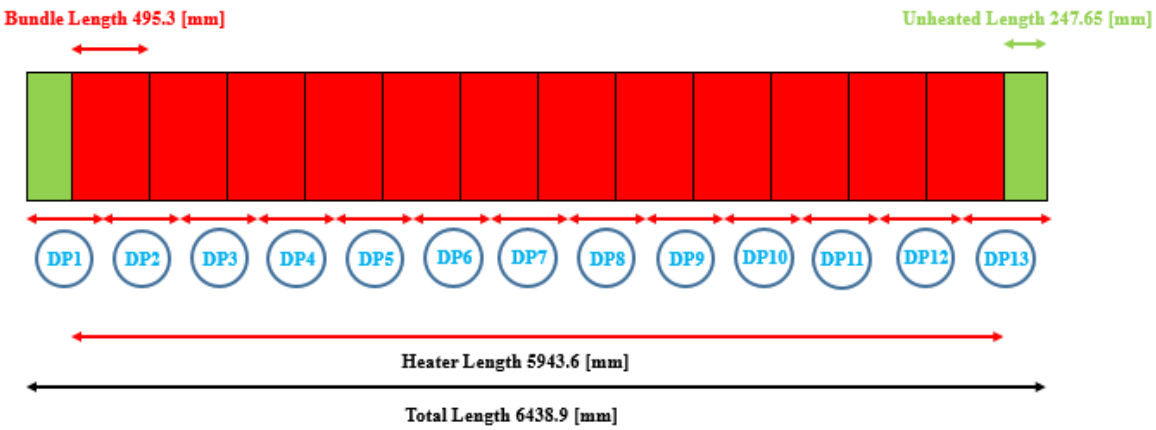

Figure 3-1 Represents bundle length, heated length and total length of fuel channel and pressure taps locations

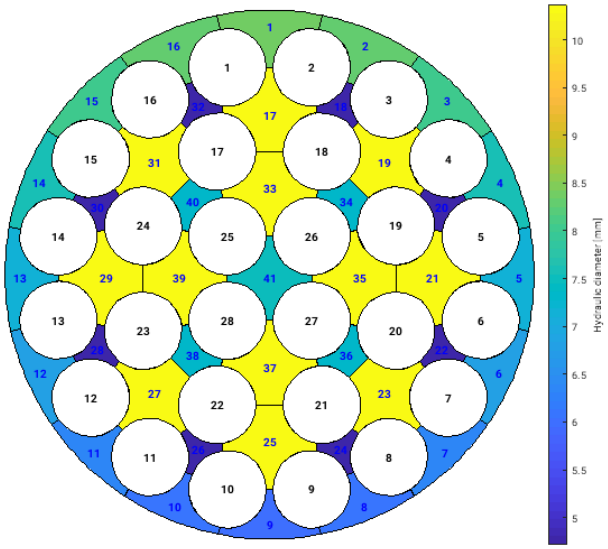

Figure 3-2 1.35 mm Test Assembly Subchannel and Fuel Element Numbering Schemes (as viewed looking downstream) for an Uncrept Pressure Tube *(Novog, 2019)*

The subchannel geometry for 28-element rod bundle is left to right symmetric i.e. subchannel 2 – 8 would have same flow area, wetted perimeter, heated perimeter as that of subchannel 16 – 10 respectively. The purple triangular subchannels have the smallest flow area whereas yellow color

represents subchannels with largest flow areas. There is an offset in fuel assembly center and PT center for nominal conditions due to the fact that the bundle dimensions are slightly smaller than the pressure tube, and, thus the bundle rests on the bottom of the PT, with the bundle centerline being slightly offset downward from PT centerline. This causes the flow area of the outer top subchannels to be larger than the bottom subchannels. Bearing pads are used on outer ring fuel pins to limit PT and fuel assembly contact. Test were conducted at Stern Laboratories under different bearing pads height to analyze the effect of eccentricity on fuel thermalhydraulics.

The horizontal 28-element rod bundle is modeled in CTF for pressure drop measurements, flow rates calculations, and enthalpy imbalance factors. The test cases were run using two different bearing pads heights 1.17 mm and 1.35 mm. Furthermore, given that the CANDU pressure tube age during their lifetime and increases slightly in diameter, cases are also considered for the crept and the uncrept pressure tube. The CTF model for horizontal 28-element includes bearing pads, spacers, and end plates. User can either geometrically model or use loss coefficients (K-factors) for bundle appendages. Due to the complication of geometric modeling in CTF for end-plats, spacers, and bearing pads, loss coefficients (K-factors) are used in the CTF model. Hameed's uniform K-factors are obtained from (Waddington, et al., 1995) and implemented in CTF.

- 0.440 for bundle junction/endplates,
- 0.112 for a spacer plane,
- 0.012 for bearing pads

Thom's correlation is selected for nucleate boiling model in CTF which will be used both in subcooled and saturated boiling regions. For rod friction factor calculation, Hameed's correlation is used. (Waddington, et al., 1995) concluded that Hameed's uniform K-factors and rod friction

factor model showed the best results. Hameed's rod friction model is of the Blasius form which is as:

$$f = aRe^{b} \tag{77}$$

Where the coefficients 'a' and 'b' are 0.101 and -0.148 respectively.

Table 3-1 Single and two-phase pressure drop experimental conditions *(Novog, 2019)*

Case	Tin [C]	Outlet Pressure [kPa]	Flow [kg/sec]	Test section power [kW]	Bearing pad height [mm]	Channel diameter
1.11 COG17-359	252	9000	22	3000	1.35	Uncrept
1.12 COG16-370	252	9000	22	8000	1.35	Uncrept

Table 3-2 Test cases for enthalpy imbalance factor calculations *(Novog, 2019)*

Case	Tin [C]	Outlet Pressure [kPa]	Flow [kg/sec]	Test section power [kW]	Bearing pad height [mm]	Channel diameter
2.12 COG17-400	252.0	10000	22.0	9505	1.35	Uncrept
2.13 COG17-603	252.1	10000	22.0	4002	1.35	Crept
2.14 COG17-612	252.1	10000	22.0	8000	1.35	Crept

The current CTF version allows user to have variation in flow area, gap width, and wetted perimeter along the axial subchannel length (This is done in CARD GROUP 5 & 6 in CTF input

file). This gives the opportunity to analyze CTF prediction for crept PT cases. The crept PT diameter values at different axial locations are taken from OECD-NEA blind benchmark on CANDU thermalhydraulics (Novog, 2019). According to the report, the flow diameter for crept channel increased axially from the nominal dimensions at the inlet and reached a maximum of 0.1073 mm at axial location of 4.086 m. It then started decreasing and reached the nominal diameter at end location.

In CTF input file, for the modeling of PT creeping effect; the increase in subchannel flow area, gap width, and wetted perimeter are used. These updated parameter values are obtained by using AUTOCAD software and the dimensions provided in the OECD-NEA 28-element benchmark specifications.

3.3 Turbulent mixing effect on BEIN

The subchannels in nuclear reactor core are interlinked with neighboring subchannels by means of gaps. This mixing with neighboring subchannels have influence on local subchannel parameters such as pressure, enthalpy, quality etc. (Carlucci, et al., 2003) worked on the relationship development for single and two-phase inter-subchannel turbulent mixing. In order to optimize these relationships, they were implemented in subchannel codes and assessed. The optimized relationships gave an excellent prediction with enthalpy migration data for vertical flows. In CTF input deck user can select either of the four options for mixing and void drift model which are as follows:

- 0 –Neither mixing nor void drift
- 1 –User-specified constant two-phase turbulent mixing coefficient
- 2 –Single-phase mixing coefficient according to Rogers and Rosehart

- 3 –User-specified constant single-phase turbulent mixing coefficient; two-phase multiplier according to Beus (Beus, 1971)

For the current study CTF option '3' is selected for mixing and void drift model. This card group '12.3' has three input terms; AAAK, BETA, and THETM representing equilibrium distribution parameter weighting factor in void drift model, constant single-phase turbulent mixing coefficient, and ratio between the maximum two-phase turbulent mixing coefficient and the single-phase mixing coefficient respectively. For the terms AAAK and THETM the suggested values of 1.4 and 5.0 respectively from CTF user manual are used. The BETA value is increased from 0.007 – 0.084 with 0.007 increment. The analysis is then performed for 28-element rod bundle for 1.17 mm and 1.35 mm bearing pads cases. Tests were also performed to examine the sensitivity to these parameters.

4 Results and discussion

4.1 CTF prediction of the RISO experiment pressure drop

Figure 4-1 and Figure 4-2 are the vertical flow regime maps for Fair and Hewitt and Roberts along with the data points at the exit of each RISO test. These plots depict that the selected adiabatic cases for RISO experiment lie in the annular flow regime and/or mist/wispy annular regime.

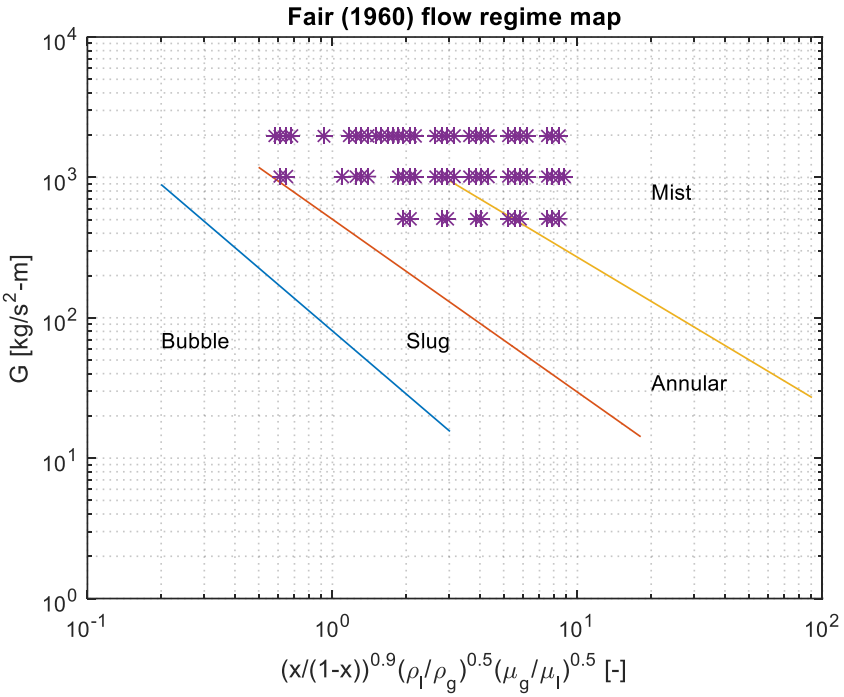

Figure 4-1 Selected RISO adiabatic cases data against Fair (1960) flow regime map

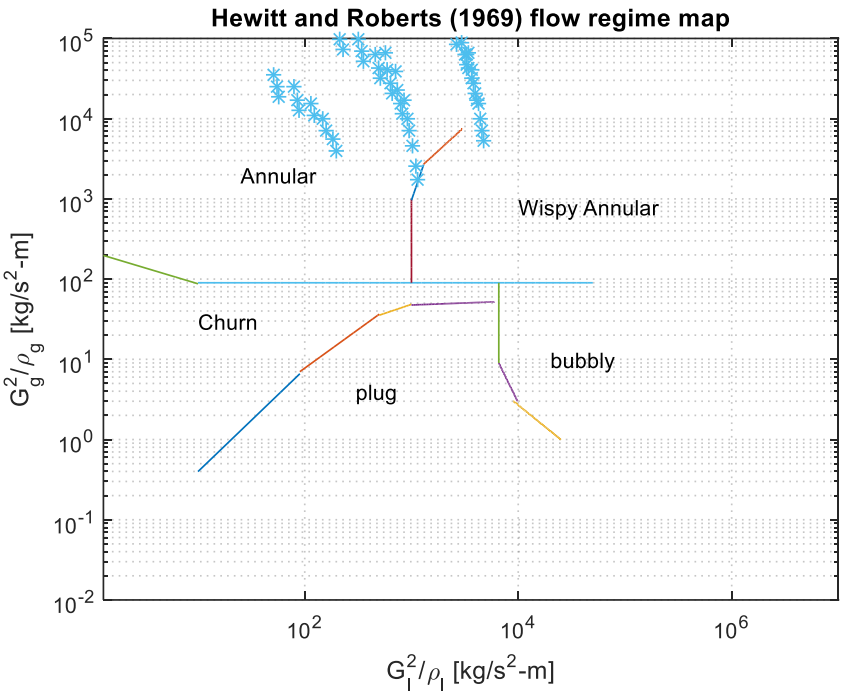

Figure 4-2 Selected RISO cases against Hewitt and Roberts (1969) flow regime map

For assessing the pressure drop, a total of 70 adiabatic test cases are modeled in CTF. The pressure range for the test cases is 30 – 90 bar with different combination of thermalhydraulic parameters such as heat flux and mass flow rate. The pressure drop is recorded one meter from tube's exit as mentioned in experiments by Wurtz and this is reflected in the CTF model.

Figure 4-3 and Figure 4-4 shows that the CTF (base version) overpredicts pressure drop for adiabatic and diabatic test conditions for these annular flow tests. The mean absolute percentage error for these runs is ~140% (adiabatic) and ~89% (diabatic). It is postulated that this overprediction is mainly caused by the interfacial friction factor models since previous tests on single-phase flow showed accurate CTF pressure drop predictions.

While there is considerable improvement in the predictions using the Lane model option in CTF for annular flow, the performance still shows systematic offsets, in particular for the diabatic tests. The mean absolute percentage error using Lane model prediction is ~13% (adiabatic) and ~36%

(diabatic). To study the effect of interfacial friction models, the CTF source code is modified to include six new options for interfacial friction predictions. Figure 4-5 to Figure 4-7 shows the predicted pressure drop using Ju, Lane, Belt, Quiben and Sun models. These comparisons are for the adiabatic test cases with outlet flow quality greater than 20%.

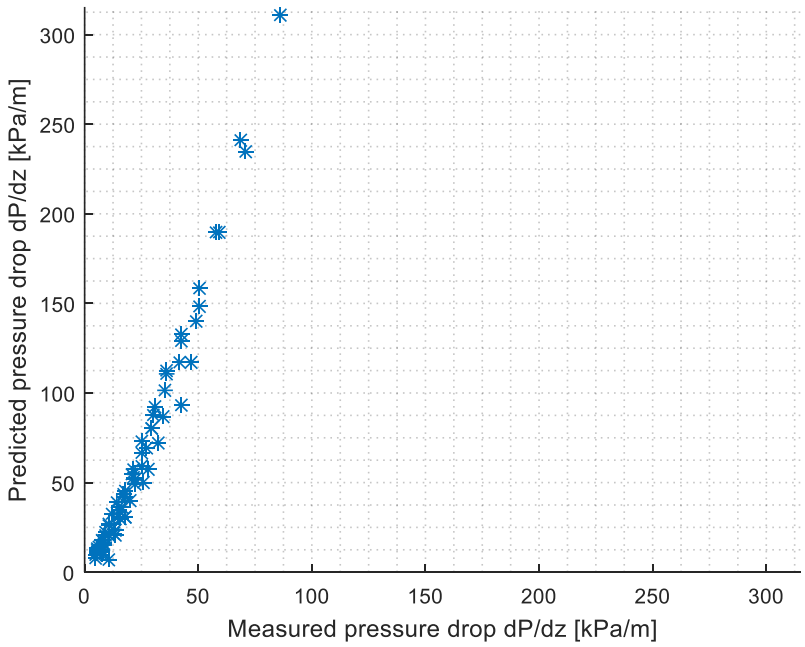

Figure 4-3 Predicted [CTF] pressure drop vs. measured [experimental] pressure drop for adiabatic cases using base CTF for P=30 to 90 [bar]

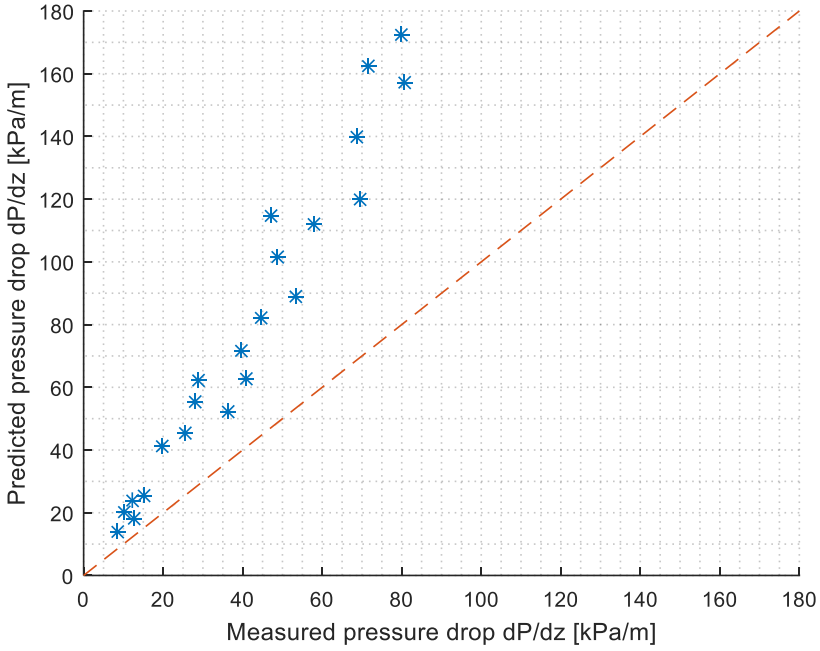

Figure 4-4 Predicted [CTF] pressure drop vs. measured [experimental] pressure drop for diabatic cases using base CTF at P=70 [bar]

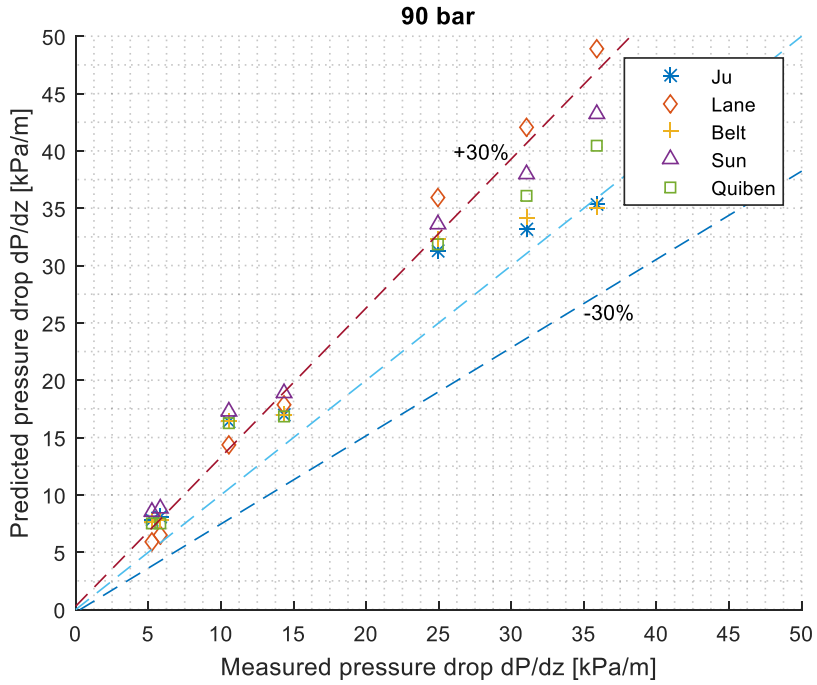

Figure 4-5 Predicted [CTF] vs. measured [Experimental] pressure drop for adiabatic cases using alternate IFF correlations [P=90 bar]

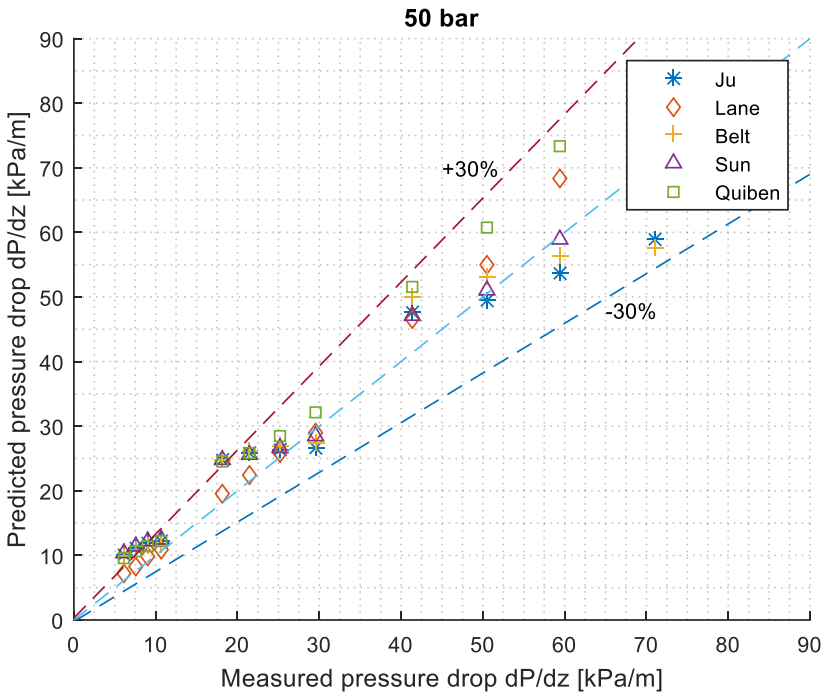

Figure 4-6 Predicted [CTF] vs. measured [Experimental] pressure drop for adiabatic cases using alternate IFF correlations [P=50 bar]

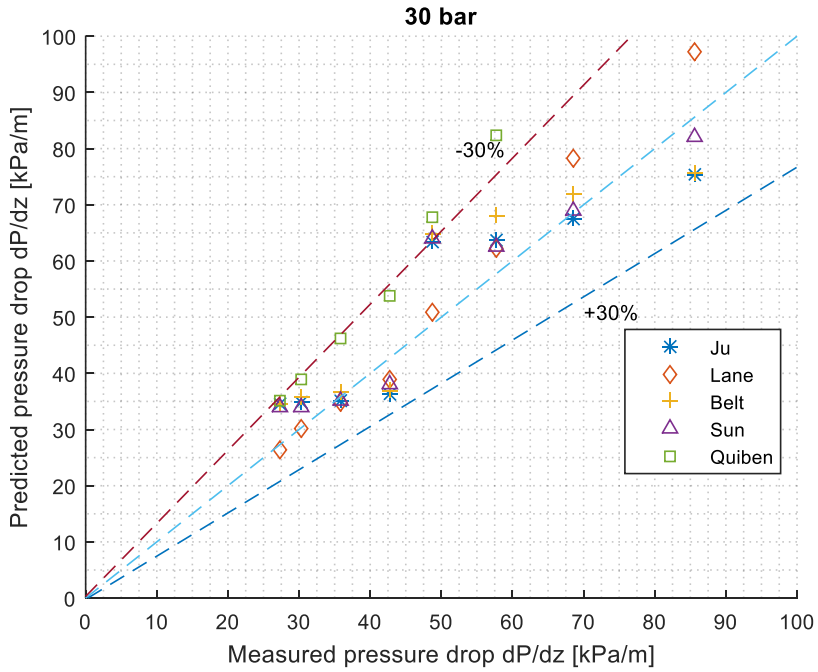

Figure 4-7 Predicted [CTF] vs. measured [Experimental] pressure drop for adiabatic cases using alternate IFF correlations [P=30 bar]

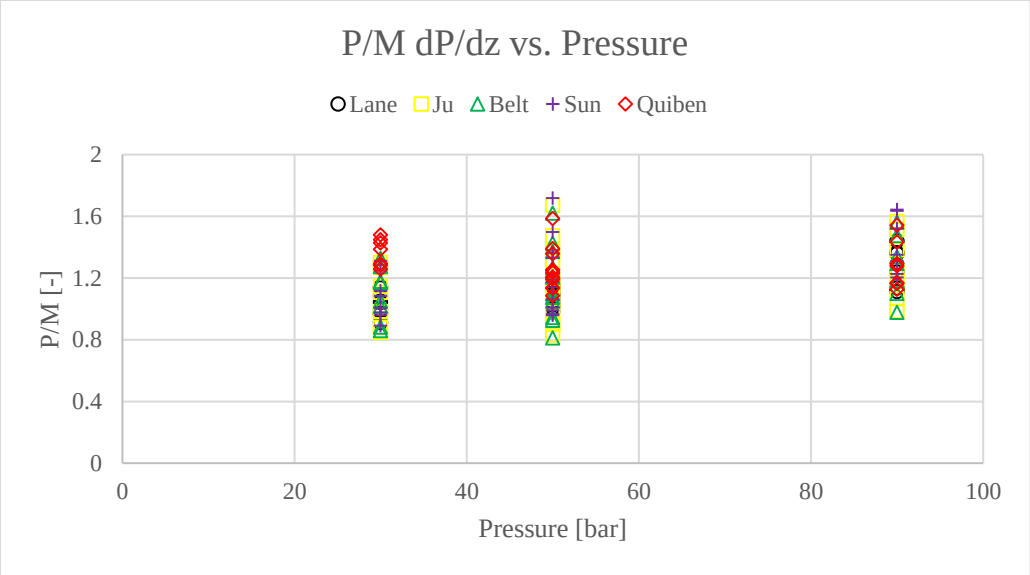

Figure 4-8 P/M vs. outlet pressure for RISO adiabatic cases using alternate IFF correlations

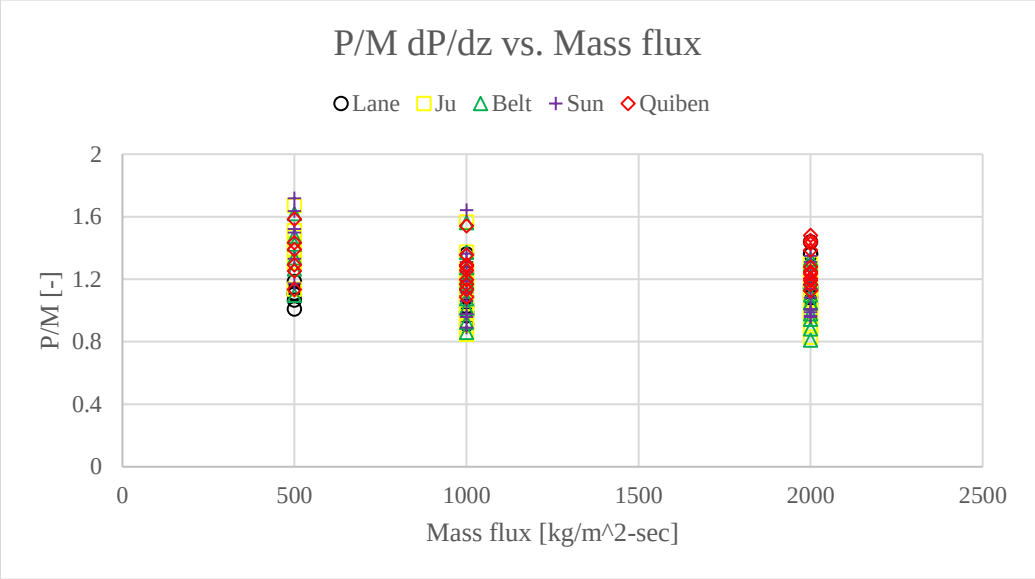

Figure 4-9 P/M vs. mass flux for RISO adiabatic cases using alternate IFF correlations

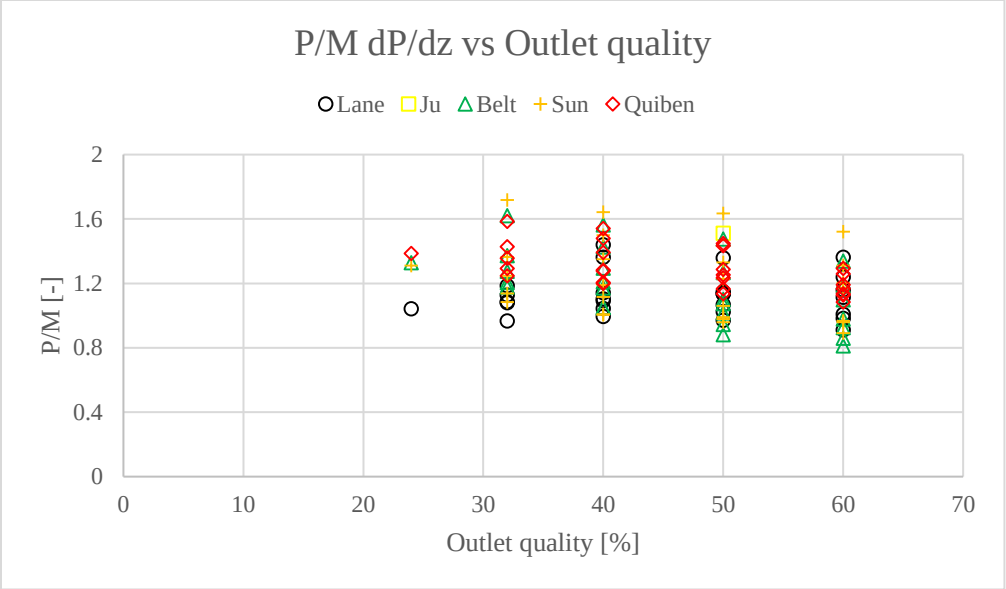

Figure 4-10 P/M vs. outlet quality for RISO adiabatic cases using alternate IFF correlations

Table 4-1 Statistical parameters comparison of different IFF correlations for adiabatic test conditions (Outlet flow quality > 20%)

Correlation	Avg. P/M	S.D	RMSE	R^2	Mean absolute % error
Base	2.80623395	0.384242	1.846652	0.444448	180.6234
Ju	1.16413308	0.225814	0.279162	0.919398	21.64249
Lane	1.12152267	0.130859	0.178583	0.944598	13.44197
Sun	1.21774338	0.228528	0.315654	0.938584	23.67441
Belt	1.17402197	0.208593	0.271652	0.912081	21.83439
Quiben	1.29216639	0.129846	0.31972	0.838593	29.21664

Table 4-1 and Table 4-2 shows the results for a subset of data that includes only outlet qualities above 20%, and the results using all the test data, respectively. In terms of performance, one can see that the Lane model performs better when considering only a subset of the data with high quality (greater than 20%) and adiabatic conditions, but when assessing against all data there is little improvement compared to the Base CTF model.

The main findings from Figure 4-11 to Figure 4-14 are: 1) Ju's correlation predicted the pressure drop results with the least error among all correlations 2) for cases with high mass flux and outlet flow quality (> 50%), the predicted to measured pressure drop gets closer to unity (1).

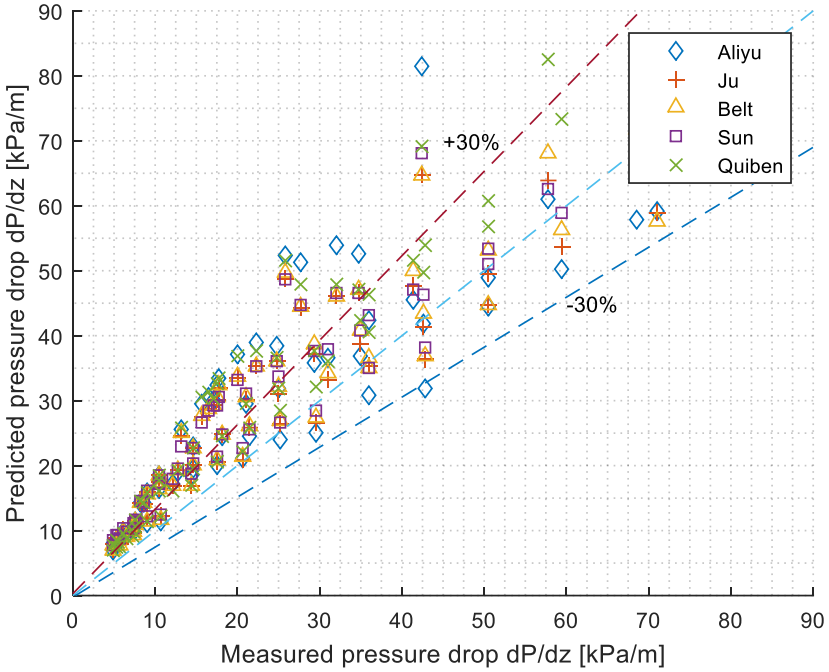

Figure 4-11 Predicted [CTF] vs. measured [Experimental] pressure drop for adiabatic cases using alternate IFF correlations [P=30-90 bar]

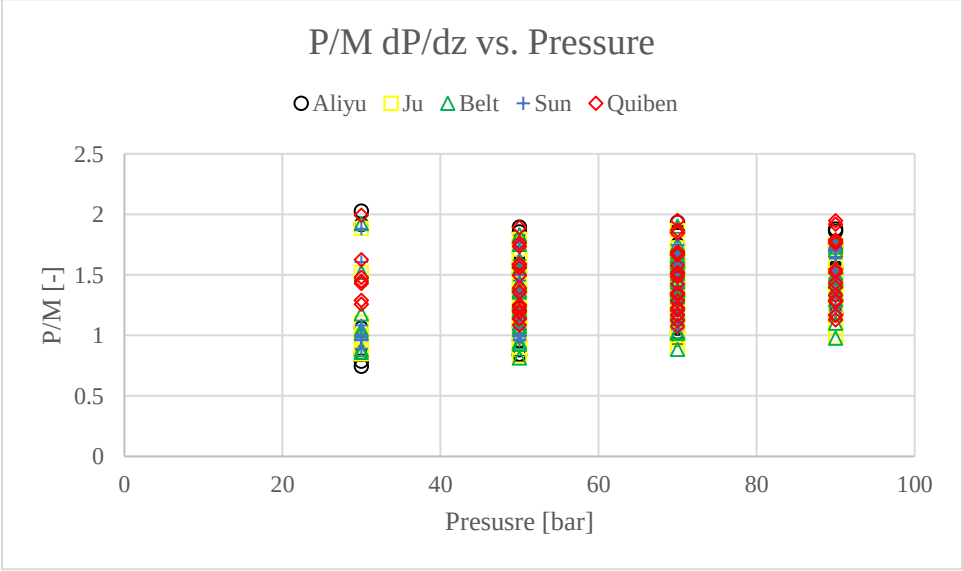

Figure 4-12 P/M vs. Outlet pressure for RISO adiabatic cases using alternate IFF correlations

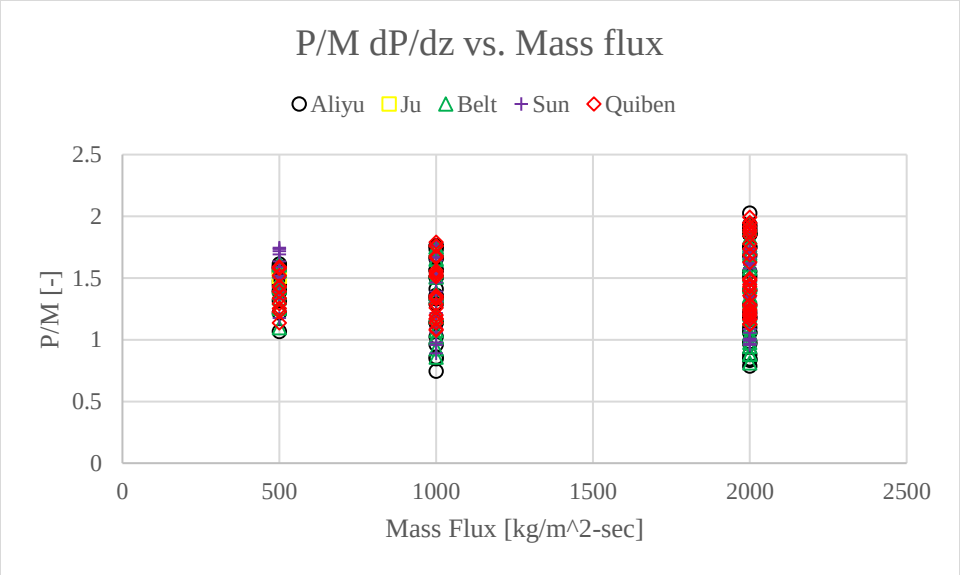

Figure 4-13 P/M vs. Mass flux for RISO adiabatic cases using alternate IFF correlations

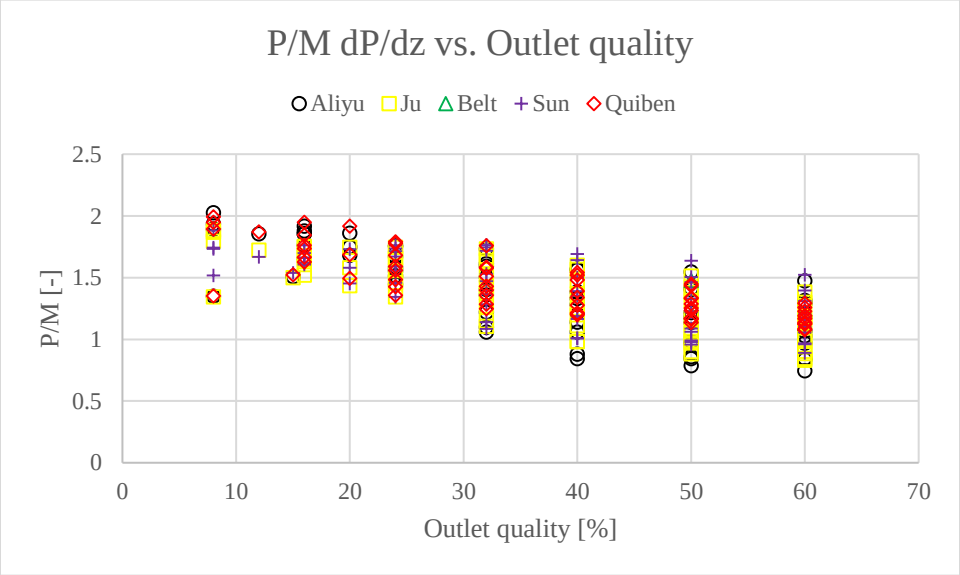

Figure 4-14 P/M vs. Outlet quality for RISO adiabatic cases using alternate IFF correlations

Table 4-2 Statistical parameters comparison of different IFF correlations for adiabatic test conditions (Includes all outlet flow qualities)

Correlation	Avg. P/M	S.D	RMSE	R^2	Mean absolute % error
Base	8.89057003	5.847759	9.821272	0.517988	142.6184
Ju	1.36981586	0.295486	0.473366	0.802522	39.72418
Aliyu	1.39213054	0.346777	0.52347	0.717978	43.9117
Sun	1.41530526	0.272478	0.496712	0.820421	42.35797
Belt	1.37626909	0.28791	0.473784	0.803244	39.92806
Quiben	1.44945291	0.252465	0.265747	0.798337	44.94529

A total of 22 diabatic cases are run in CTF. The diabatic length of the test section is 4.02m.

As pressure tap locations are not mentioned in Wurtz report for diabatic cases, one must assume the pressure tap locations. Thus, we performed CTF simulations using several pressure tap locations and compared them to a small number of low-power tests in order to assess the likely pressure tap locations. For these scoping tests we extracted the pressure drop from CTF at 0.25m, 0.50m, 0.75m and 1m from the test section exit. The pressure drop results obtained at 0.25m shows the best agreement and hence this position is assumed for all subsequent comparisons. Hence, the results in Figure 4-15 to Figure 4-17 show that the Sun and Ju correlations show the best level of agreement, in particular at low mass flow rates, for these diabatic tests. Table 4-3 shows summary of the results using each interfacial friction factor correlations. The mean absolute percentage error of pressure drop in diabatic two-phase conditions is improved from ~89% to ~26% and 31% for Sun and Ju correlations respectively.

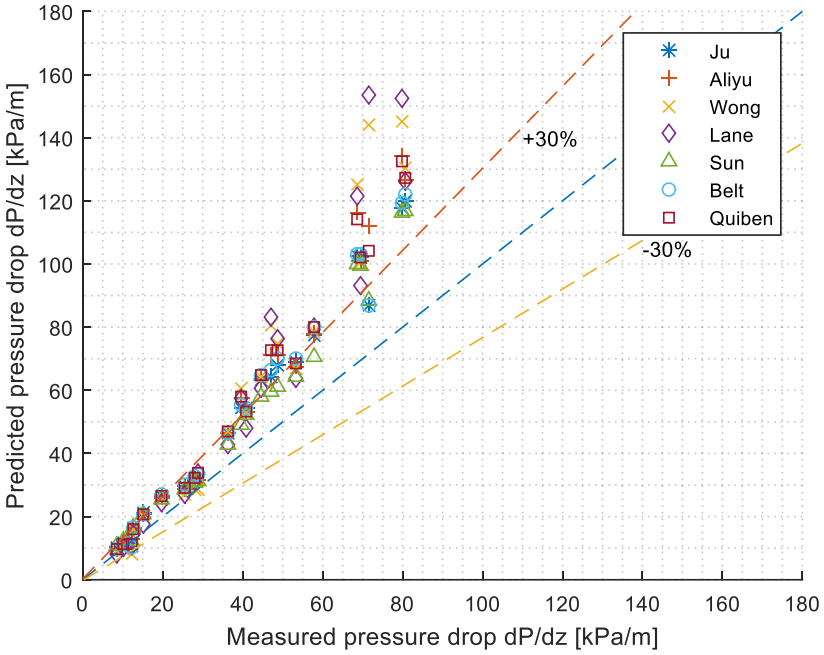

Figure 4-15 Predicted [CTF] vs. measured [Experimental] pressure drop for diabatic cases using alternate IFF correlations [P=70 bar]

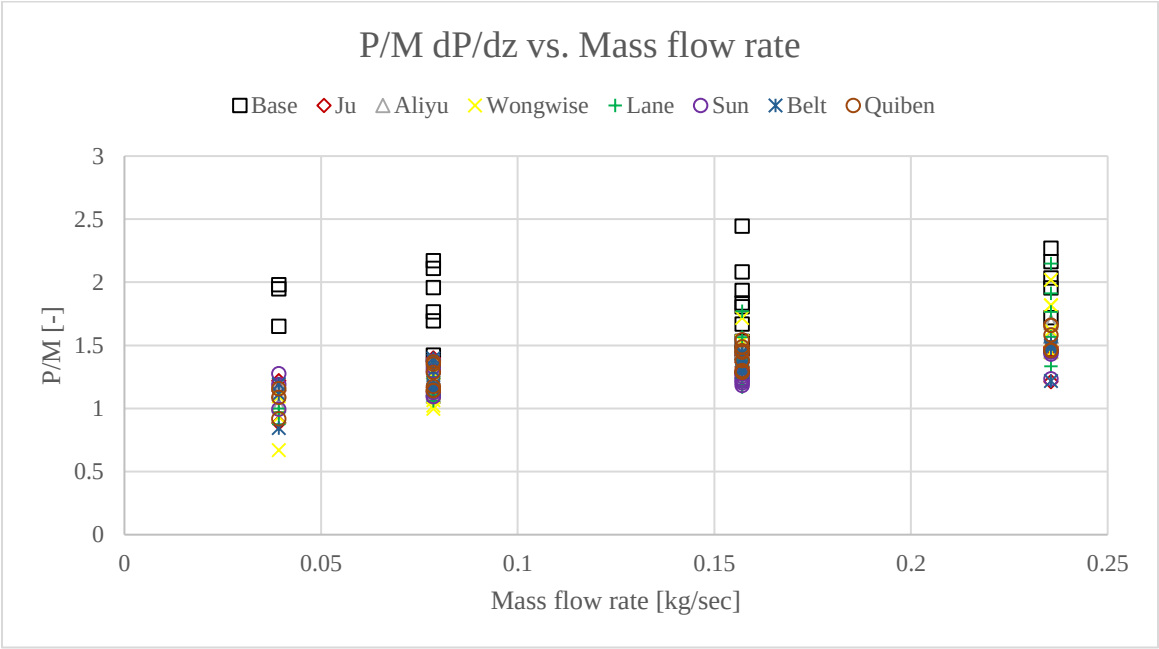

Figure 4-16 P/M vs. mass flow rate for RISO diabatic cases using alternate IFF correlations

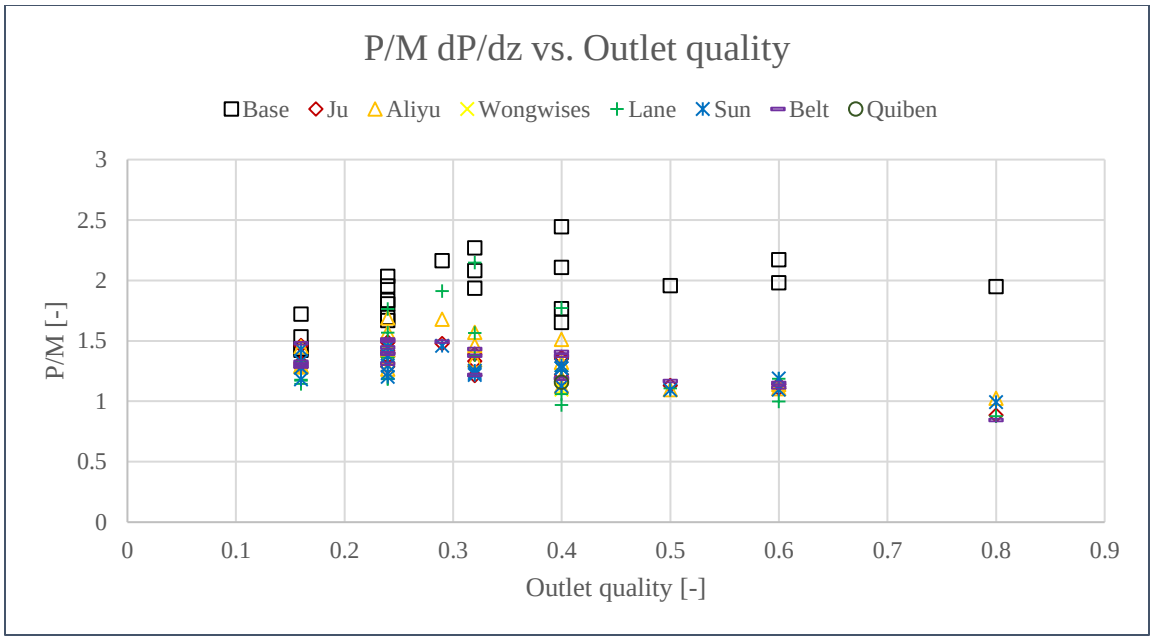

Figure 4-17 P/M vs. outlet flow quality for RISO diabatic cases using alternate IFF correlations

Table 4-3 Statistical parameters comparison of different IFF correlations for diabatic test conditions

Correlation	Avg. P/M	S.D	RMSE	R^2	Mean absolute % error
Base	1.89026861	0.259412	0.927293	0.518984	89.02686
Ju	1.30036408	0.146186	0.334049	0.770404	31.07611
Aliyu	1.34852452	0.185165	0.394658	0.720207	34.85245
Wongwises	1.35479420	0.317089	0.475841	0.680370	39.11504
Lane	1.34435548	0.319053	0.469442	0.676069	35.83731
Sun	1.26061256	0.121153	0.287397	0.802988	26.11355
Belt	1.31482209	0.157391	0.351973	0.568539	32.89292
Quiben	1.34776542	0.187399	0.395043	0.721897	35.51535

Given the adiabatic and diabatic results, it is concluded that the interfacial friction factor and liquid film models in CTF require further improvements. More specifically, it has been shown that a survey of a wide range of interfacial models fail to accurately predict two-phase annular film pressure drop for these experiments. Out of the six interfacial friction correlations examined, the Sun and Ju models obtained the best results (with higher R^2 values and lower standard deviation). In the view of these results, future work should examine the parameters such as liquid film thickness, droplet fraction and void fraction and ideally use realistic boiling conditions to generate

experimental data related to interfacial phenomenon. Most notably there is a lack of reliable liquid film thickness and wave properties under annular film boiling conditions that accompany any pressure drop measurements.

4.2 28-element CANDU rod bundle analysis

4.2.1 Pressure drop prediction

To assess CTF behavior in the annular flow regime for a complex geometry, test cases are modeled for horizontal 28-element CANDU rod bundle with bearing pads, spacer pads, and endplates. Experimental pressure drop is measured using thirteen pressure taps at different locations in the channel. The first pressure tap is located at the middle of the first bundle (just upstream of the spacer plane) while the last pressure tap is at the exit of the channel. These have recently been defined in an international benchmark for CANDU pressure drop prediction as outlined in Chapter 3. The test case naming conventions and discussions are consistent with the specifications (Novog, 2019).

Case 1.11 considers diabatic flow under single-phase conditions. The pressure drop predicted by CTF lies within ~4% of absolute error with one outlier at ~8%. Hameed's rod friction factor and uniform K-factors are used in the CTF model. The results predict an overall excellent agreement of the single-phase models. Figure 4-18 shows some fluctuations for different pressure taps (usually caused by experimental uncertainties) while the data obtained from CTF is uniform as expected based on the uniform input geometries.

The second case, case 1.12, is diabatic test where boiling initiates part-way through the channel. The CTF pressure drop prediction for pressure taps DP1 – DP6 lies within ~ 2-3 % error and are single-phase conditions. CTF starts overpredicting pressure drop from DP7 and this overprediction

can reach to ~25% in some locations. A slight decrease in the pressure drop for DP-13 in both measured and predicted results is seen in Figure 4-18. This is due to the fact that the heat input for DP-13 is lower (as half of the length is unheated) as compared to DP-12.

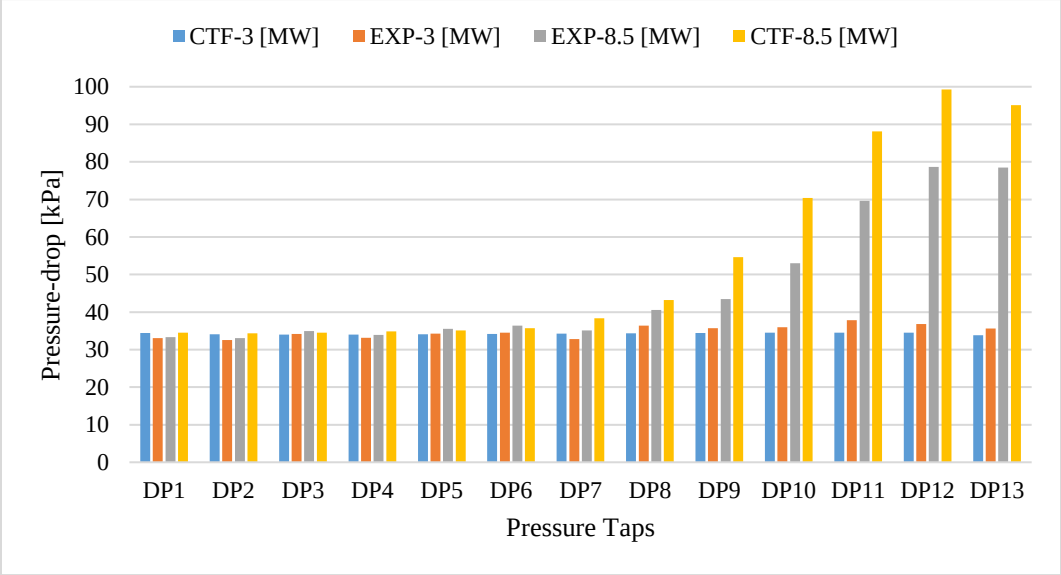

Figure 4-18 Pressure drop comparison between predicted (CTF) and experimental (EXP) results for single [3 MW] and two-phase [8.5 MW] conditions

4.2.2 Sensitivity analysis

While there is no specific benchmark data under different flow or bearing pads geometries available yet (they will be published at the end of 2021) several sensitivity studies are performed to assess the CTF predictions under the aforementioned test conditions. Subchannel flow rates are analyzed for subchannels located near the top and bottom of the channel to assess the impact of the lateral asymmetries on important thermalhydraulic phenomena.

Figure 4-19 and Figure 4-20 shows the subchannel flow rates for case 1.11 considering diabatic single-phase conditions with bearing pads height of 1.17 mm and 1.35 mm respectively. The fluctuations in subchannel flow rates are due to the presence of flow obstructions (Bearing pads,

Spacers pads, and end plates) in the CTF model. Apart from these fluctuations, the subchannel flow rates are relatively constant along the axial channel length for single-phase conditions.

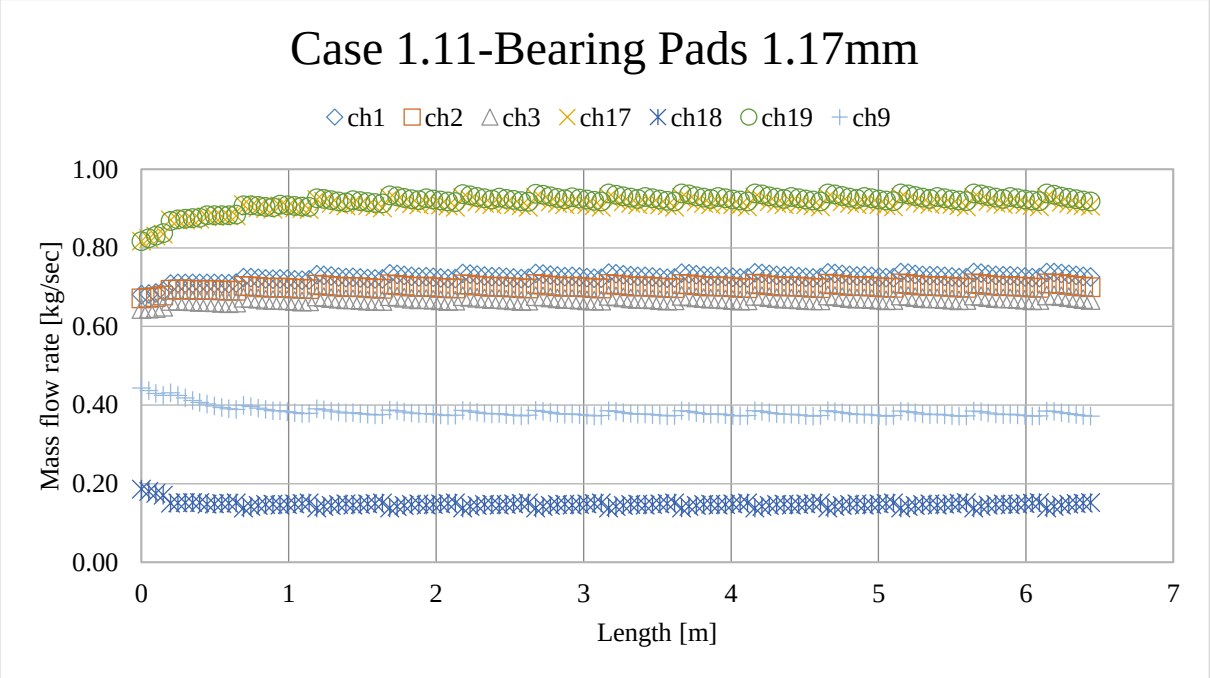

Figure 4-19 Mass flow rate [kg/sec] along the axial length [m] for uncrept single-phase conditions

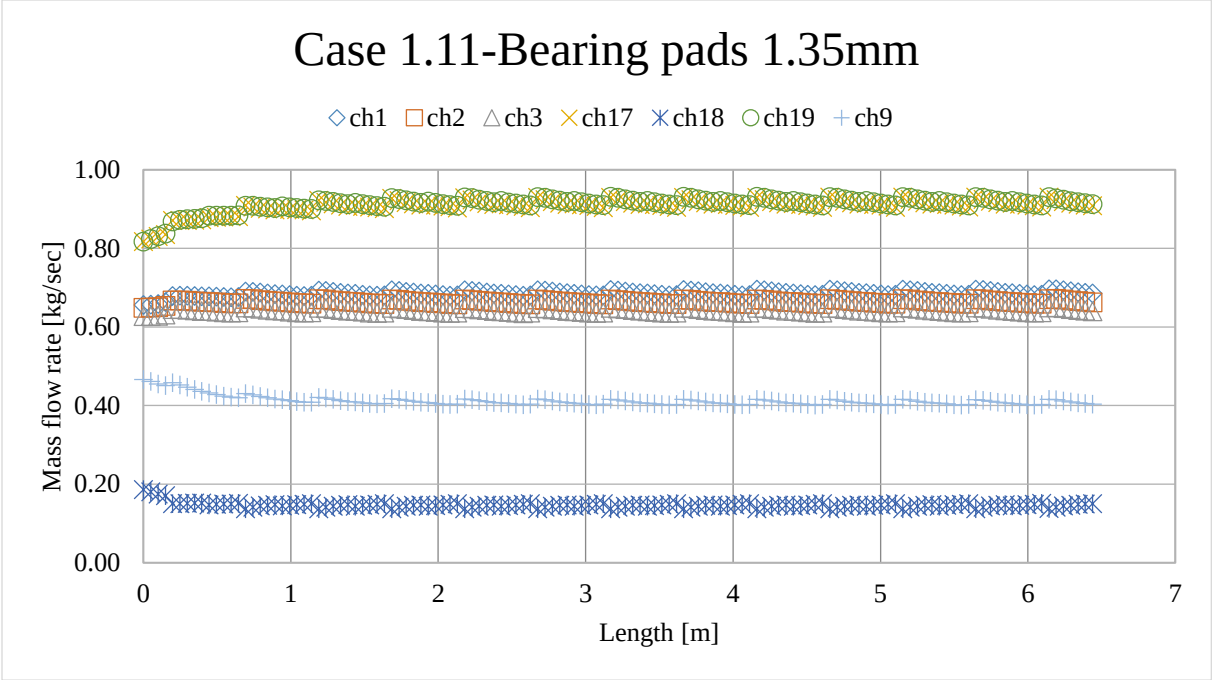

Figure 4-20 Mass flow rate [kg/sec] along the axial length [m] for uncrept single-phase conditions

Figure 4-21 and Figure 4-22 exhibits the subchannel flow rates for case 1.12 considering diabatic two-phase conditions in the test section with bearing pads height of 1.17 mm and 1.35 mm respectively. The subchannel flow rates show the impact of bearing pads on the top and the bottom subchannel flows. For the top subchannels (Subchannel No. 1, 2, 3), the subchannel flow rates increase with decreasing bearing pad height. On the other hand, for bottom subchannels (Subchannel No. 8, 9, 10), the subchannel flow rates increase with increasing bearing pad height. This is due to the fact that the bundle centerline has a slight offset from the PT centerline. Thus, the bundles rests on the bottom of the PT. This causes the change in the flow areas for the top and the bottom subchannels. In addition, a significant change in the subchannel flow rates can be observed part-way through the channel. This happens due to the influence of void generation as the boiling initiates part-way through the channel. Figure 4-23 and Figure 4-24 shows the

subchannel mass flux for case 1.12 considering diabatic two-phase conditions in the test section with bearing pads height of 1.17 mm and 1.35 mm respectively.

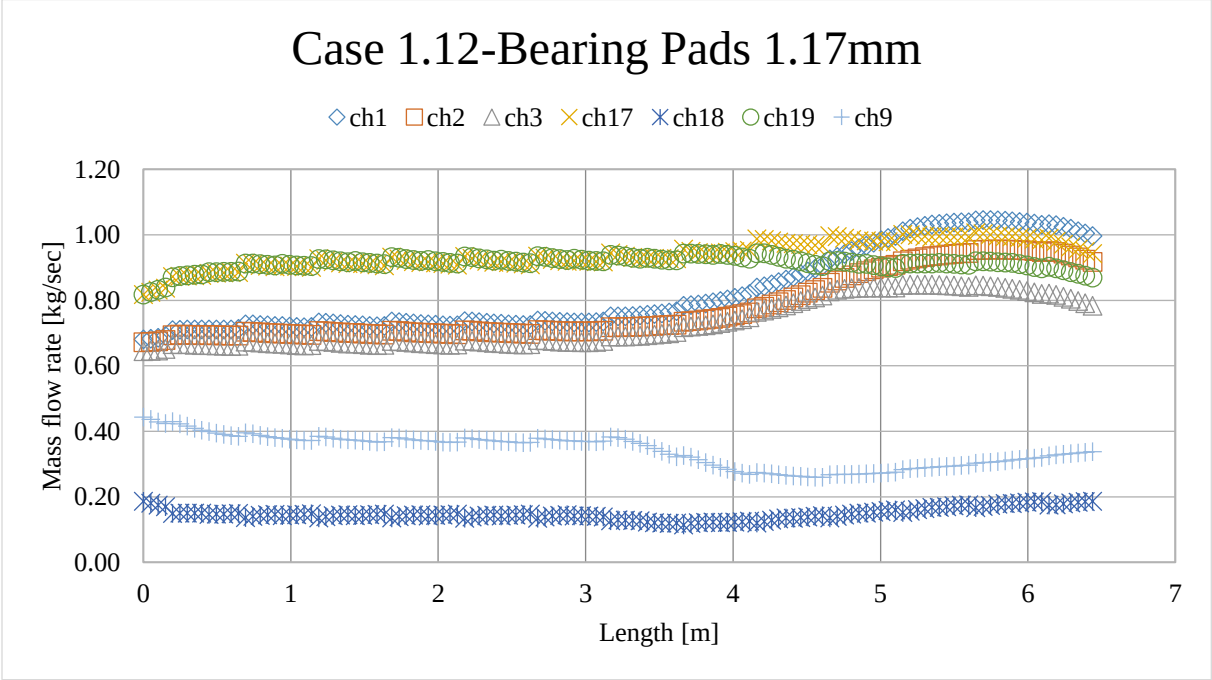

Figure 4-21 Mass flow rate [kg/sec] along the axial length [m] for uncrept two-phase conditions

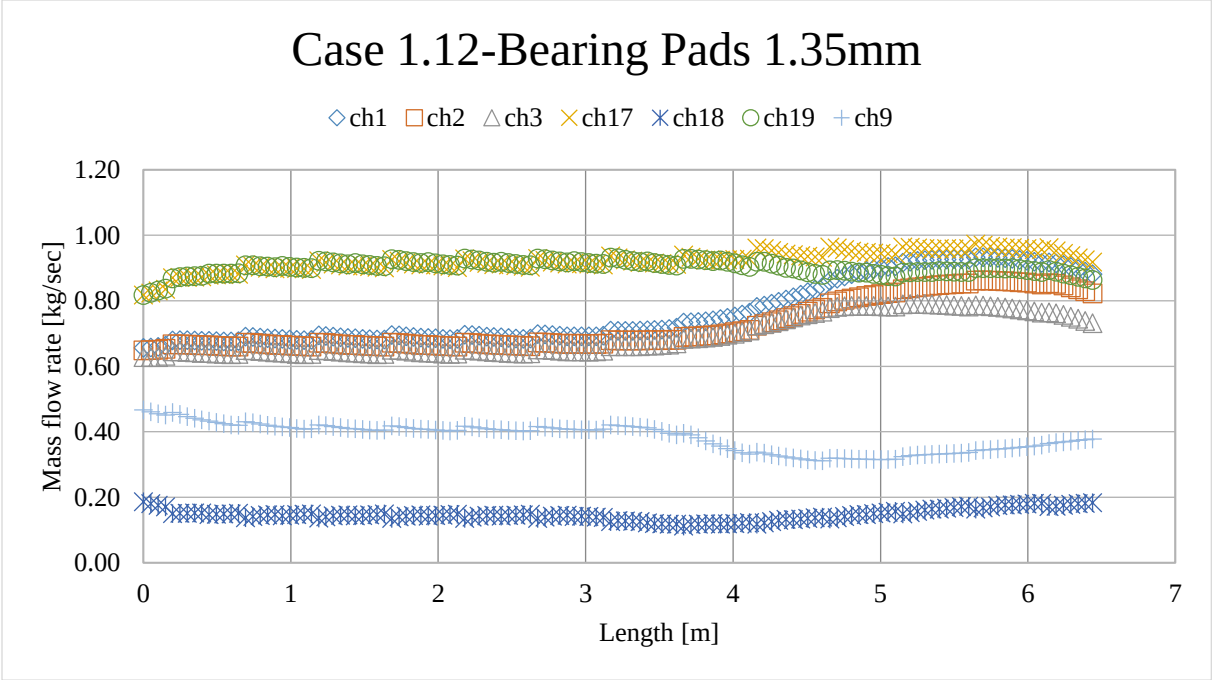

Figure 4-22 Mass flow rate [kg/sec] along the axial length [m] for uncrept two-phase conditions

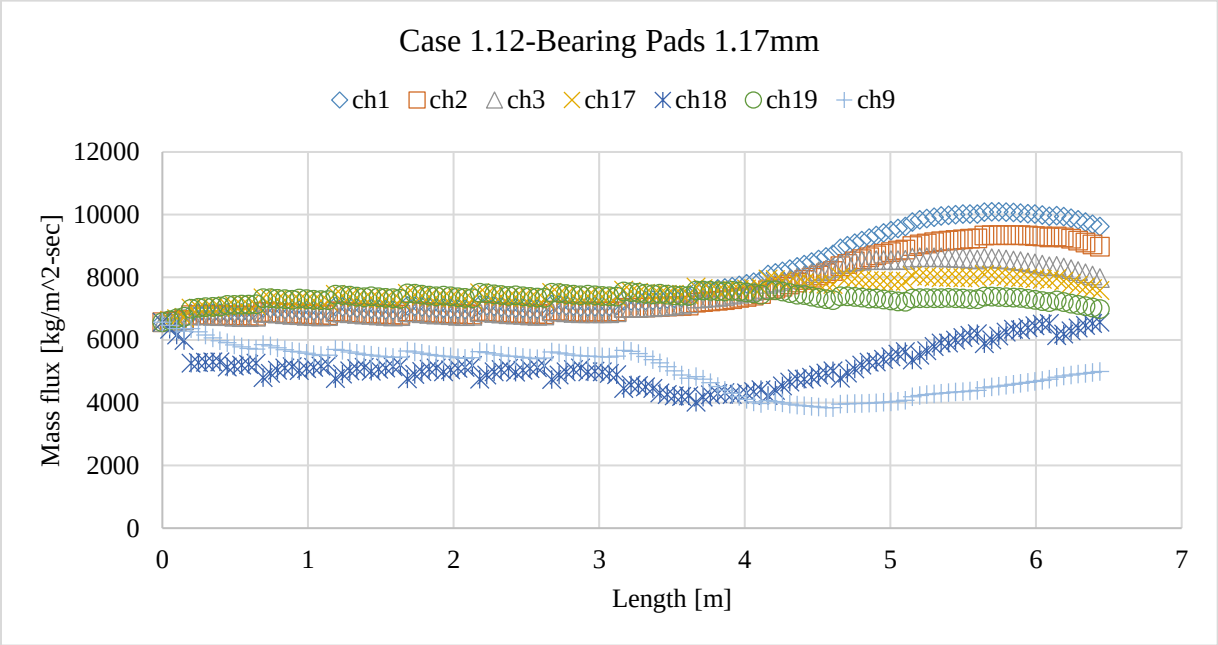

Figure 4-23 Mass flux [kg/m^2-sec] along the axial length [m] for uncrept two-phase conditions

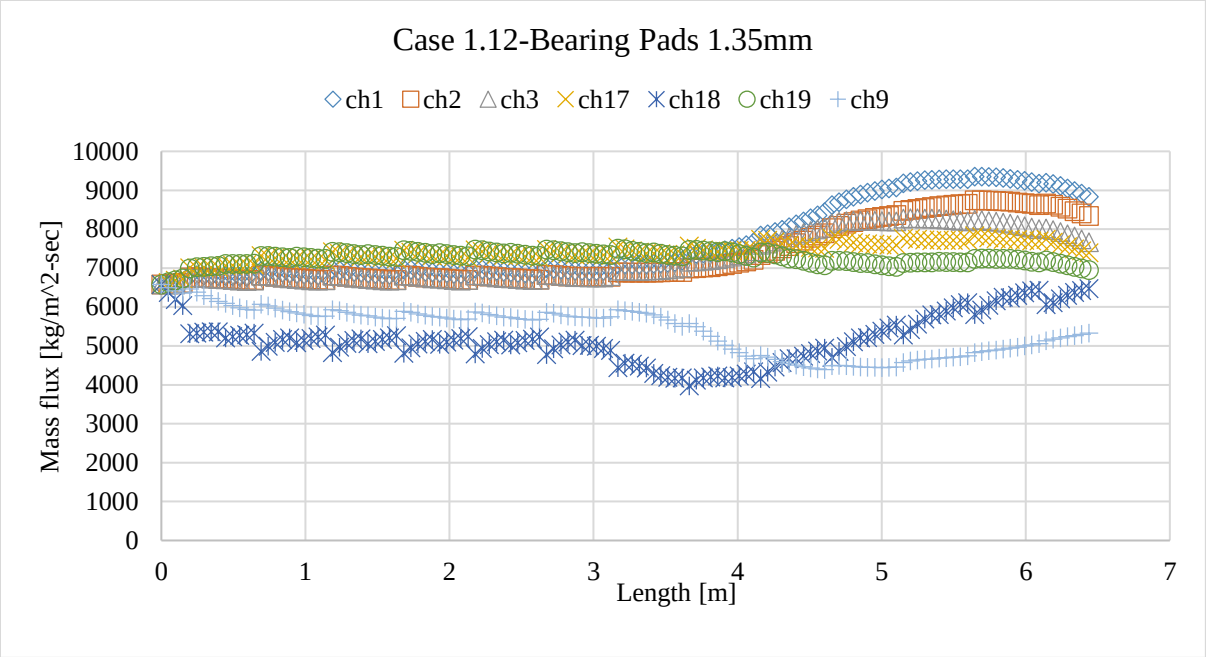

Figure 4-24 Mass flux [kg/m^2-sec] along the axial length [m] for uncrept two-phase conditions

To better observe the impact of eccentricity on fuel thermalhydraulics the sensitivity studies are performed for the crept PT. Figure 4-25 and Figure 4-26 represents the subchannels flow rates for diabatic crept PT case under single-phase conditions with different bearing pads height. The crept diameter used in 28-element rod bundle is 3.3% of the nominal PT diameter. The crept diameter increases from nominal PT diameter along channel's axial length. The crept diameter increases to a maximum increase of 3.3% of nominal diameter at 4.334m from the channel inlet. After this axial location, the diameter starts decreasing reaching the nominal PT diameter at channel's exit. The 28-element bundle geometry is left-to-right symmetric. Due to this, the outer ring subchannels [1-16] flow areas and wetted perimeters change as PT diameter changes. Figure 4-25 and 4-26 depicts the significant change in top subchannels flow rates for the crept PT caused by the increase in subchannel flow area as the PT diameter increases. The flow rates decrease back towards their inlet values in the latter half of the channel where the PT is decreasing in diameter. However, at the exit of the test section there is a slight decrease in middle ring subchannel (e.g., 17, 19) flows

relative to their initial values. This decrease in flow rates may occur as the flow tends towards larger flow area subchannels (e.g., 1, 2).

Figure 4-27 and Figure 4-28 shows the subchannel flow rates for crept PT under two-phase conditions. The sudden changes in subchannel flow rates at the latter section of the subchannels is due to the initiation of voiding and void migration phenomena. Examining subchannel '9' flow rates in Figure 4-25and Figure 4-27, the flows are similar to those under single-phase conditions until the middle of the channel. There is a noticeable drop in this subchannel's flow rate after the onset of voiding (in Figure 4-27). For the other subchannels in these figures there are generally increases to the mass flow rates in larger subchannels and in the crescent formed above the bundle. Contrary to single-phase case, the flow distribution is very different at the outlet of the two-phase tests.

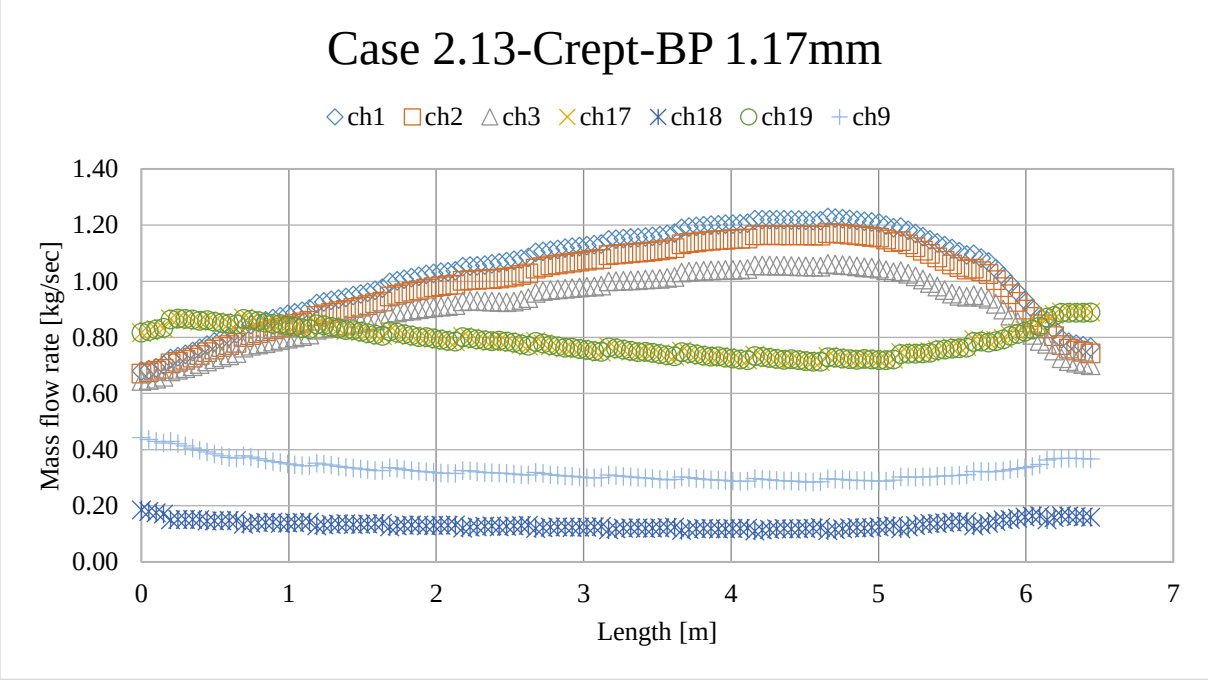

Figure 4-25 Mass flow rate [kg/sec] along the axial length [m] for crept single-phase conditions

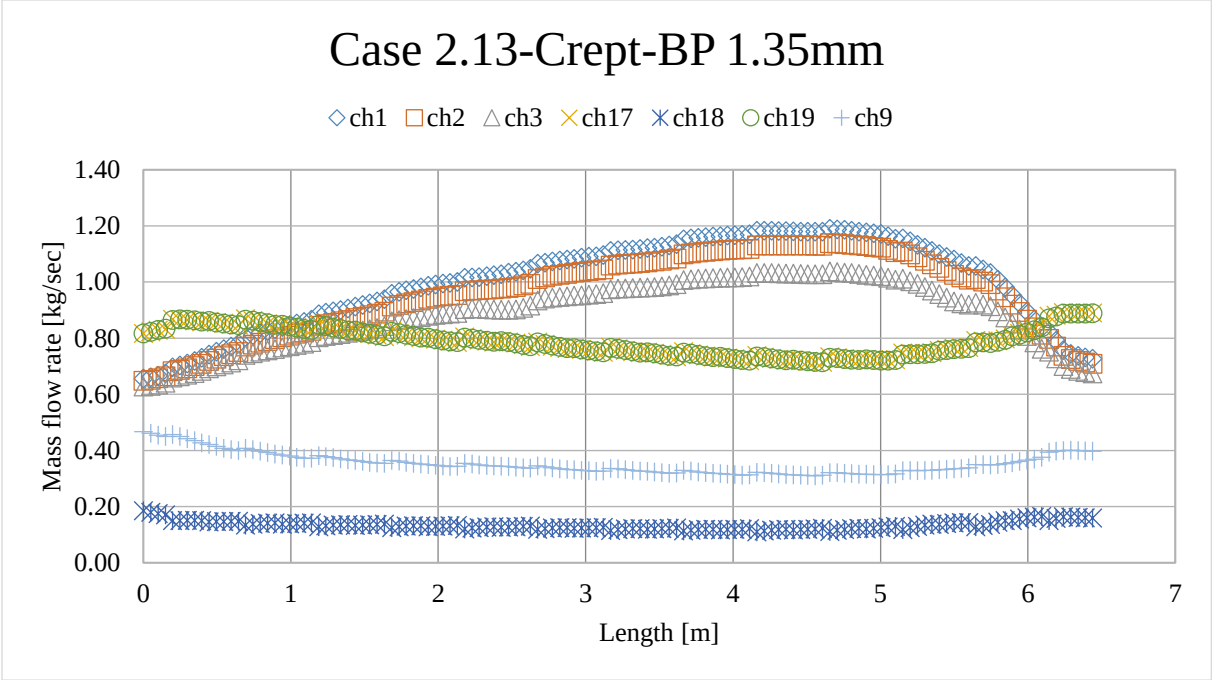

Figure 4-26 Mass flow rate [kg/sec] along the axial length [m] for crept single-phase conditions

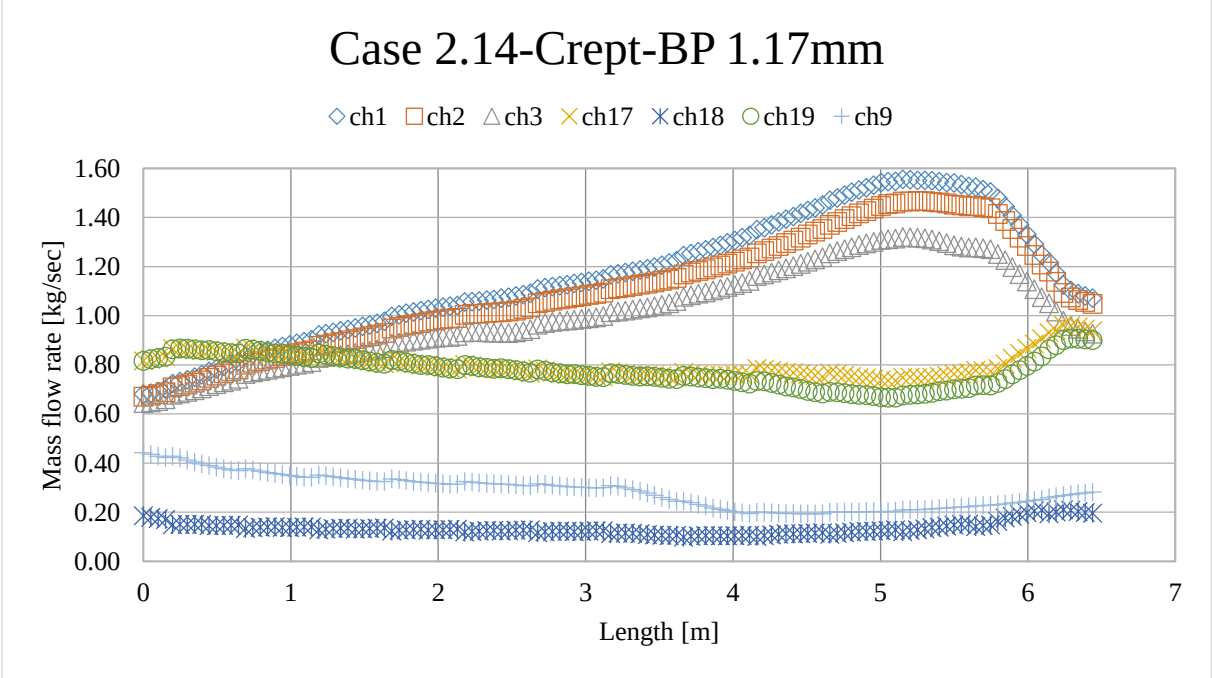

Figure 4-27 Mass flow rate [kg/sec] along the axial length [m] for crept two-phase conditions

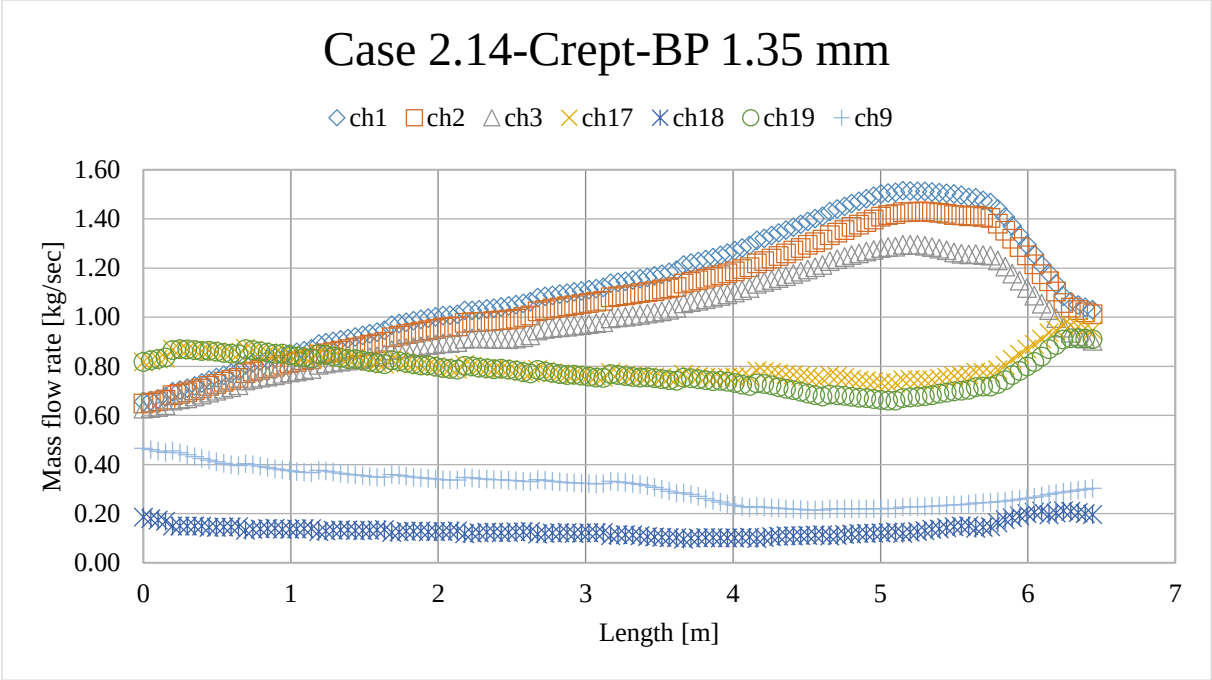

Figure 4-28 Mass flow rate [kg/sec] along the axial length [m] for crept two-phase conditions

4.2.3 Effect of alternate IFF correlations on subchannel mass flow rates

Figure 4-29 and Figure 4-30 shows the mass flow rates for top (subchannel 1) and bottom subchannel (subchannel 9) using alternate interfacial friction factor correlations. The subchannel '1' mass flow rate prediction using the alternate interfacial friction factor correlations in this thesis is invariant. This is expected since the exit quality for subchannel '1' is ~ 3.6% and the flow regime at the channel's exit is 'slug/large bubble flow'. Therefore since the flow regime is not annular the alternative interface friction correlations studies in this these are not invoked. The subchannel '9' mass flow rate prediction by alternate interfacial friction factor correlation have slight variations towards the end of the channel. The exit quality for subchannel '9' is 11.11% and the flow regime at the channel's exit is 'churn flow'. Further studies should examine high power levels where the flow rates become predominantly annular to study the effect of interfacial friction factors on subchannel flows and mixing.

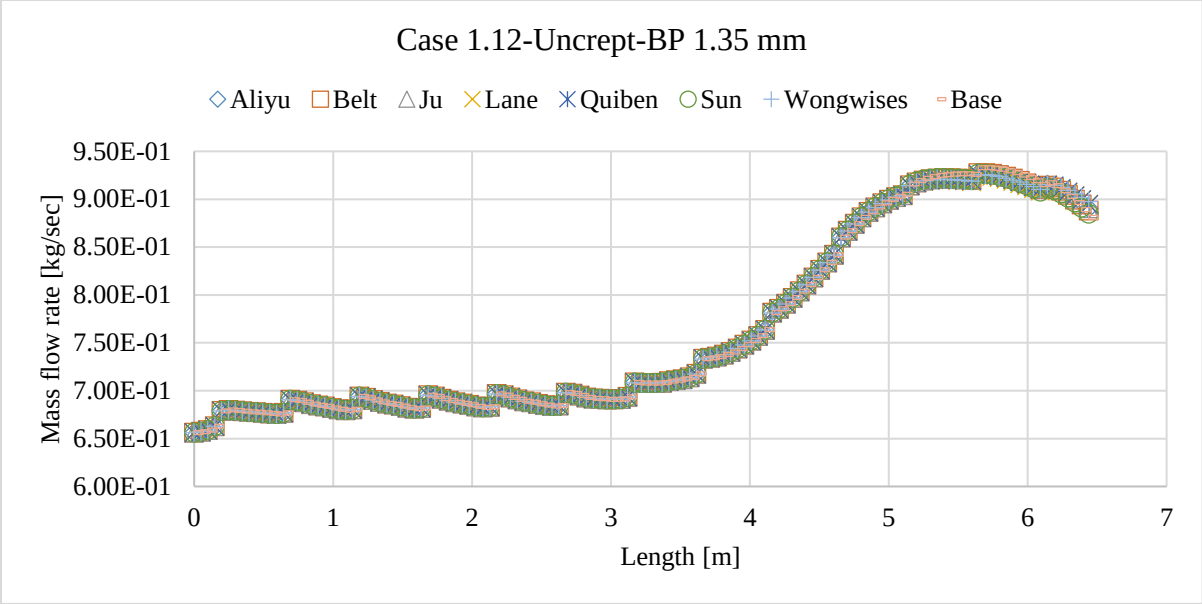

Figure 4-29 Subchannel 1 mass flow rate [kg/sec] along the axial length [m] using alternate IFF correlations

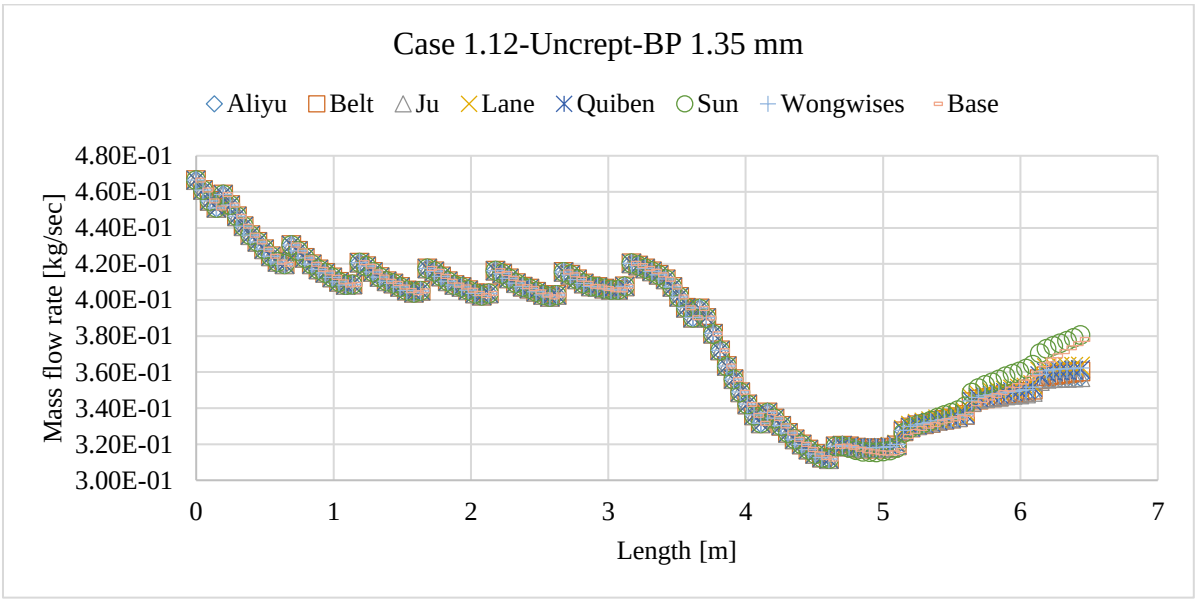

Figure 4-30 Subchannel 9 mass flow rate [kg/sec] along the axial length [m] using alternate IFF correlations

4.2.4 Enthalpy imbalance factor

Figure 7-1 and Figure 7-2 shows the enthalpy imbalance factors for an uncrept PT under two-phase conditions. These imbalance factors are obtained for subchannels along the axial length of the channel. The plots show that the imbalance factors for the bottom subchannels are greater than the

top subchannels. This behavior is similar for 1.17mm and 1.35mm bearing pads geometries. While the only difference lies in the magnitude of the imbalance factors as the flow area for outer ring subchannels [e.g., 1-16] change.

Figure 7-3 and Figure 7-4 shows enthalpy imbalance factors for crept PT under two-phase conditions. The main conclusions by comparing uncrept and crept cases are; a) the imbalance factor of bottom subchannels for crept cases is significantly greater than uncrept cases b) the bottom subchannels with smallest subchannels flow area (24, 26) have the highest imbalance factors at ~ 3.2m from the channel's inlet c) subchannel '25' in crept PT case has highest imbalance factor towards the exit of the channel d) the imbalance factors for top subchannels in case of the crept PT is lower than the uncrept PT case.

Enthalpy imbalance factors are also determined for all 41 subchannels at five different axial locations which are; 3.517m, 4.012m, 4.507m, 5.003m, and 5.498m. Figure 7-5 shows these factors for uncrept PT case with different bearing pads height. At the first axial location (3.517m), the middle ring subchannels with smallest flow areas (e.g., 22, 24, 26, and 28) have greater imbalance factors. The imbalance factors for these subchannels reduce along the axial length. For other subchannels the imbalance factors can be seen increasing at successive axial locations due to void migration. The imbalance factor for outer ring top subchannels increase with increasing bearing pad height.

Figure 7-6 shows the result for the crept PT case. By comparing Figure 7-5 and Figure 7-6 the results show that the imbalance factors of the subchannels in the upper-half of the crept channel is lower than the uncrept channel. While the imbalance factors of the subchannels in the lower-half of the crept channel is greater than the uncrept channel. Moreover, the imbalance factors of the

inner ring subchannels (35-39) increase significantly towards the channel's exist for the crept channel.

4.2.5 Effect of turbulent mixing on BEIN

Turbulent mixing is another important phenomenon which has significant effect on subchannel thermalhydraulic parameters. Due to this effect of turbulent mixing on BEIN, a total of six subchannels with different bearing pads height are analyzed. Figure 7-7 to Figure 7-17 shows the effect of turbulent mixing on these subchannels with different bearing pads height. The BEIN values are determined at three different axial locations which are; 3.517m, 4.012m and 4.507m. The main finding from these results are; a) There is no significant change in BEIN at high BETA values (BETA>0.05) indicating strong inter subchannel mixing, b) For 1.35mm bearing pads, the BEIN values are higher for top subchannels and lower for bottom subchannels c) The subchannels with small flow areas have greater BEIN initially. The plots presenting the effect of turbulent mixing on CHF and DNBR are mentioned in Appendix 'B' and 'C' respectively.

4.3 Incorporation and testing of R-134a fluid properties in CTF

A major impediment in further testing of CTF is that it lacks the capability to simulate R-134a fluids and given there is a large database of R-134a two-phase tests there is an opportunity to expand CTF testing by using these modeling fluid experiments. An additional aspect of this thesis is to extend CTF for application and validation using refrigerants. The current CTF version only supports fluid properties for water and FLiBe salts. By adding R-134a fluid properties, the testing and validation range of CTF is broadened for different experiments performed using R-134a fluids.

In CTF, user can select from six fluid property table options in CARD GROUP 1.1. Table 4-4 presents the fluid property options obtained from CTF user manual.

Table 4-4 Fluid property tables selection options in CTF

Option No.	**Fluid Property Tables**
0	Original CTF water property tables (mix of various sources)
1	IAPWS IF97 water property tables (direct correlation evaluations)
2	IAPWS AF97 water property tables, using a second-order central difference approximation for property derivatives w.r.t temperature and pressure.
3	IAPWS water property tables (lookup tables are generated from the direct correlation evaluations using option 1, so this method will have some error but performs much faster)
4	User defined fluid property
11	FLiBe liquid salt property calculations

There are two approaches to incorporate fluid properties in CTF. The first approach is to select option '4'. Upon selecting this option, the fluid properties are added in a separate file and then linked to the input file. This option is recommended as this gives the user flexibility to add various fluid properties. For the current study, this option is not selected as it is not fully functional in CTF at the time of this work. We also noted several hard coded water properties within the correlations inside CTF what must be adjusted depending on the fluids examined. The second approach, and that used in this thesis, is to replace water properties by R-134a fluid properties completely in the input files, and to manually update the various instances where water specific constants are hard coded in correlations or other CTF subroutines. For the current study, water properties are replaced with R-134a fluid properties in option '0'.

A total of thirteen saturated liquid and saturated vapor property tables are obtained at saturation pressure using NIST (USD211). CTF uses linear interpolation method to obtain desired fluid saturated properties at given local conditions. The state coefficients are obtained from literature for liquid specific volume, vapor specific volume, liquid enthalpy, and vapor enthalpy. These state coefficient are used to calculate derivative of density w.r.t pressure, and derivative of density w.r.t enthalpy for both phases (liquid and vapor). Finally, a least square method is used to develop

correlations for six superheated properties which are temperature, density, dynamic viscosity, thermal conductivity, specific heat capacity, and enthalpy.

The next step after incorporating the fluid properties is to validate it with different experimental data. In the current study the CTF is validated for CHF experiments. In CTF, user can select CHF correlation out of the five options. Table 4-5 shows these five options.

Table 4-5 CHF correlation selection option in CTF

Option No.	**Correlation**
<0	No Correlation (A very high value of CHF is assumed)
0	Standard correlation (Biasi)
1	W3 correlation
2	Bowring Correlation
3	Groenveld look-up tables

All the correlations in Table 4-5 are suitable for predicting CHF for water as working fluid. The two most common methodologies in CHF prediction are: Direct Substitution Method (DSM) and Heat Balance Method (HBM). DSM depends on local conditions such as local quality to predict CHF while HBM depends on upstream conditions such as inlet sub cooling and distance from test section's inlet for CHF prediction (Shah, 1987). In order to predict CHF for R-134a fluid, (Katto, et al., 1984) correlation (HBM) and CHF LUT (DSM) are implemented in the CTF code. To use water LUT, fluid-to-fluid scaling is performed to obtain R-134a CHF prediction. Figure 4-49 and 8 and 4-49 shows the comparison of predicted to experimental critical power results using HBM and DSM prediction methods for Liu's and Chun's experiment respectively.

A complete research paper (under review) on this study is presented in the Appendix.

5 Conclusions

This thesis focused on testing, refinement and incorporation of R-134a fluid properties in CTF with the overall objective of improving two-phase flow modeling in the annular flow regime. The RISO experiments are modeled in CTF for adiabatic and diabatic test conditions. CTF significantly overpredicts the pressure drop in annular flow regime. This overprediction is caused by over estimation in frictional pressure drop. A survey of wide range of interfacial friction factors was carried out. Six interfacial friction factors models were added in CTF source code. The pressure drop predictions by Sun and Ju correlations performed best, however they showed significant bias at high flow conditions. For adiabatic test conditions, the mean absolute percentage error was improved from ~142% to ~39%. Whereas for diabatic test conditions, the mean absolute percentage error was improved from ~89% to 26%. Given the results, we conclude that the interfacial and liquid film models needs further improvement. Given that the behavior is most noticeable at high mass fluxes, the focus may need to be on the rough or roll-wave sub-region of annular flow where there is the highest interface friction factors.

All these interfacial friction factor correlations appear to overpredict the pressure drop in annular flow conditions. The most significant variable in most of these interfacial friction models is liquid film thickness. This parameter is quiet strenuous to measure from experiments as it need high accuracy instruments and depends on many factors (E.g., liquid film and gas core flow rates, entrainment and deposition rates) . Due to this, liquid film thickness is calculated from available correlations in the literature which adds further uncertainty in interfacial friction factor prediction.

The interfacial friction models directly based on non-dimensional numbers provide improved results for pressure drop for annular two-phase conditions. The major reason behind non-dimensional numbers use in the models is as they can be obtained easily from flow conditions and

fluid properties but this can improve the accuracy to a certain limit. The non-dimensional numbers which are important to grasp the major phenomena in annular flows are Weber number, viscosity number, and Reynolds. The liquid film thickness in annular flow is mostly effected by two mechanisms which are: inertia force and surface tension force, where inertia force tends to change and surface tension tends to maintain the liquid-gas interface shape. This effect is represented by gas Weber number. The Reynold's number inclusion in correlation accounts for the inertia changes in the gas core.

This work also assessed the behavior of CTF against a small set of CANDU specific measurements. There was also a consistent overprediction of the pressure drop in two-phase conditions, investigation showed that for these tests there was noticeable changes in subchannel flows under two-phase crept conditions as compared to uncrept channels, and this will likely impact the dryout prediction significantly. This thesis also examined the effect of interface friction and subchannel mixing models for these limited tests and further work at higher power levels is needed to better quantify their impact.

Finally, R-134a fluid properties were added in CTF to extend its validation and verification database. For CHF comparison purposes, two CHF prediction methods are added in CTF; HBM and DSM. Katto's CHF correlation is used as HBM approach whereas fluid-to-fluid scaling is performed in CTF to obtain CHF prediction using water LUT which is DSM approach. The testing of CTF for these refrigerants covered primarily DNBR phenomena and some dryout tests. However, no pressure drop comparisons were made since these were not included in the literature available. Katto's correlation underpredicted critical power and DNBR. The standard deviation for LUT was slightly greater when compared with Liu's correlation but lies within acceptable range.

6 Future prospects

The results in this thesis clearly demonstrate the need for further refinement of the CTF annular film flow regime interface models. We have shown that a wide range of interfacial friction factors fail to predict the two-phase annular pressure drop from the experiments accurately. Hence, future prospects should consider the assessment of the liquid film thickness, droplet fraction and void fraction models. It appears to be most pronounced in the stable sub-regime of annular flow where the interfacial friction (or roughness) is highest.

Given that there is not a large database available in literature on steam-water annular flows at high operating pressure, the RISO experiment provides data of film thickness, film flow rates, pressure drops, wave frequencies and velocities, and burnout heat fluxes for more than 250 steam-water annular flow experiments. Hence, future work should also consider assessing the liquid film thickness, and liquid film flow rate prediction by CTF and comparing it with the RISO database. Furthermore, film thickness correlation suggested in some studies such as (Sun, et al., 2018) and (Quiben, et al., 2007) can be implemented in CTF and compared with the actual film thickness measurements in the RISO experiments.

In addition to this, fluid properties option '4' in CTF needs to be fully implemented by the developers. While this work used a brute force approach (replaced all water properties with R-134a, option '4' would allow a much more flexible approach to alternative fluid modeling. This will further broaden the validation and testing of CTF. Moreover, the future prospects in further validating the CTF for R-134a fluid properties should also consider the validation of pressure drop and void fraction with the measured databases.

References

Aliyu Aliyu Musa [et al.] Interfacial friction in upward annular gas-liquid two-phase flow in pipes [Journal] // Experimental Thermal and Fluid Science. - 2017. - Vol. 84. - pp. 90-109.

Andersen J G.M REMI/HEAT COOL, A Model for Evaluation of Cire Heat-up and Emergency Core Spray Cooling System Performance for Light-Water-Cooled Nuclear Power Reactors [Report]. - [s.l.] : Technical Report 296, RISO National Laboratory , 1973.

Asali J. C., Hanratty T. J. and Andreussi Paolo Interfacial Drag and Film Height for Vertical Annular Flow [Journal] // AIChE Journal. - 1985. - 6 : Vol. 31. - pp. 895-902.

Baniamerian Z., Mehdipour R. and Aghanajafi Cyrus Analytical Simulation of Annular Two-Phase Flow Considering the Four Involved Mass Transfers [Journal]. - [s.l.] : Journal of Fluids Engineering, 2012. - 8 : Vol. 34.

Belt R J, Van't Westende J M.C and Portela L M Prediction of the interfacial shear-stress in vertical annular flow [Journal] // International Journal of Multiphase Flow. - 2009. - Vol. 35. - pp. 689-697.

Beus S G A Two-Phase Turbulent Mixing Model for Flow in Rod Bundles. Technical Report WAPD-TM-2438 [Report]. - [s.l.] : Bettis Atomic Power Laboratory, 1971.

Carlucci L N, Hammouda N and Rowe D S Two-phase turbulent mixing and buoyancy drift in rod bundles [Journal]. - [s.l.] : Nuclear Engineering and Design, 2003. - Vol. 227.

Carver M. B. [et al.] VALIDATION OF THE ASSERT SUBCHANNEL CODE: PREDICTION OF CRITICAL HEAT FLUX IN STANDARD AND NONSTANDARD CANDU BUNDLE GEOMETRIES [Journal]. - [s.l.] : HEAT TRANSFER AND FLUID FLOW, 1995. - Vol. 112.

Cousins L B Liquid Mass Transfer in Annular Two-Phase Flow [Journal]. - [s.l.] : Symposuim on Two-Phase Flow, 1965. - Vol. 2.

CTF: ORNL [Online] // Oak Ridge National Laboratory. - March 22, 2021. - http://www.ornl.gov/onramp/ctf.

de Paula Junior C F and Lima L E M Comparison analysis of correlations for interfacial friction factor applied in gas-liquid annular flow in vertical pipes [Journal] // Engenharia Termica (Thermal Engineering) . - 2017. - 2 : Vol. 16. - pp. 54-61.

Hewitt G. F. and Hall-Taylor N. S. Annular Two-Phase Flow [Book]. - Oxford : Pergamon Press, 1970.

Holland F. A. and Bragg R. Fluid Flow for Chemical Engineers [Book]. - [s.l.] : Butterworth-Heinemann, 1995. - Vol. 2.

Hurlburt Evan T., Fore Larry B. and Bauer Richard C. A two zone interfacial shear stress and liquid film velocity model for vertical annular two-phase flow [Conference] // Proceedings of FEDSM2006. - Miami, FL : 2006 ASME Joint U.S. - European Fluids Engineering Summer Meeting, July 2006.

Ju Peng [et al.] Prediction of interfacial shear stress of vertical upward adiabatic annular flow in pipes [Journal] // International Journal of Heat and Mass Transfer. - 2019. - Vol. 133. - pp. 500-509.

Katto Y. and Ohno H. An improved version of the generalize correlation of critical heat flux for the force convective boiling in uniformly heated vertical tubes [Journal]. - [s.l.] : Int. J. Heat and Mass Transfer, 1984. - Vol. 27.

Lahey Jr. R T, Shiralkar B S and Radcliffe D W Two-Phase flow and heat transfer in multirod geometries: Subchannel and pressure drop measurements in a nine-rod bundle for diabatic and adiabatic conditions [Report]. - [s.l.] : General Electric, 1970.

Lane Jeffrey W. The development of a comprehensive annular flow modeling package for two-phase three-field transient safety analysis codes [Report]. - [s.l.] : Pennsylvania State University, 2009.

Liu Yang [et al.] Critical heat flux measurement and visualization in R-134a on vertical single rod with and without mixing-vane spacer: The characteristics and phenomenon of critical heat flux [Journal]. - [s.l.] : Annulas of Nuclear Energy, 2021. - Vol. Under Review.

McPherson M. D. THE USE OF ENTHALPY IMBALANCE IN EVALUATING THE DRYOUT PERFORMANCE OF FUEL BUNDLES [Report]. - Chalk River : Atomic Energy of Canada Limited, 1971.

Novog D. R. Plan for Specification for OECD-NEA Blind Benchmark on CANDU Thermalhydraulics [Report] : R&D. - [s.l.] : CANDU Owners Group Inc., 2019.

Pedras M H J Atrito Interfacial em Escoamento Anular Transicional, Master Thesis (in Portuguese) [Report]. - Campinas, SP : Faculdade de Engenharia Mecanica, Universidade Estadual de Campinas, 1993.

Quiben Jesus Moreno and Thome John R Flow pattern based two-phase frictional pressure drop model for horizontal tubes, Part II: New phenomenological model [Journal]. - [s.l.] : International Journal of Heat and Mass Transfer, 2007. - Vol. 28.

Salko R. [et al.] CTF Theory Manual. - 11 8, 2019.

Schubring D and Shedd T A Two-phase wavy-annular flow in small tubes [Journal] // International Journal of Heat and Mass Transfer. - 2009. - Vol. 52. - pp. 1619-1622.

Shah M Mohammaed Improved general correlation for critical heat flux during upflow in uniformly heated vertical tubes [Journal]. - [s.l.] : Heat and Fluid Flow, 1987. - 4 : Vol. 8.

SLIZ F. W. and BASEHORE K. L. VEPCO REACTOR CORE THERMAL-HYDRAULIC ANALYSIS USING THE COBRA IIIC/MIT COMPUTER CODE [Report]. - RICHMOND, VIRGINA : VIRGINA ELECTRIC AND POWER COMPANY, 1983.

Sun Baojiang [et al.] Interfacial Friction Factor Predition in Vertical Annular Flow Based on the Interface Roughness [Journal] // Chamical Engineering & Technology. - 2018. - 9 : Vol. 41. - pp. 1833-1841.

Thome John R and Cioncolini Andrea Encyclopedia of Two-phase Heat Transfer and Flow I [Book]. - [s.l.] : World Scientific, 2015. - Vol. 3: Flow Boiling in Macro and Microchannels.

Thurgood M. J. [et al.] COBRA/TRAC-A Thermal-Hydraulics Code for Transient Analysis of Nuclear Reactor Vessels and Primary Coolant Systems [Report]. - Richland : Pacific Northwest Laboratory, 1983.

US Department of Commerce [Online] // NIST: National Institute of Standards and Technology. - 2021. - https://www.nist.gov/..

Waddington G. M., Kiteley J. C. and Carver M. B. ASSERT VALIDATION AGAINST THE STERN LABORATORIES SINGLE-PHASE PRESSURE DROP TESTS [Conference] // CNS Simulation Symposium. - Chalk River : CNS, 1995.

Wallis G B [Journal] // Jbasic Eng.. - 1970. - Vol. 92. - p. 73.

Wallis G B Annular Two-Phase Flow [Journal] // Journal of basic engineering. - 1970. - pp. 59-72.

Wallis Graham B. One-dimensional Two-phase Flow [Book]. - [s.l.] : McGraw-Hill, 1969.

Webb B. COBRA-IV PC: A PERSONAL COMPUTER VERSION OF COBRA-IV-I FOR THERMAL-HYDRAULIC ANALYSIS OF ROD BUNDLE NUCELAR FUEL ELEMENTS AND CORES [Report]. - 1976.

Whalley P. B. and Hewitt G. F. The correlation of liquid entrainment fraction and entrainment rate in annular two-phase flow [Report]. - [s.l.] : AERE-R-9187, Harwell, England, 1978.

Wongwises Somchai and Kongkiatwanitch Wittaya Interfacial friction factor in vertical upward gas-liquid annular two-phase flow [Journal] // International Communications in Heat and Mass Transfer. - 2001. - 3 : Vol. 28. - pp. 323-336.

Wurtz Jorgen An Experimental and Theoretical Investigation of Annular Steam-Water Flow in Tubes and Annuli at 30 to 90 bar [Report]. - Denmark : Riso National Laboratory, 1978.

Zeigarnik Yuri Albertovich Annular flow [Online] // Thermopedia. - February 03, 2011. - March 21, 2021. - http://www.thermopedia.com/content/11/.

Zhao X [et al.] Validation and Benchmarking of CTF for Single- and Two-phase Flow Using VIPRE-01 [Conference] // International Topical Meeting on Nuclear Reactor Thermalhydraulics (NURETH-17). - Xi'an, China : [s.n.], 2017.

7 Appendix

7.1 Enthalpy imbalance factor

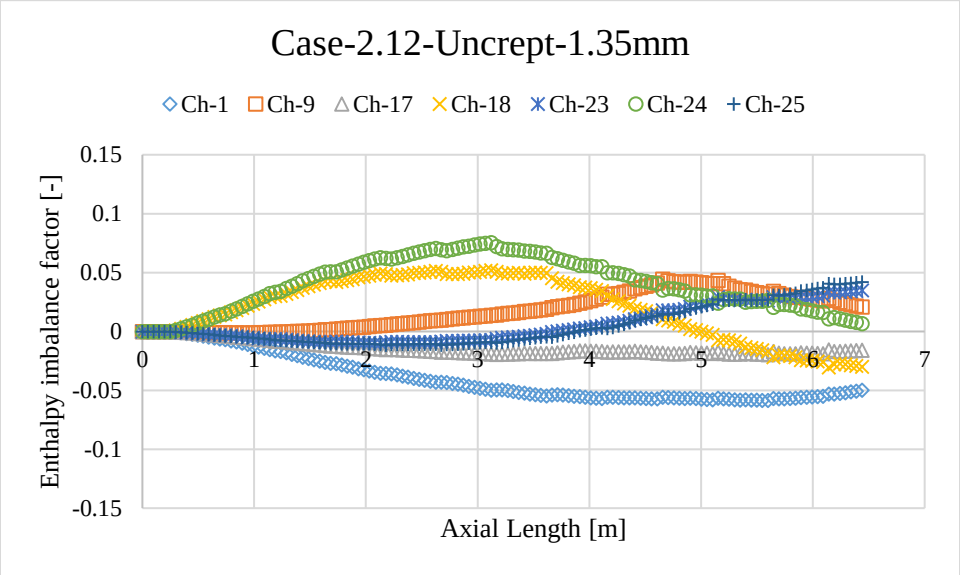

Figure 7-1 Enthalpy imbalance factor along axial length for uncrept case 2.12-Bearing pads 1.35 mm

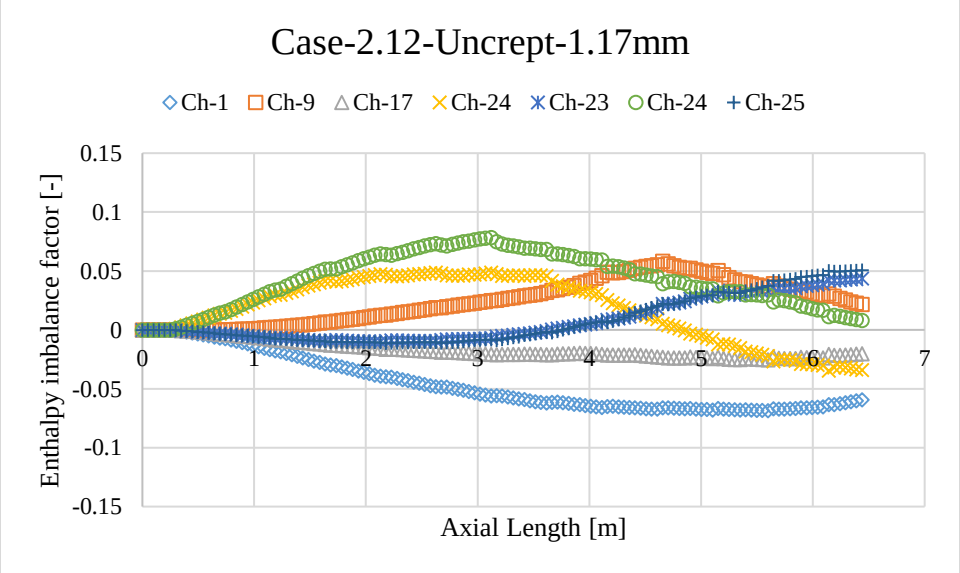

Figure 7-2 Enthalpy imbalance factor along axial length for uncrept case 2.12-Bearing pads 1.17mm

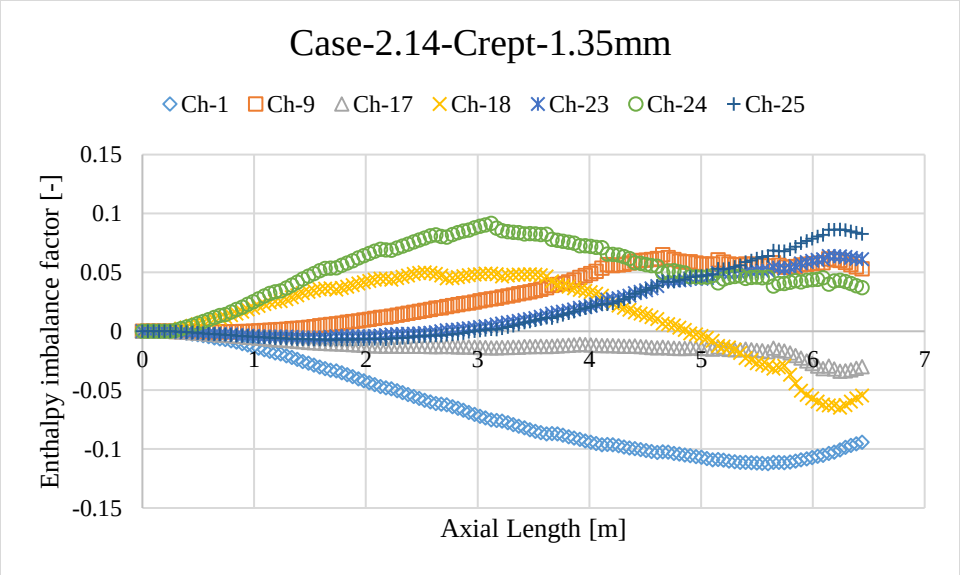

Figure 7-3 Enthalpy imbalance factor along axial length for crept case 2.14-Bearing pads 1.35mm

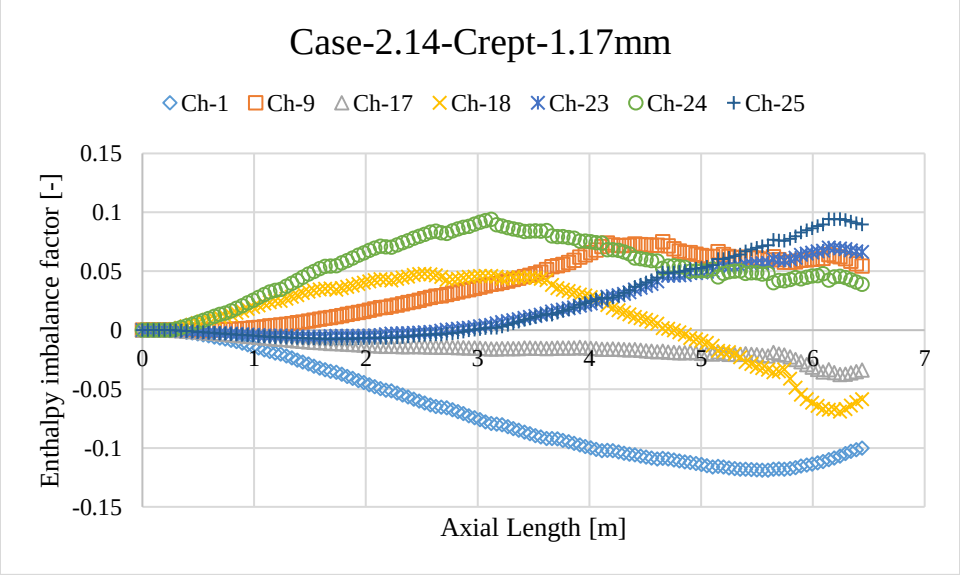

Figure 7-4 Enthalpy imbalance factor along axial length for crept case 2.14-Bearing pads 1.17mm

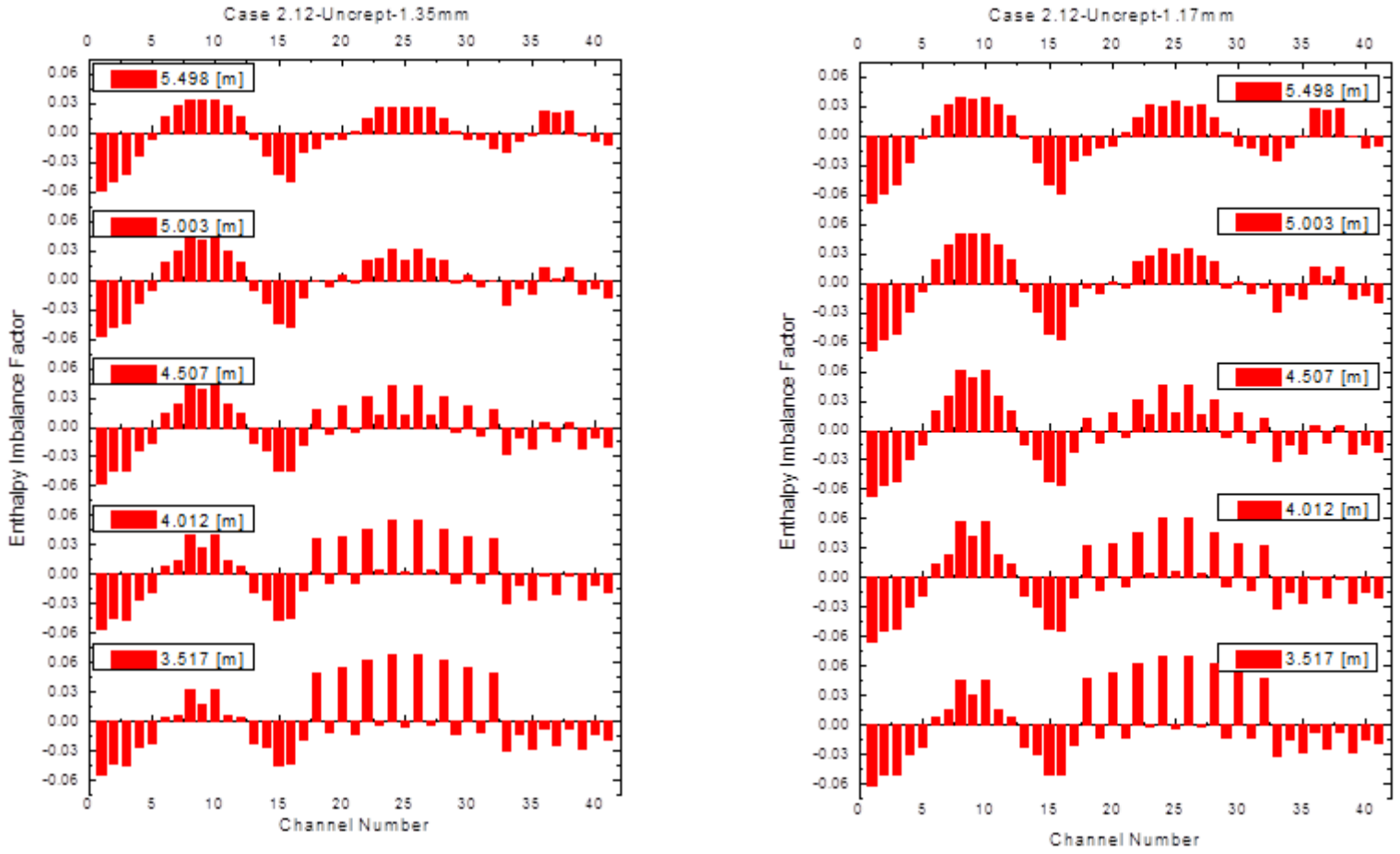

Figure 7-5 Enthalpy imbalance factors for different subchannels at various axial locations along the fuel channel with bearing pads 1.35 mm (Left plot) and 1.17 mm (Right plot)

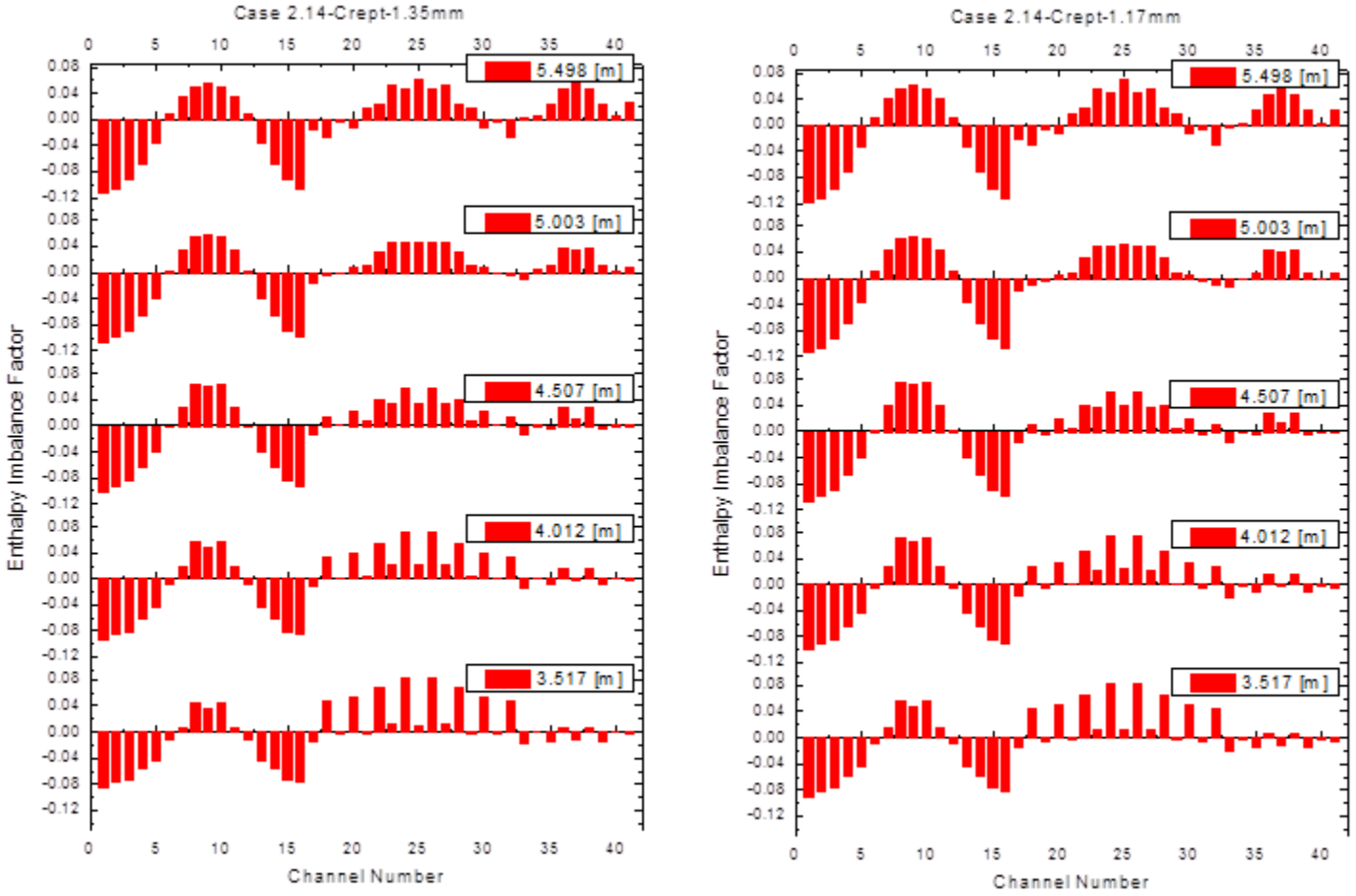

Figure 7-6 Enthalpy imbalance factors for different subchannels at various axial locations along the crept fuel channel with bearing ds 1.35 mm (Left plot) and 1.17 mm (Right plot)

7.2 Effect of turbulent mixing on BEIN

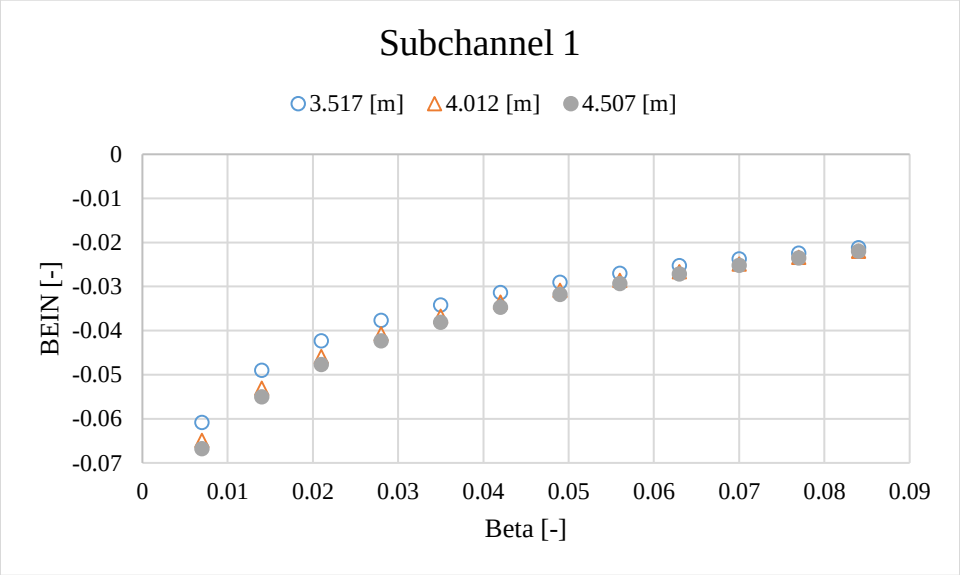

Figure 7-7 Effect of turbulent mixing on BEIN for uncrept case 2.12 [BP: 1.17 mm]

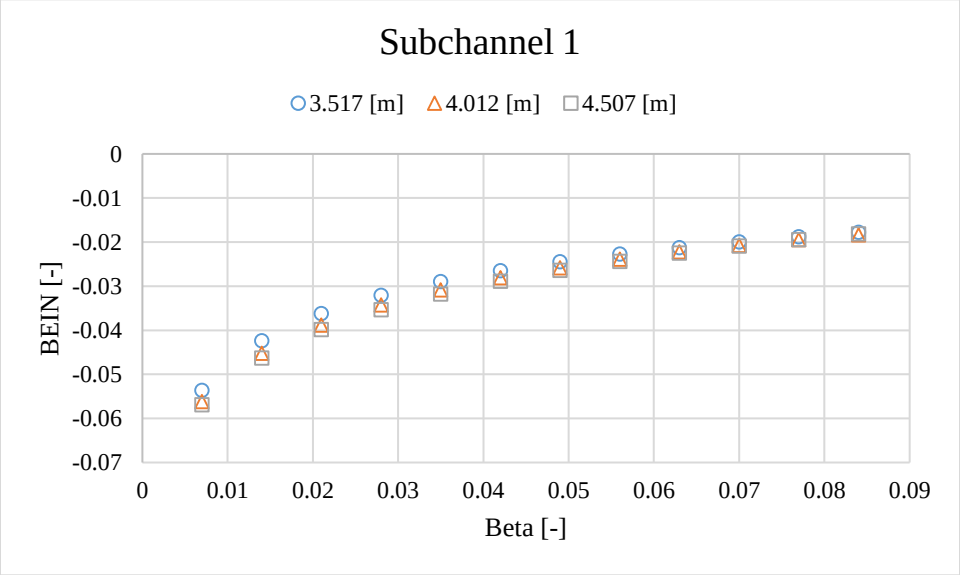

Figure 7-8 Effect of turbulent mixing on BEIN for uncrept case 2.12 [BP: 1.35 mm]

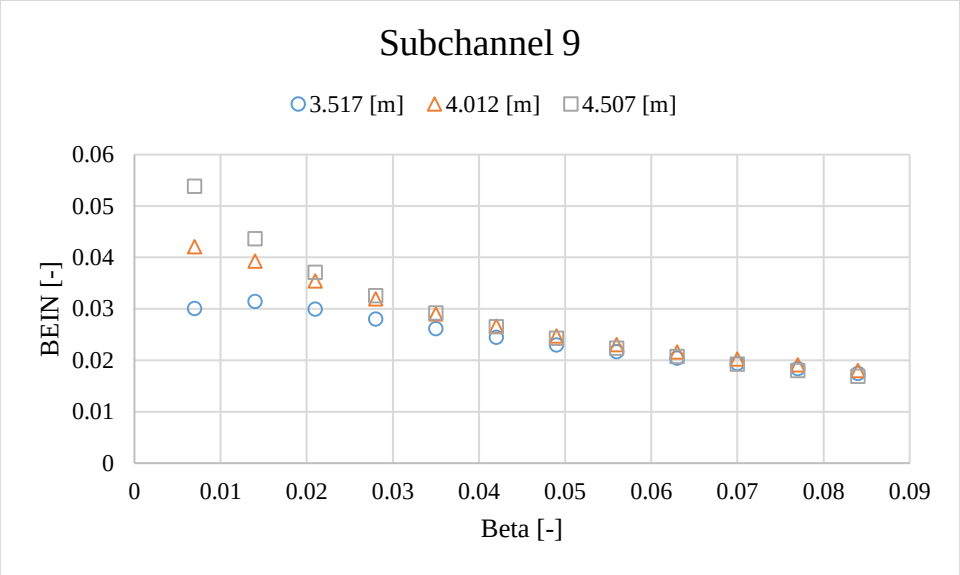

Figure 7-9 Effect of turbulent mixing on BEIN for uncrept case 2.12 [BP: 1.17 mm]

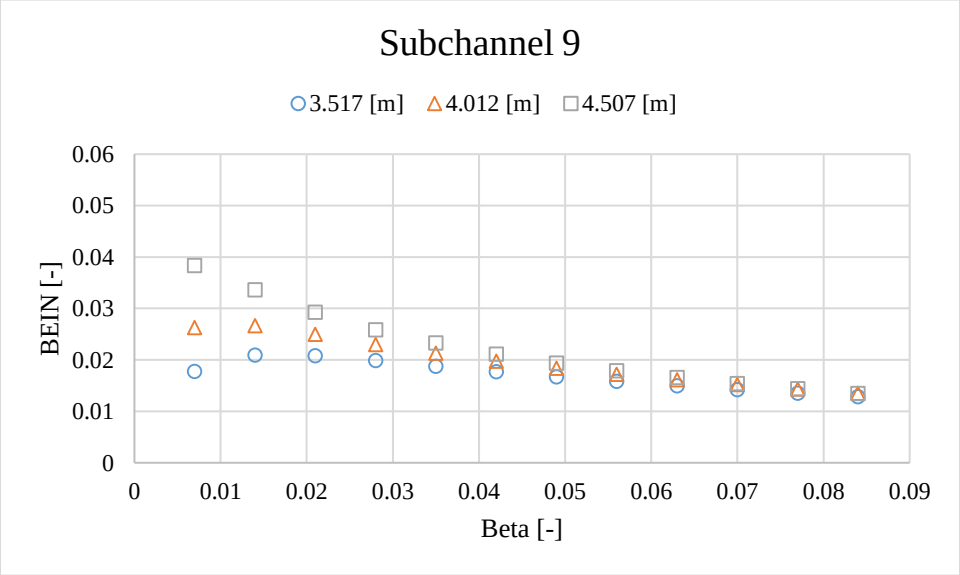

Figure 7-10 Effect of turbulent mixing on BEIN for uncrept case 2.12 [BP: 1.35 mm]

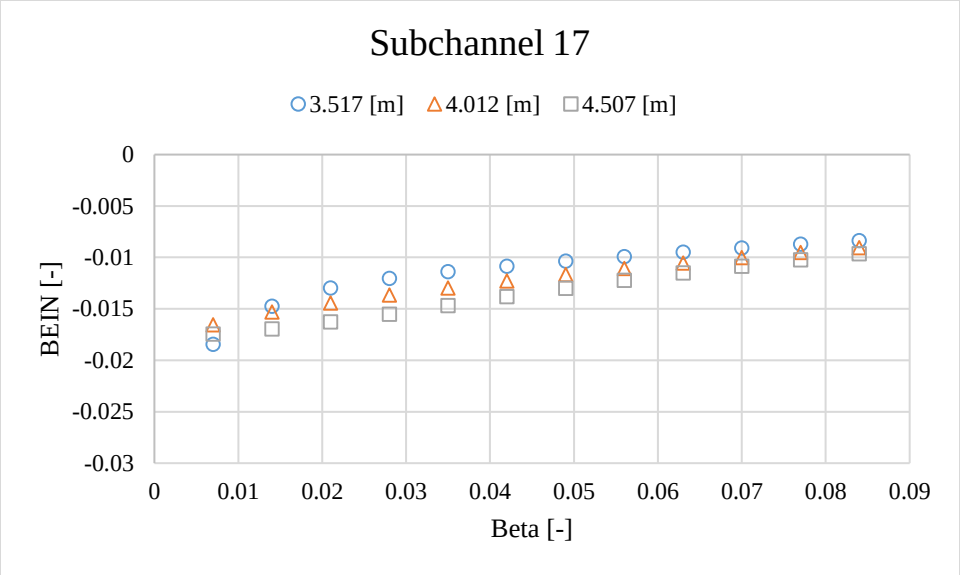

Figure 7-11 Effect of turbulent mixing on BEIN for uncrept case 2.12 [BP: 1.35 mm]

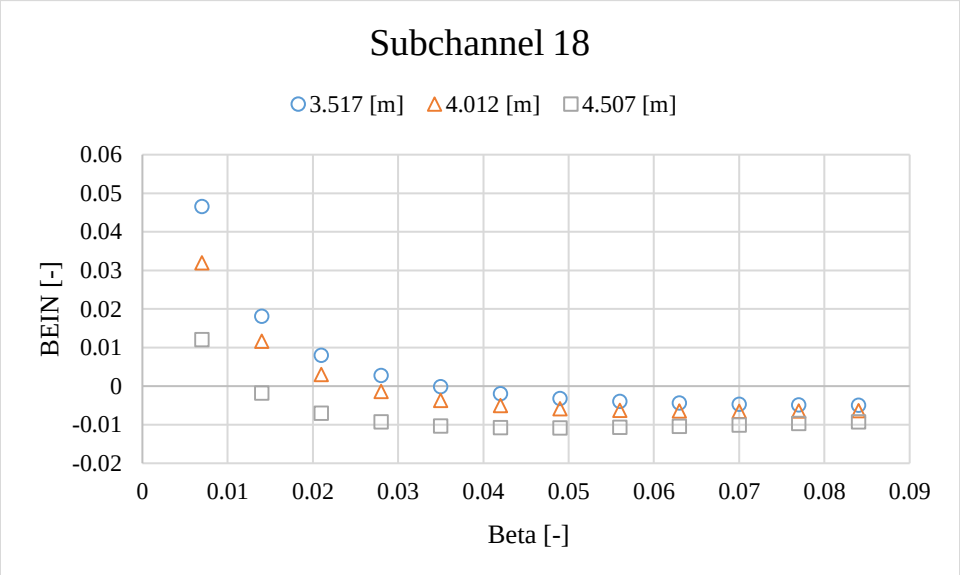

Figure 7-12 Effect of turbulent mixing on BEIN for uncrept case 2.12 [BP: 1.17 mm]

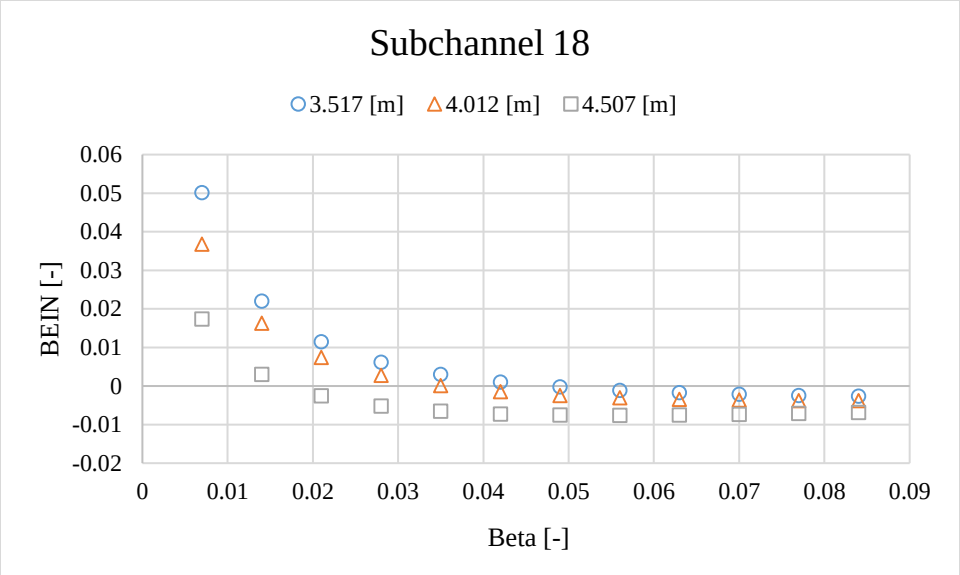

Figure 7-13 Effect of turbulent mixing on BEIN for uncrept case 2.12 [BP: 1.35 mm]

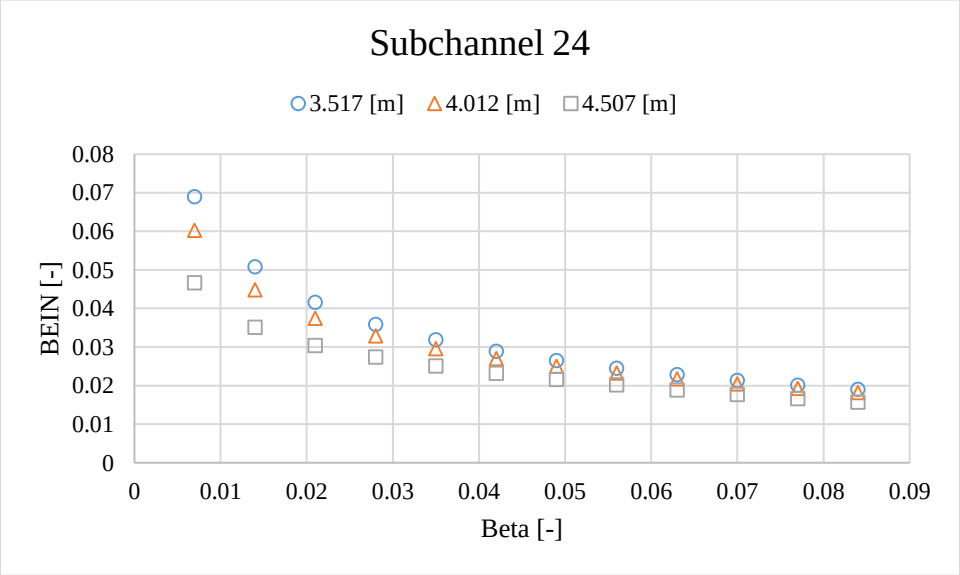

Figure 7-14 Effect of turbulent mixing on BEIN for uncrept case 2.12 [BP: 1.17 mm]

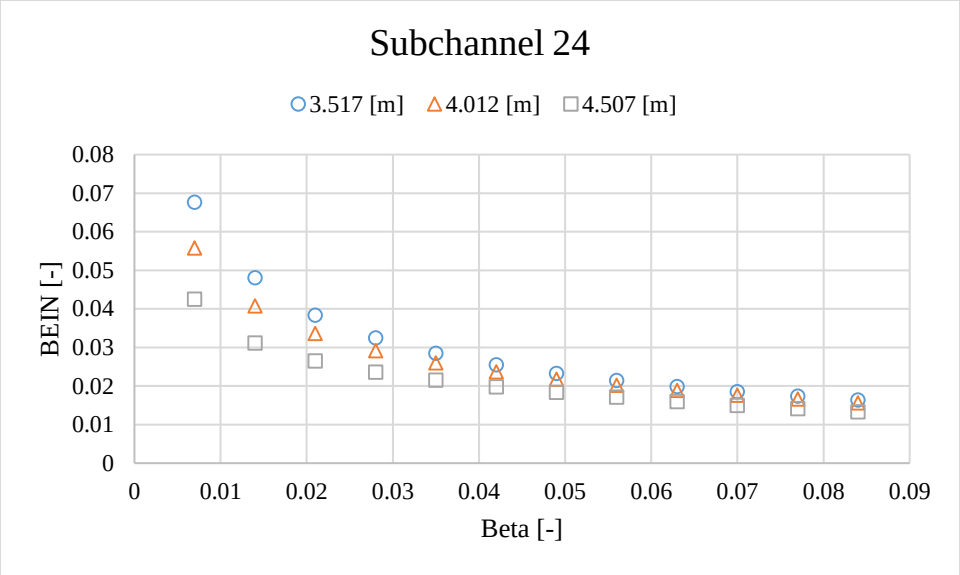

Figure 7-15 Effect of turbulent mixing on BEIN for uncrept case 2.12 [BP: 1.35 mm]

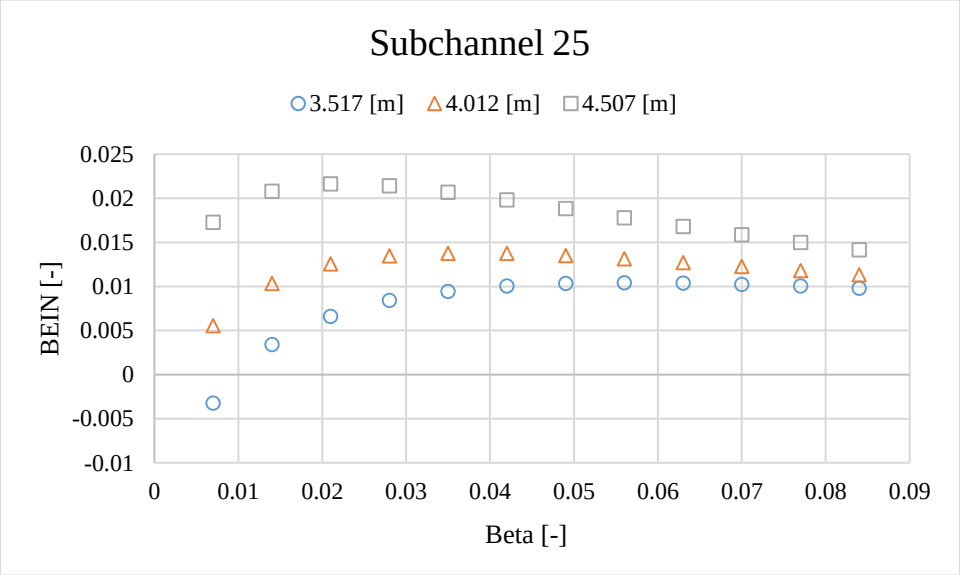

Figure 7-16 Effect of turbulent mixing on BEIN for uncrept case 2.12 [BP: 1.17 mm]

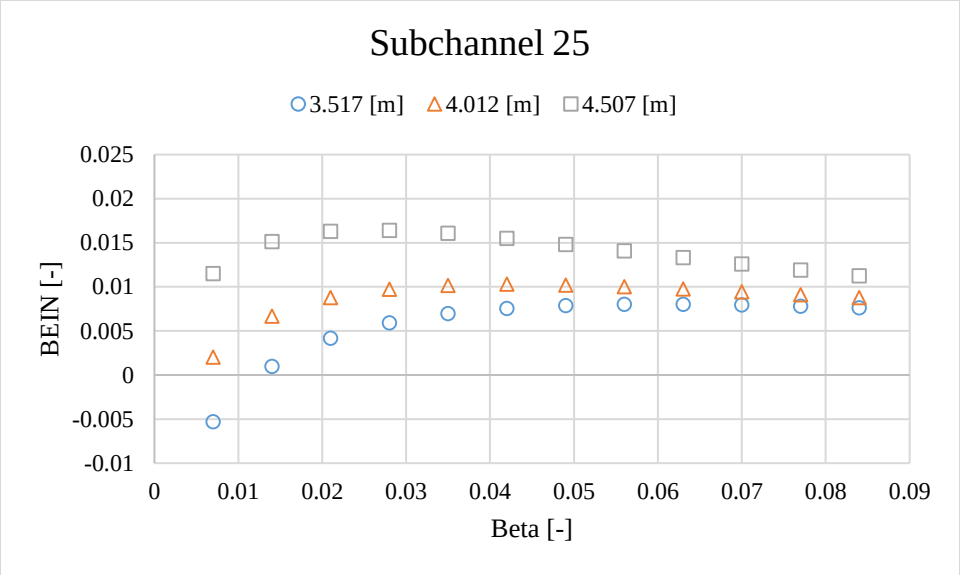

Figure 7-17 Effect of turbulent mixing on BEIN for uncrept case 2.12 [BP: 1.35 mm]

7.3 Effect of turbulent mixing on CHF

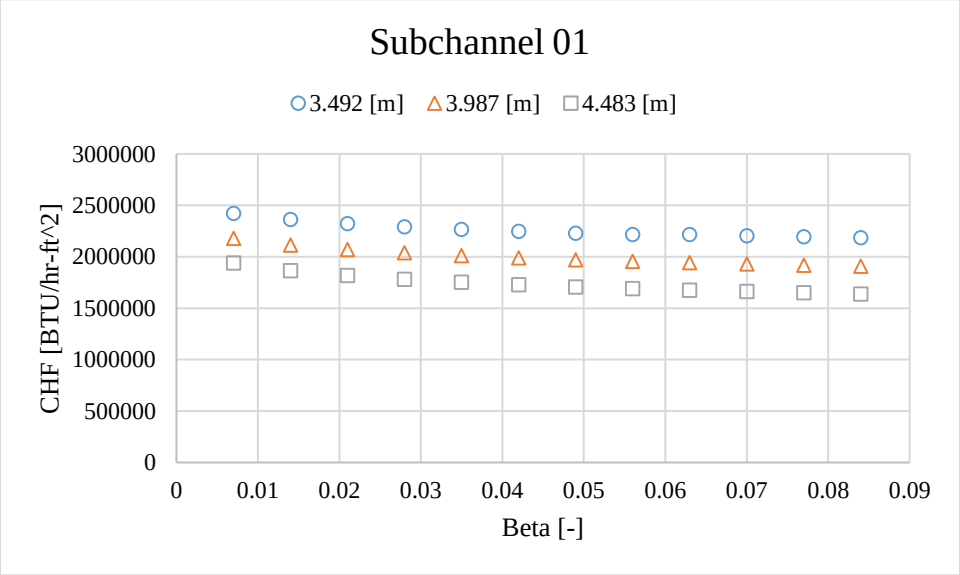

Figure 7-18 Effect of turbulent mixing on CHF for uncrept case-2.12 [BP: 1.17 mm]

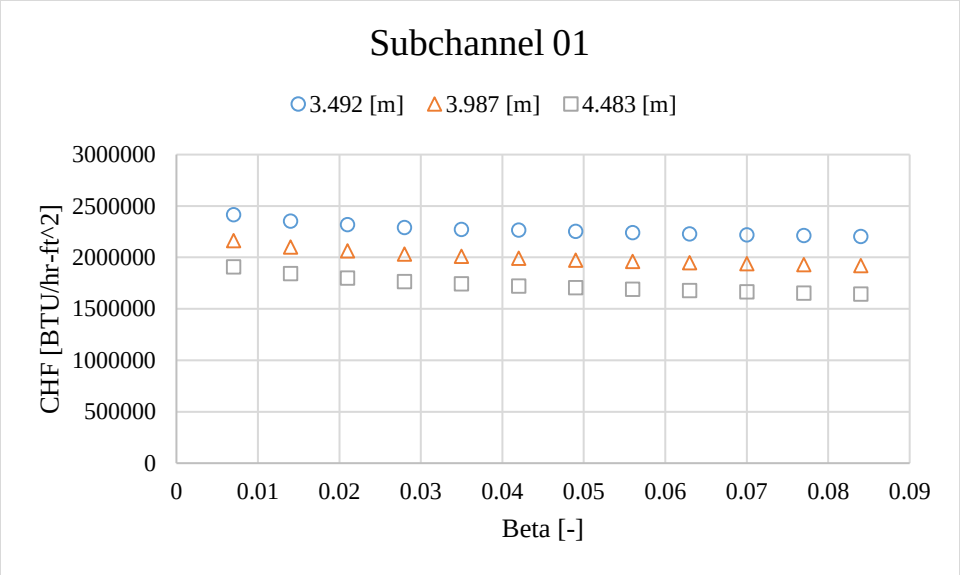

Figure 7-19 Effect of turbulent mixing on CHF for uncrept case-2.12 [BP: 1.35 mm]

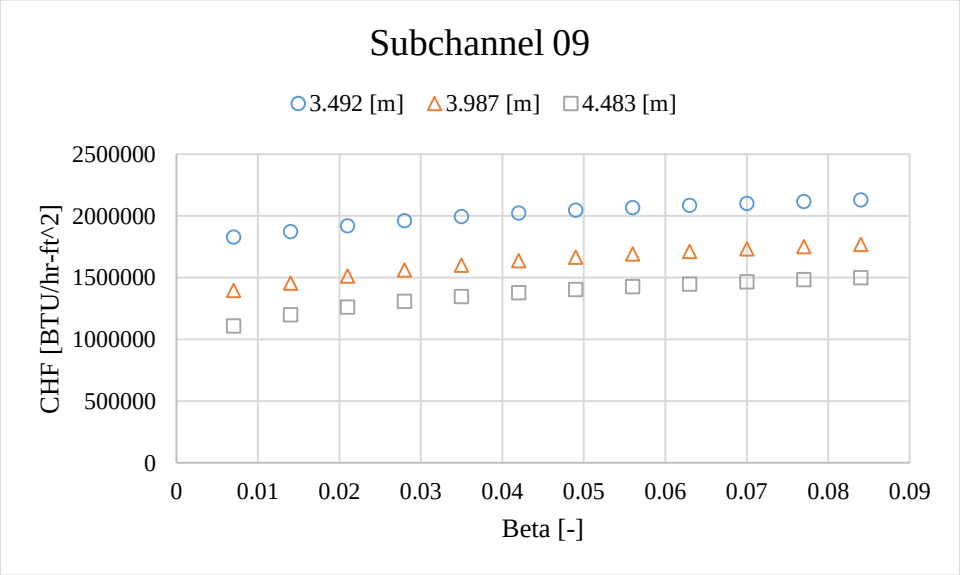

Figure 7-20 Effect of turbulent mixing on CHF for uncrept case-2.12 [BP: 1.17 mm]

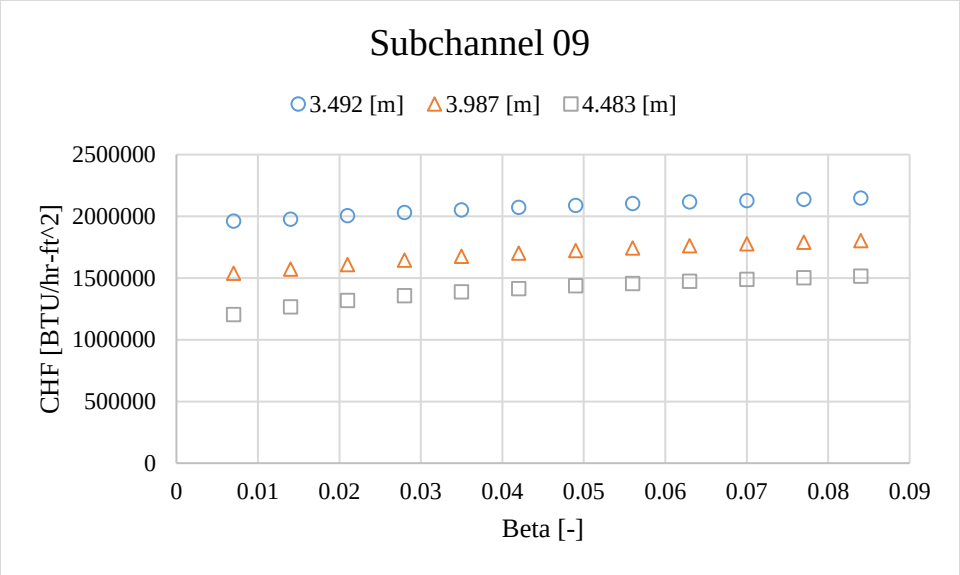

Figure 7-21 Effect of turbulent mixing on CHF for uncrept case-2.12 [BP: 1.35 mm]

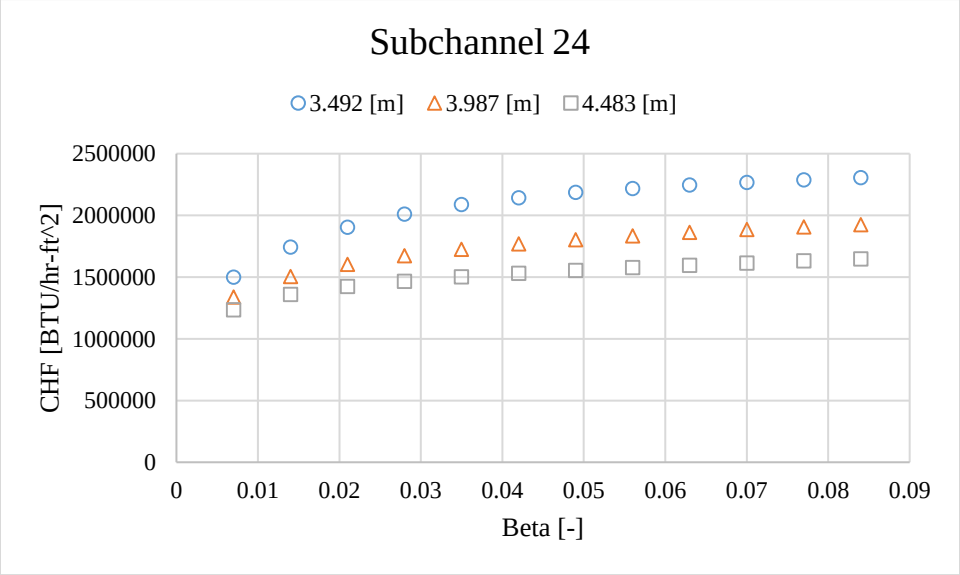

Figure 7-22 Effect of turbulent mixing on CHF for uncrept case-2.12 [BP: 1.17 mm]

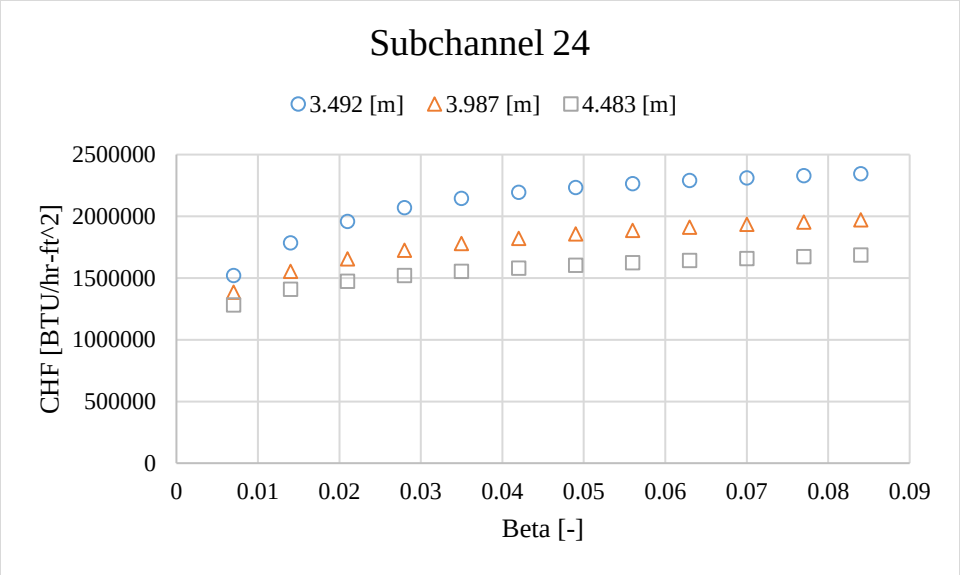

Figure 7-23 Effect of turbulent mixing on CHF for uncrept case-2.12 [BP: 1.35 mm]

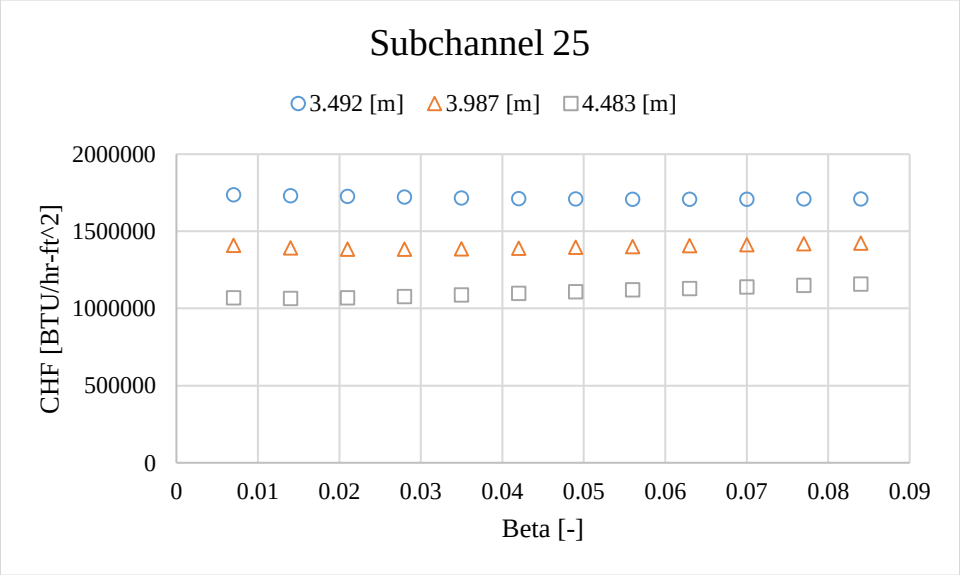

Figure 7-24 Effect of turbulent mixing on CHF for uncrept case-2.12 [BP: 1.17 mm]

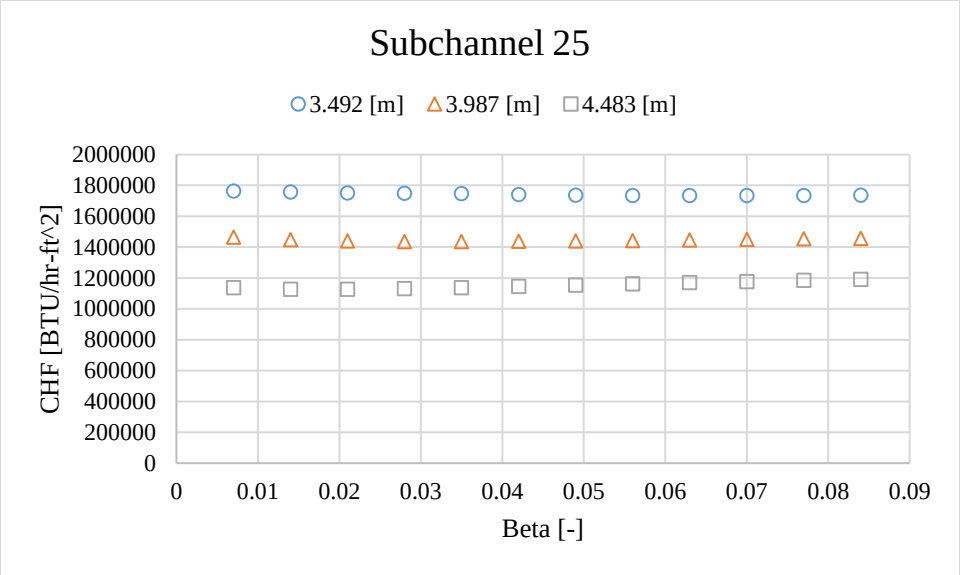

Figure 7-25 Effect of turbulent mixing on CHF for uncrept case-2.12 [BP: 1.35 mm]

7.4 Effect of turbulent mixing on DNBR

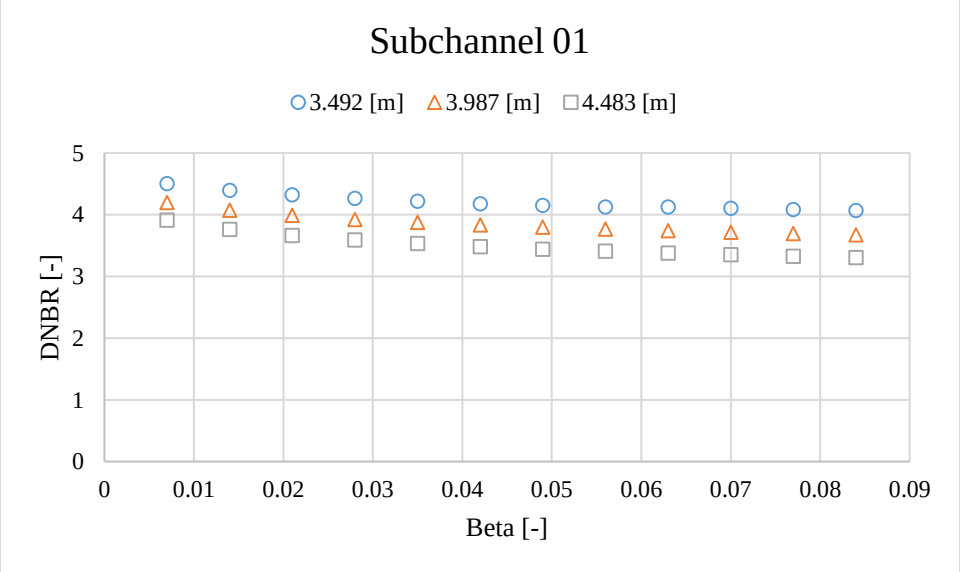

Figure 7-26 Effect of turbulent mixing on DNBR for uncrept case-2.12 [BP: 1.17 mm]

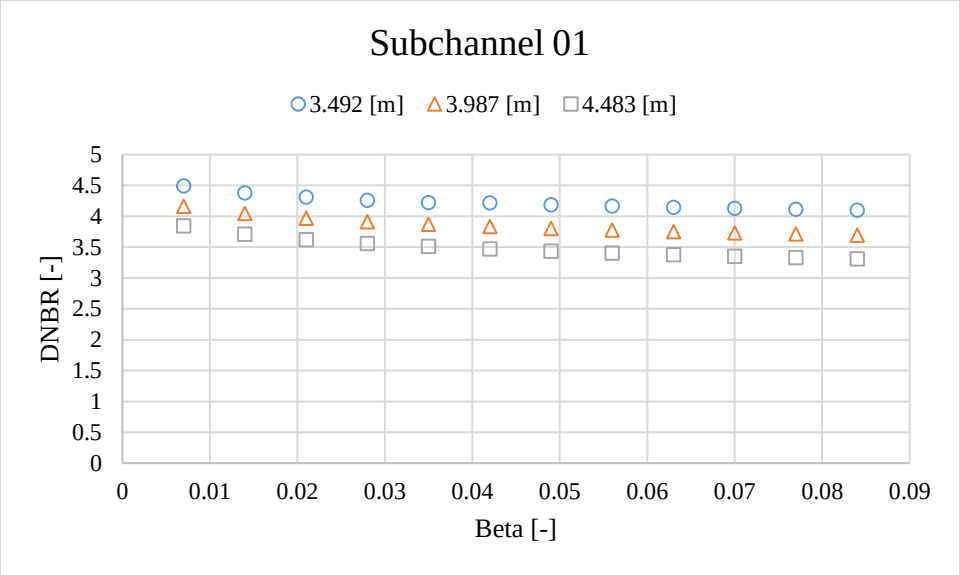

Figure 7-27 Effect of turbulent mixing on DNBR for uncrept case-2.12 [BP: 1.35 mm]

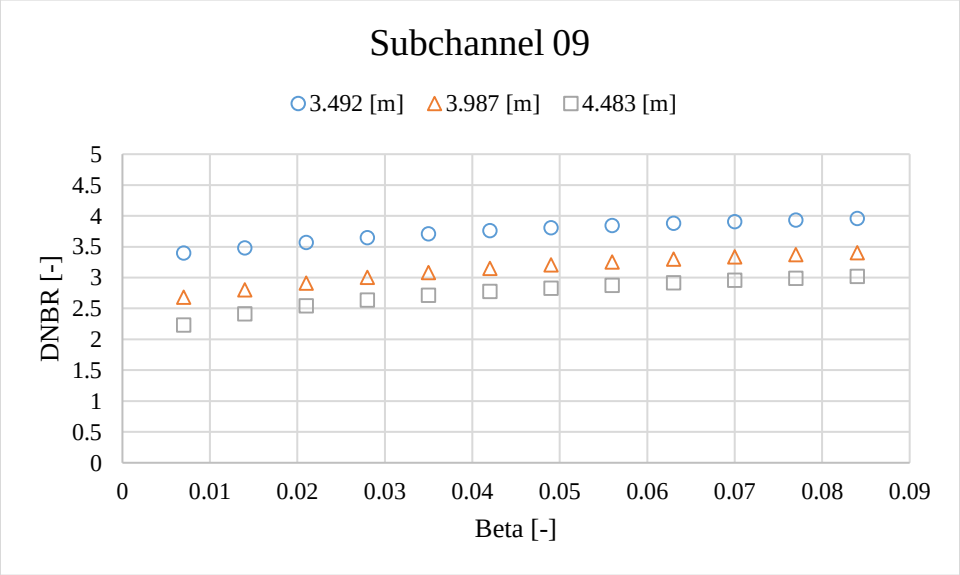

Figure 7-28 Effect of turbulent mixing on DNBR for uncrept case-2.12 [BP: 1.17 mm]

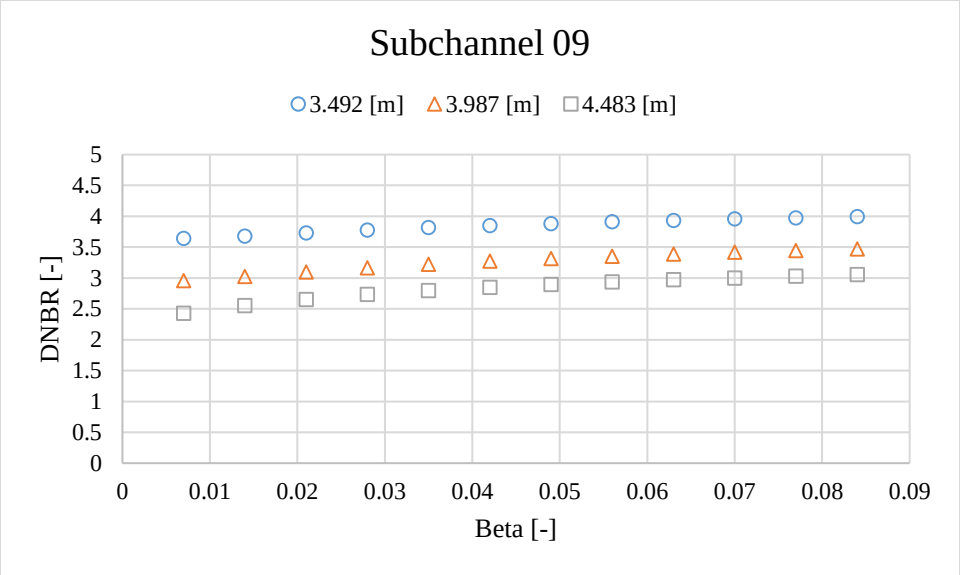

Figure 7-29 Effect of turbulent mixing on DNBR for uncrept case-2.12 [BP: 1.35 mm]

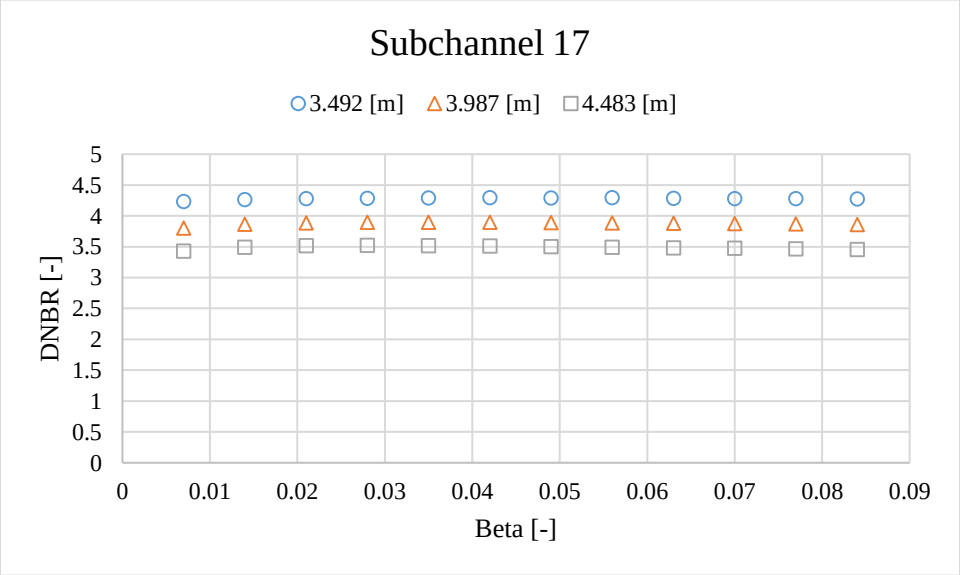

Figure 7-30 Effect of turbulent mixing on DNBR for uncrept case-2.12 [BP: 1.17 mm]

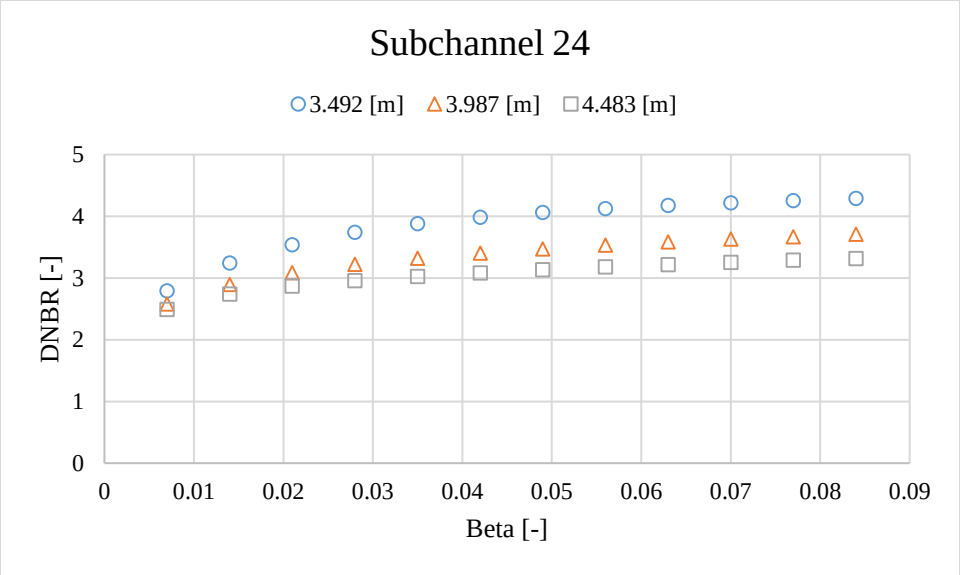

Figure 7-31 Effect of turbulent mixing on DNBR for uncrept case-2.12 [BP: 1.17 mm]

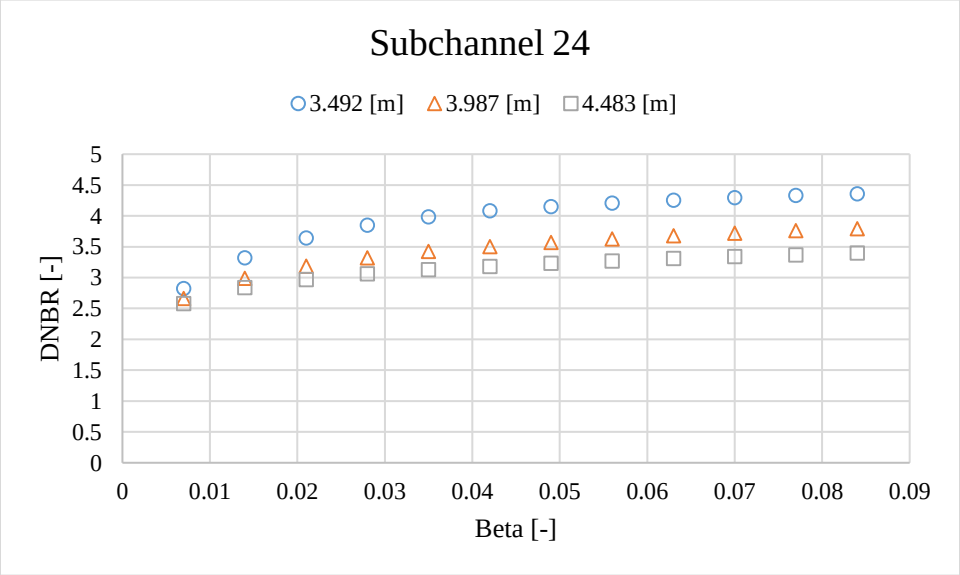

Figure 7-32 Effect of turbulent mixing on DNBR for uncrept case-2.12 [BP: 1.35 mm]

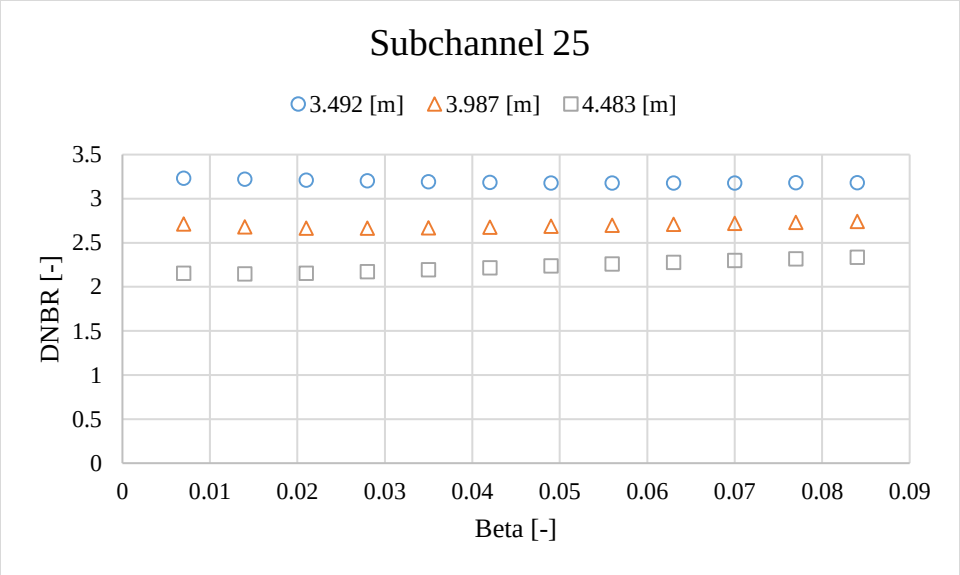

Figure 7-33 Effect of turbulent mixing on DNBR for uncrept case-2.12 [BP: 1.17 mm]

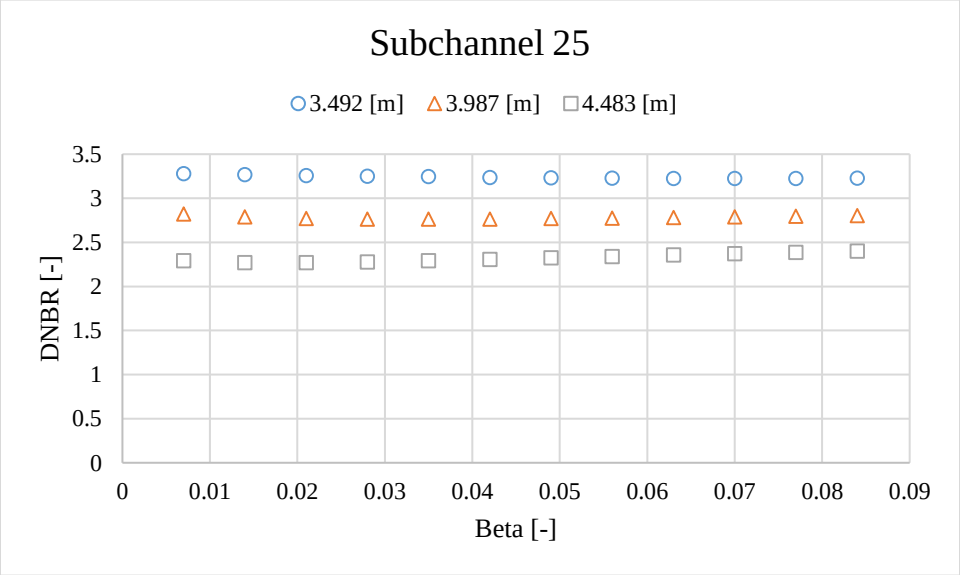

Figure 7-34 Effect of turbulent mixing on DNBR for uncrept case-2.12 [BP: 1.35 mm]

7.5 Effect of turbulent mixing in GE 3 X 3 experiment

(Lahey Jr., et al., 1970) performed two-phase flow and heat transfer experiments in nine-rod bundle for diabatic and adiabatic conditions. The experiment is modeled in CTF to analyze the effect of turbulent mixing on subchannel quality and mass flow rate for three subchannels (Corner, side and center). Figure 7-35 and Figure 7-36 shows the exit quality for corner, side and center subchannels. The results shows that at higher 'BETA' values (~ >0.035) there is insignificant change in exit quality. Furthermore, the exit quality for corner subchannel is significantly overpredicted. Figure 7-37 and Figure 7-38 presents corner, side and center subchannel's exit mass flow rates. Table 7-1 gives the experimental test conditions for the two cases modeled in CTF.

Table 7-1 Experimental test conditions for GE 3X3 experiment *(Lahey Jr., et al., 1970)*

Case	Power [kW]	Inlet sub cooling [kJ/kg]	Inlet Mass flow rate [kg/sec]	Exit quality [%]			Exit Mass flow rate [kg/sec]		
				Corner	Side	Center	Corner	Side	Center
2B2	532	238.67	1.35873	0.3	1.5	3.0	0.02548	0.08314	0.13677
2D1	1064	602.9	1.38437	8.3	10.5	11.7	0.02911	0.08936	0.14082

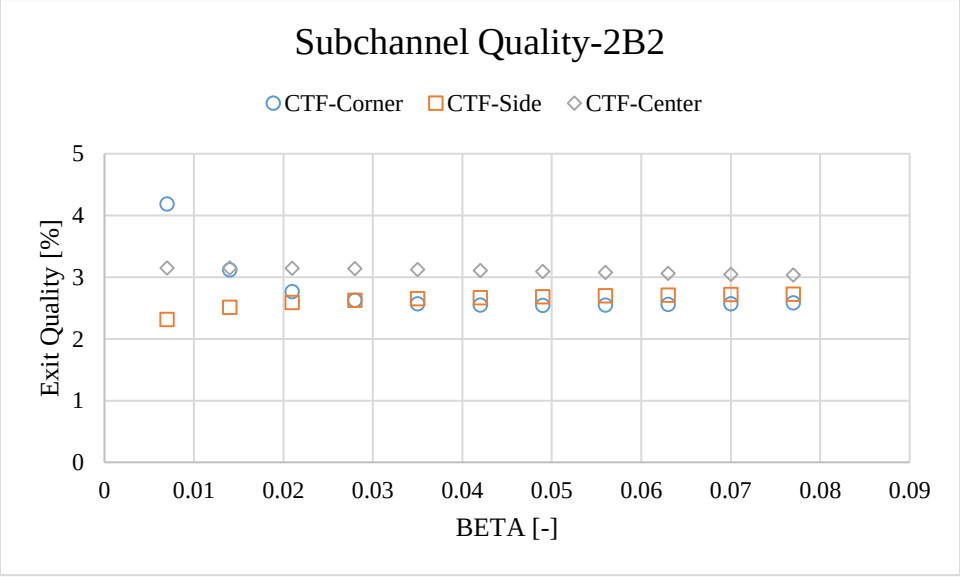

Figure 7-35 Effect of turbulent mixing on corner, side and center subchannel exit quality

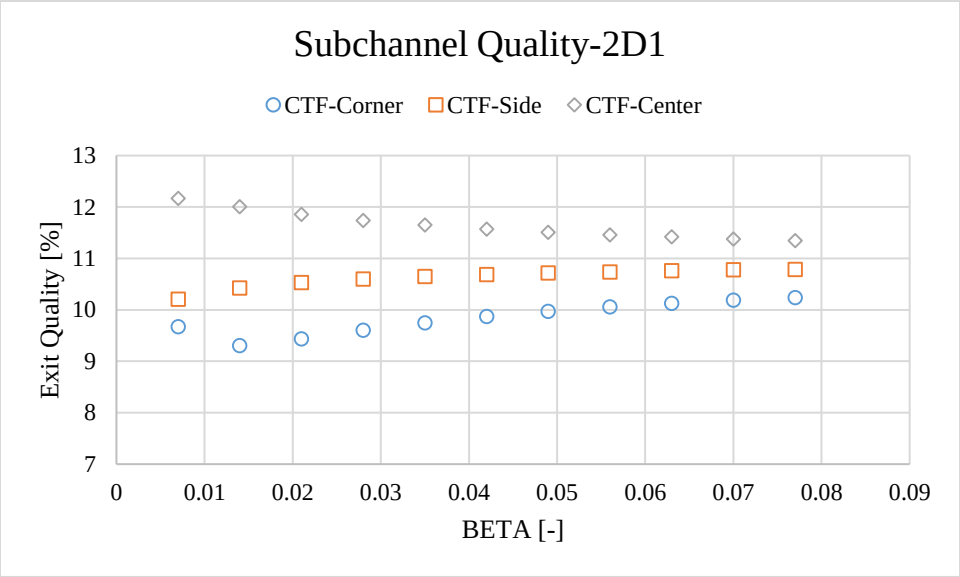

Figure 7-36 Effect of turbulent mixing on corner, side and center subchannel exit quality

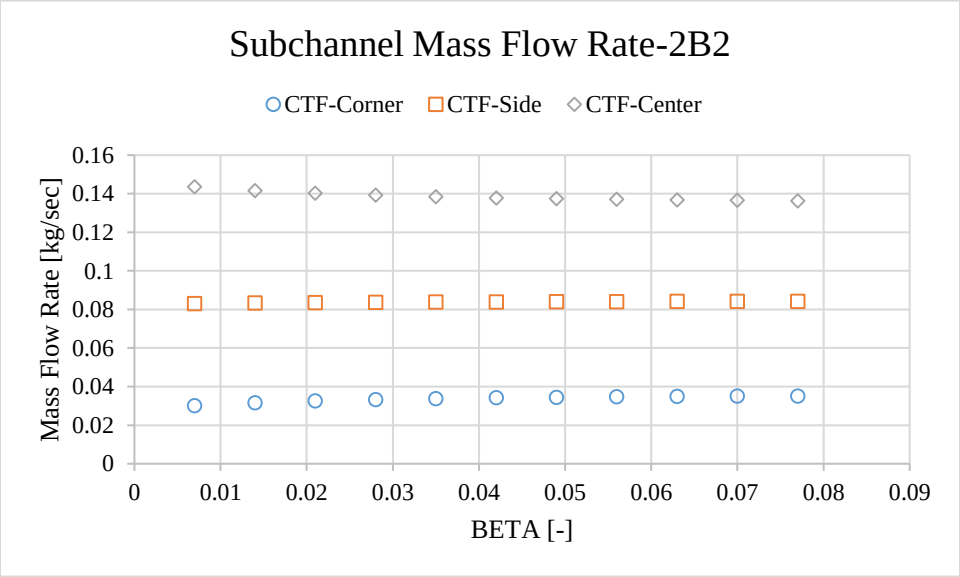

Figure 7-37 Effect of turbulent mixing on corner, side and center subchannel mass flow rate

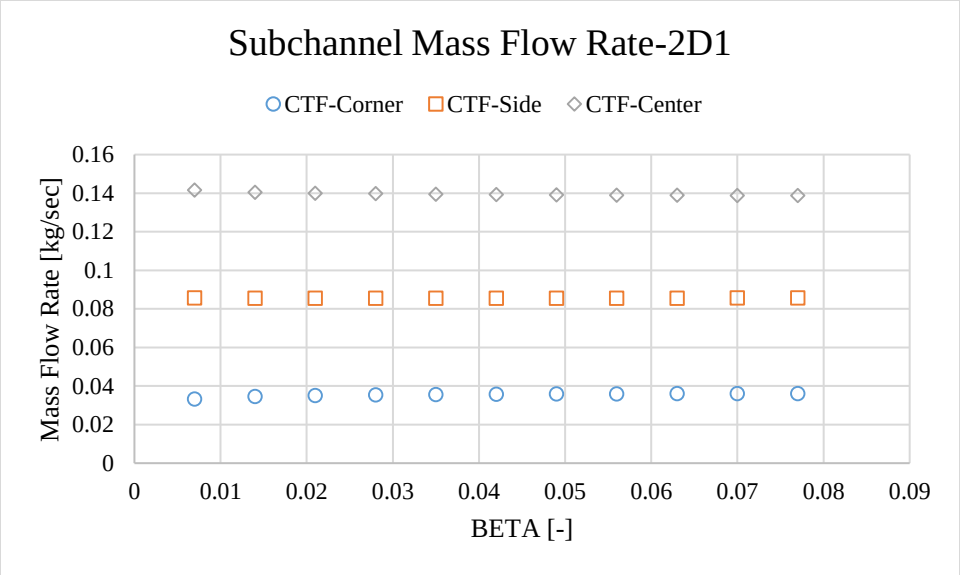

Figure 7-38 Effect of turbulent mixing on corner, side and center subchannel mass flow rate

7.6 Incorporation and testing of R-134a fluid properties in CTF

Incorporation and Testing of R-134a Modeling Capabilities in the CTF Code

U. Shahid[1], Y. Liu[1, 2], A. Abarca[3], D. R. Novog[1]

[1]Department of Engineering Physics, McMaster University, Canada

[2]School of Nuclear Science and Technology, Xi'an Jiaotong University, China

[3]Department of Nuclear Engineering, North Carolina State University, USA

Abstract

Subchannel analysis codes are an important tool for analysis of fuel cooling during transients, optimization of fuel designs, and investigation of complex Multiphysics phenomenon such as Crud Induced Power Shift (CIPS). While there exists some experimental data under full-scale reactor conditions, there is a wealth of additional separate-effect experimental data available for validations and benchmarking in alternative fluids. In particular experimental data on CHF (Pioro, et al., 2001), interfacial phenomenon (Quiben, et al., 2007) and pressure drop (Leung, et al., 1999) are available in R-134a and can provide meaningful data for model development and validation. This study focuses on the incorporation of R-134a fluid properties into the subchannel code CTF which is distributed by North Carolina State University. This capability will broaden the testing and benchmarking opportunities for CTF. For the current study, fluid properties and refrigerant specific correlation have been implemented in CTF, along with CHF correlation by (Katto, et al., 1984). Furthermore, CHF prediction using the water LUT (Groeneveld, et al., 2007) which was available in CTF previously has been performed using fluid-to-fluid scaling for prediction of R-134a CHF data. Finally, the experimental and code predicted CHF are compared to four different R134a CHF experiments.

Key words: CTF; R-134a; CHF correlations; LUT; Transient simulation

1 Background

Subchannels are defined as the coolant flow areas inside a fuel assembly, bounded by fuel rods and imaginary lines linking adjacent rod centers (Carver, et al., 1995). Subchannels codes are useful in predicting the local thermal hydraulic parameters such as pressure, mass flow rates, enthalpy etc. in subchannels. Moreover, local subchannel parameters like pressure, mass flow rate, and quality, play a vital role in critical heat flux

(CHF) determination as well as other processes such as crud induced power shift (CIPS) phenomena. The prediction of CHF is important in the assessment of operational transients and design basis accidents while CIPS is a Multiphysics phenomenon that requires detailed subchannel thermal hydraulic predictions (Salko, et al., 2018). While fuel design specific correlations are developed by fuel vendors and used in one-dimensional system codes for safety analysis, subchannel analysis benefits from local CHF predictions in subchannel based on generic tube CHF phenomena. Many subchannel codes like CTF, ASSERT, VIPRE, ATHAS, FLICA etc. have been developed for PWR, BWR and CANDU type reactor subchannel analysis. Among them CTF has been adopted in the US Department of Energy CASL program and provides a robust two-fluid approach for subchannel analysis. The COBRA subchannel code was originally developed by Pacific Northwest Laboratories in 1980 for thermal-hydraulic analysis of nuclear power reactors. Over the last four decades it has evolved and eventually been re-named into the CTF subchannel code. CTF solves conservation equations for mass, momentum, and energy for three coolant fields; liquid, entrained droplets, and vapor using the Semi-Implicit Method for Pressure-Linked Equations (SIMPLE) technique (Salko, et al., 2019).

Over the years many CHF, interfacial measurements and two phase flow experiments have been performed using various refrigerants but most recently the major experimental campaigns using refrigerant R-134a. Refrigerants can be used in experiments at lower pressures and much lower test section powers than water experiments while still maintaining similarity in dimensionless parameters (e.g., density ratio and/or non-dimensional heat flux). The main reasons behind these refrigerant experiments are; 1) Economics; performing experiments with water typically require much higher pressures, power requirements and temperatures leading to higher experimental costs, 2) Visualization; Refrigerants are operated at lower temperature and pressures and it is more feasible to deploy flow visualization techniques than it would be using higher pressure water, 3) Ecological; R-134a is environmentally more acceptable than many other Refrigerants or Freons. Currently CTF version 4.0 supports only water as a working fluid. Hence the incorporation of R-134a will broaden the testing and benchmarking capabilities of CTF with R-134a experimental databases.

2 Introduction

As stated previously, R134a is often used to perform scaled thermal-hydraulic experiments. For example, in order to conduct relevant experiments, in PWR condition in water requires a pressure of 16 MPa and typical electrical powers on the order of Mega-Watts (depending on if it is pin experiments or full bundles). Using scaling analysis such as those proposed by Ahmed (Ahmad, 1972), experiments with similar non-dimensional parameters can be performed at pressure from 2-4 MPa and with power $1/10^{th}$ of that required for water. As a result there are experiments performed in many laboratories around the world measuring thermal-hydraulic phenomena in refrigerants. While there is a wealth of this data in literature, its use in benchmarking, model development, and validation has been limited because many codes do not have the capability to directly model these refrigerants. In order to improve this situation, codes should be modified to a) have the appropriate refrigerant properties and b) provide options for correlations that are fluid specific for Freon or are non-dimensional (E.g., CHF correlation). Recently, (Son, et al., 2016) study focused on implementation and verification of R-134a in MARS code. In that work, single channel flow boiling experiments of R-134a were simulated and the heat transfer coefficient (HTC) was compared with the predicted HTC by MARS code.

CHF correlations have been developed from experimental and analytical studies for different working fluids. The most common methodologies used for predicting CHF are Heat Balance Method (HBM) and Direct Substitution Method (DSM). The CHF predicted at a location by using HBM depends on upstream conditions such as distance from test section's inlet and inlet sub cooling. Whereas CHF predicted by DSM depends on local parameters such as local quality, which is not the case for short tubes (Shah, 1987).

For HBM correlation, this paper utilizes the CHF is predicted using Katto's correlation. Katto (Katto, et al., 1984) performed CHF experiments for a round tube while covering both DNB and annular film dry-out regimes in uniformly heated tubes. Katto's correlation is divided in two parts based on a density ratio of 0.15. It is widely used because of its range of applicability and its suitability for both refrigerants and water.

For DSM correlation, the CHF look up tables (LUT) are accepted and widely used for CHF predictions because they avoid correlation

form issues and utilize data directly in the predictions.

The 2006 CHF LUT has a wide range of applicability covering ranges of 0.1 – 21 MPa, 0 – 8000 kg/m^{2}s, and -0.5 – 1 for pressure, mass flux and quality respectively. LUT predicts CHF using local parameters such as pressure, mass flux and quality. The data points obtain for LUT were for 8 mm diameter tubes and correction factor are available for alternate geometries.

For this study the CHF comparison was performed with four different CHF experimental databases. Table2-1 shows the experimental test conditions for the four CHF experiments.

Firstly, (Liu, et al., 2021) performed R-134a CHF experiments in a square duct with a uniformly heated rod in the middle of the duct. One mixing vane spacer was introduced in the test section, at ~0.82 m from inlet, to take into account spacer effect on CHF. The parameter ranges selected for different test cases were similar to the typical modeling range of PWR experiments. These experiments were performed to obtain the relationship between CHF and local parameters and their effect on CHF.

Secondly, (Kim, et al., 2005) performed CHF experiments in smooth and rifled uniformly heated tubes. These experiments were performed to investigate the CHF characteristics comparison of rifled tube and smooth tube. Only the 40 datasets from smooth tube experimental database were used for current study analysis.

Thirdly, (Chun, et al., 2007) performed CHF experiments in tubular and annular geometry using R-134a. The comparison was done between R-134a and water CHF data by using Ahmad and Katto modeling parameters. In this work, only the 32 tube-based test cases are included.

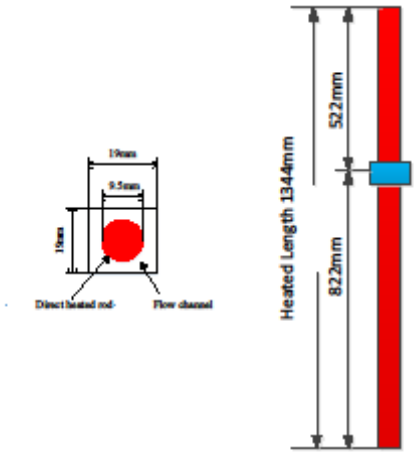

Figure 2-1 Cross-sectional (left Fig.) and axial (right Fig.) view of *(Liu, et al., 2021)* test section

Finally, (Pioro, et al., 2001) performed experiments in R-134a cooled tubes for various heated lengths and hydraulic

diameters to provide a consistent set of CHF database. For this study, 20 cases corresponding to three different heated lengths were selected.

The focus of current study is to incorporate R-134a fluid properties in subchannel code CTF and to compare its CHF predictions using HBM and DSM methods with all four experimental databases. For the current study the CHF was predicted using; Katto's HBM correlation and the CHF LUT local conditions predictions were used. Fluid-to-fluid scaling technique was implemented in CTF for obtaining R-134a specific CHF predictions from LUT as explained below.

Table 2-1 Experimental test conditions for four selected experimental database

Experiment	Cases	Geometry	Hydraulic Diameter [mm]	Mass flux [kg/m^2-sec]	Pressure [MPa]	Inlet Sub-cooling [kJ/kg]
(Liu, et al., 2021)	28	Annular	10.97	870 – 2105	1.83 – 2.78	17.66 – 95.81
(Kim, et al., 2005)	40	Tubular	17.04	285 – 1300	1.3 – 2.39	13.24 – 65.18
(Chun, et al., 2007)	34	Tubular	7.5, 9.4	710 – 3500	1.43 – 2.9	44.4 – 57
(Pioro, et al., 2001)	20	Tubular	6.92	500	1.67	-32.12 – 68.21

3 Methods

The methods are sub-divided into three sections representing the implementation of R-134a properties in CTF, fluid-to-fluid scaling, and CHF comparisons.

3.1 R-134a incorporation in CTF

In CTF, fluid properties are divided into three regimes: saturated liquid/vapor mixture, sub-cooled liquid, and super-heated vapor properties. All the R-134a properties for this work were obtained from the NIST R-134a database (U.S Department of Commerce, 2021). Firstly, saturated liquid and vapor property tables were obtained at various saturation pressures. The selected range of saturation pressure was between 0.634 – 3.627 MPa which covers a sufficient R-134a

property range for CHF experiments relevant to scaled PWR and BWR conditions. The properties included vapor enthalpy, liquid enthalpy, surface tension, temperature, pressure, liquid thermal conductivity, vapor thermal conductivity, liquid specific heat capacity, vapor specific heat capacity, liquid density, vapor density, liquid dynamic viscosity and vapor dynamic viscosity. CTF routines are used to interpolate the local properties based on local conditions based on the input property tables.

CTF also requires several derivatives of these fluid properties with respect to the pressure and enthalpy of the fluid. To provide these derivatives in a computationally efficient manner, the state coefficients for liquid specific volume, vapor specific volume, liquid enthalpy, and vapor enthalpy were extracted from the literature. The R-134a state coefficients were used to calculate the derivative of density w.r.t pressure, and derivative of density w.r.t enthalpy for both phases (liquid and vapor) and included in the code routines. A large data bank from NIST was chosen to update the Eq. 1 - 4 coefficients using least square method. The equations for liquid specific volume, vapor specific volume, liquid enthalpy, and vapor enthalpy are as follows;

$$v_l = exp\left[\sum_{i=1}^{5}\left(\sum_{j=1}^{3} C_{CXij} P^{j-1}\right) H_l^{i-1}\right] \quad (1)$$

$$v_g = V_c(1) + V_c(2) * P + \frac{V_c(3)}{P} + V_c(4) * H_g + V_c(5) * H_g * P + V_c(6) * \frac{H_g}{P} \quad (2)$$

$$H_f(P_{sat}) = \sum_{n=1}^{9} A_n [ln(P_{sat})]^{n-1} \quad (3)$$

$$H_g(P_{sat}) = \sum_{n=1}^{9} B_n [ln(P_{sat})]^{n-1} \quad (4)$$

Finally, property correlations were developed using least square method for six superheated properties; thermal conductivity, dynamic viscosity, specific heat capacity, enthalpy, density and temperature, and replaced the existing water formulations in CTF.

An extensive series of verification tests were performed to cross-check the fluid properties over the range of CTF applications against the NIST database in order to verify the correct implementation of the fluid property routines.

3.2 Fluid-to-fluid modeling approach

Fluid-to-fluid modeling is used in thermal hydraulic analysis and design of nuclear power reactors to transform correlations or

experimental data from one fluid to another by attempting to assure similarity in the important non-dimensional groups. While it may not be possible to match all non-dimensional groupings, fluid-to-fluid scaling such as that proposed by (Ahmad, 1972) is used extensively in thermal-hydraulic research. In most of the literature the scaling of thermal-hydraulic parameters in Table 3-1 are widely accepted.

Table 3-1 Fluid-to-fluid modeling scaling parameters and their respective correlation *(Katto, 1978)*

Scaling Parameters Similarity	**Correlation**
Density	$\left(\frac{\rho_f}{\rho_g}\right)_M \Big/ \left(\frac{\rho_f}{\rho_g}\right)_P = 1$
Mass flux	$\left(\frac{G\sqrt{D}}{\sqrt{\rho_f.\sigma}}\right)_M \Big/ \left(\frac{G\sqrt{D}}{\sqrt{\rho_f.\sigma}}\right)_P = 1$
Steam quality	$X_M/X_P = 1$
Geometric	$\left(\frac{L_h}{D}\right)_M \Big/ \left(\frac{L_h}{D}\right)_P = 1$
Boiling Number	$\left(\frac{q''}{G.h_{fg}}\right)_M \Big/ \left(\frac{q''}{G.h_{fg}}\right)_P = 1$

In this work, we adopt the fluid-to-fluid scaling approach so that the CHF LUT based on water can be utilized for predicting CHF in R-134a experiments.

3.3 Approach towards comparison

Liu experimental test section presented in Fig. 2-1 consists of a square duct with uniformly heated rod in the middle of duct. The CTF model consists of a single subchannel, a heat structure for the heater, and an adiabatic boundary at the test section exterior. A total of 28 test cases of Liu's experiments were run in CTF for different inlet conditions and heat flux values. Comparisons are also performed with three other CHF experimental databases. All three (Kim, Chun, and Pioro) CHF experiments consisted of simple tubular test section with uniformly heated tubes. Table 2-1 consists of experimental database and test runs for four selected CHF experimental datasets.

CTF version 4.0 allows user to choose the CHF predictions from Biasi, W-3, Bowring, and Groeneveld LUT (Groeneveld, et al., 2007) for water simulations. For this work, the correlations and LUT are modified to be suitable for R-134a. Code changes were implemented to include the Katto non-dimensional correlation and to add a fluid-to-fluid transformation to the CHF LUT.

The Katto's correlation (Katto, et al., 1984) includes boiling number, inlet sub-cooling enthalpy, inlet sub-cooling parameter, and latent heat of vaporization. The boiling

number and inlet sub-cooling parameter further are expressed in terms of Weber number, length to diameter ratio, and density ratio. The generalized version of Katto's correlation is as follows;

$$q_c = q_{co}\left(1 + K\frac{\Delta H_i}{H_{fg}}\right) \quad (5)$$

In terms of the fluid-to-fluid scaling of the CHF LUT the scaling was performed in two steps. Firstly, the density ratio, mass flux, surface tension, saturated liquid density, and latent heat of evaporation of R-134a were scaled to that of water at each node in the test section. The equations used for scaling these parameters are mentioned in Table 3-1.

Second, the equivalent water-based CHF values are obtained from LUT based on these scaled local conditions. Finally, water CHF values were scaled back to R-134a conditions using the boiling number scaling parameter.

CHF simulations were performed by slowly increasing the heat flux in CTF from a low value up to the time where CHF was predicted. For each test the critical power, flow and quality at the onset of CHF were recorded and compared to experimental results.

3.4 Two-phase flow correlations

In order to provide R-134a specific predictions the other two-phase flow correlation options in CTF were reviewed for applicability. In CTF, the user can select the Chen or Thom correlation for nucleate boiling heat transfer. In this study, the Chen correlation is selected as it is non-dimensional, whereas Thom correlation is specific to water as working fluid.

CTF uses Basu and Zuber-Saha model for projection of ONB and OSV location, respectively. Reviewing these models they were found suitable for R-134a application (Salko, et al., 2019).

4 Results

Two CHF prediction methods were applied into CTF for Liu's experiment and the results were compared with the experimental results in Fig 4-1. The results by LUT lie within bounds of ±15% whereas Katto's correlation under predicts the results. The LUT results show good agreement with Liu's experiment considering they are based on scaled look-up table entries for water. This is consistent with other literature which shows that the scaled CHF LUT predictions provide good

agreement with R-134a experimental data (Pioro, et al., 2001).

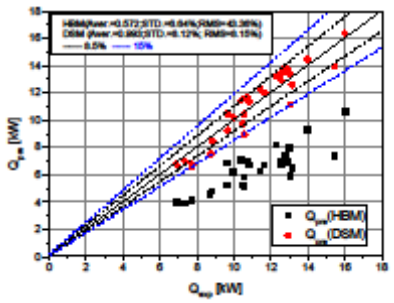

Figure 4-1 Comparison of predicted critical power using HBM and DSM CHF prediction methods with Liu's experiment

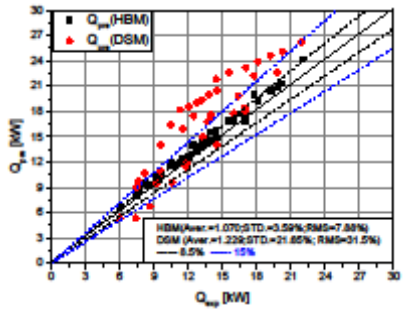

Figure 4-2 Comparison of predicted critical power using HBM and DSM prediction methods with Kim's experiment.

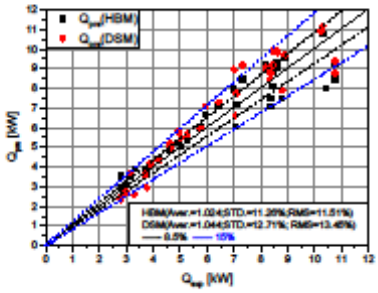

Figure 4-3 Comparison of predicted critical power HBM and DSM CHF prediction methods with Chun's experiment

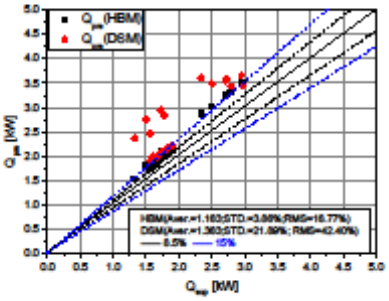

Figure 4-4 Comparison of predicted critical power using HBM and DSM CHF prediction methods with Pioro's experiment

Fig. 4-2 shows the CTF predicted and experimental critical powers for Kim's experiment. The CHF prediction by Katto's correlation lie within bounds of ± 8.5%. This good agreement is as Katto's correlation covers both DNB and annular film dry-out regimes in uniformly heated tubes. The LUT over predicts Kim's CHF experimental results. It is unclear why the LUT has a

positive bias for these tests, but one notable difference in this experiment is the quality at CHF is much greater than Liu's and Chun's experiments.

Fig 4-3 shows the CTF predicted and experimental critical powers for Chun's experiment. The CHF prediction by Katto's and LUT is in a good agreement (± 15%) with experimental results.

Fig 4-4 shows the CTF predicted and experimental critical powers for Pioro's experiment. The CHF prediction by Katto's correlation is within bounds of ± 15%.

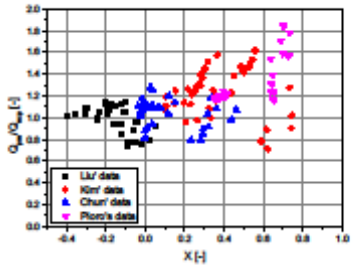

Figure 4-5 Q_{pre}/Q_{exp} vs. thermodynamic quality using LUT methods with four experiments

Figure 4-5 shows the trend of Q_{pre}/Q_{exp} with respect to thermodynamic quality (X) for the four experimental datasets using the LUT prediction method. It can be seen that as the thermodynamic quality increases and approaches the annular flow (X ~ 0.6), the dispersion of LUT Q_{pre}/Q_{exp} prediction from unity increases significantly and tends to over predict CHF. Further investigation of this trend with critical quality is required.

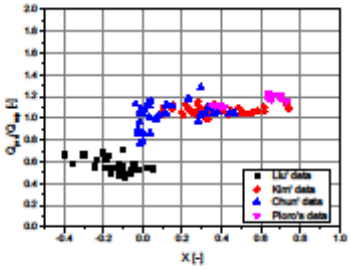

Figure 4-6 Q_{pre}/Q_{exp} vs. thermodynamic quality using Katto's correlation with four experiments

Figure 4-6 shows the trend of Q_{pre}/Q_{exp} with respect to thermodynamic quality (X) for the four experimental datasets using the Katto's correlation. It can be seen that the Katto's correlation has smaller prediction dispersion for different databases, especially tubular test sections, which shows better consistency. The underestimation of the Liu' data is due to the fact that the Katto's correlation does not take into account the cold wall effect for the specific annular geometry in Liu's experiment.

Table 4-1 Critical power statistical analysis with four experiments using Katto's correlation

Experiment	Mean Error [%]	STD [%]	RMS [%]
Liu,et al.	-42.9	6.64	43.38
Kim,et al.	7.0	3.59	7.88
Chun,et al.	2.4	11.26	11.51
Pioro,et al.	16.3	3.86	16.77

Table 4-2 Critical power statistical analysis with four experiments using LUT CHF prediction method

Experiment	Mean Error [%]	STD [%]	RMS [%]
Liu,et al.	-2.0	12.56	12.72
Kim,et al.	22.9	21.65	31.50
Chun,et al.	4.4	12.71	13.45
Pioro,et al.	36.3	21.89	42.40

5 Conclusions

This study focuses on incorporation of R-134a fluid properties in subchannel code CTF and its CHF prediction comparison with four different CHF experimental datasets. R-134a fluid properties were successfully added in CTF and the implementation was verified over the range of conditions expected in R-134a experiments. For CHF predictions two methods were implemented in CTF: a) Katto's correlation (HBM) b) the scaled 2006 CHF LUT (DSM). The predicted CHF results using each method were compared with four different CHF experimental results.

The result shows that the Katto's correlation performs well for Kim's, Chun's, and Pioro's CHF experiments. This is due to the fact that Katto's correlation covers both the DNB and dry-out regimes. While Katto's correlation under predicts CHF for Liu's experiment. Katto's correlation does not take into account the cold wall effect for the specific annular geometry in Liu's experiment and hence the difference are understood.

The LUT CHF predictions for most of the R-134a experimental data were good, however there was a trend to over predict with increasing local quality (observed mostly in the test data from (Kim, et al., 2005) and (Pioro, et al., 2001)). Further investigation using a larger experimental database is planned.

6 Nomenclature

Symbol		Units
A/B/C/V,/Y	Process fitting coefficients	/
Bo	boiling number ($Bo=q_0/h_{fg}/G$)	/
D	diameter of tube or bundle	M

D_e	hydraulic equivalent diameter	M
G	mass flux	kg/m^2s
H_f	saturated liquid enthalpy	kJ/kg
H_g	saturated vapor enthalpy	kJ/kg
H_{fg}	latent heat of evaporation	kJ/kg
ΔH_i	inlet subcooling enthalpy	kJ/kg
K	coefficient in Katto & Ohno correlation	/
LUT	Look-up Table	/
L_h/L	heated Length	m
P	pressure	psia/bar
P_{sat}	saturated pressure	psia
q_c	calculated CHF value	kW/m^2
q_{ref}	reference CHF value in Katto & Ohno correlation	kW/m^2
q_{CHF}	CHF value	kW/m^2
q_{exp}	experimental CHF value	kW/m^2
RMS	root-mean-square	/
SD	standard deviation	/
v_f	liquid specific volume	m^3/kg
v_g	vapor specific volume	m^3/kg
X_e	thermodynamic equilibrium quality	/
We	Weber number($We = G^2D/\rho\sigma$)	/
ρ_f	saturated liquid density	kg/m^3
ρ_g	saturated vapor density	kg/m^3
σ	surface tension	N/m

7 Acknowledgments

We would like to thank Dr. Robert Salko for his invaluable help and guidance with CTF.

8 References

Ahmad S Y Fluid to fluid mmodeling of critical heat flux: A compensated distortion model [Journal]. - [s.l.] : International Journal of Heat and Mass Transfer, 1972. - Vol. 16.

Carver M. B. [et al.] VALIDATION OF THE ASSERT SUBCHANNEL CODE: PREDICTION OF CRITICAL HEAT FLUX IN STANDARD AND NONSTANDARD CANDU BUNDLE GEOMETRIES [Journal]. - [s.l.] : HEAT TRANSFER AND FLUID FLOW, 1995. - Vol. 112.

Chun Se-Young [et al.] Comaprison of the CHF data for water and refrigerant HFC-134a by using the fluid-to-fluid modeling methods [Journal]. - [s.l.] : International Journal of Heat and Mass Transfer, 2007. - 21-22 : Vol. 50.

Groeneveld D C [et al.] The 2006 CHF look-up table [Journal]. - [s.l.] : Nuclear Engineering and Design, 2007. - 15-17 : Vol. 237.

Groeneveld D C On the definition of critical heat flux margin [Journal]. - [s.l.] : Nuclear Engineering and Design, 1996. - Vol. 163.

Katto Y A generalized correlation of critical heat flux for the forced convection boiling in vertical uniformly heated round tubes [Journal]. - [s.l.] : International Journal of Heat and Mass Transfer, 1978. - 12 : Vol. 21.

Katto Y. and Ohno H. An improved version of the generalize correaltion of critical heat flux for the force convective boiling in uniformly heated vertical tubes [Journal]. - [s.l.] : Int. J. Heat and Mass Transfer , 1984. - Vol. 27.

Kim Chang Ho, Bang In Cheol and Chang Soon Heung Critical heat flux performance for flow boiling of R-134a in vertical uniformaly heated smooth tube and rifled tubes [Journal]. - [s.l.] : International Journal of Heat and Mass Transfer, 2005. - 14 : Vol. 48.

Leung L K.H [et al.] Critical Heat Flux and Pressure Drop For a CANFLEX Bundle String Inside an Axially Non-Uniform Flow Channel [Conference] // 6th International Conference on CANDU Fuel. - Niagara Falls : [s.n.], 1999. - Vols. AECL-CONF-1199.

Liu Yang [et al.] A mechanistic bubble crowding model for predicting critical heat flux in subchannels of a bundle [Journal]. - Xi'an : Annals of Nuclear Energy, 2019. - Vol. 137.

Liu Yang [et al.] Critical heat flux measurement and visualization in R-134a on vertical singl rod with and without mixing-vane spacer: The characteristics and phenomenon of critical heat flux [Journal]. - [s.l.] : Annulas of Nuclear Energy, 2021. - Vol. Under Review.

Pioro I L [et al.] Comparison of CHF measurements in R-134a coled tubes and the water CHF look-up table [Journal]. - [s.l.] : International Journal of Heat and Mass Transfer, 2001. - 1 : Vol. 44.

Quiben Jesus Moreno and Thome John R Flow pattern based two-phase frictional pressure drop model for horizontal tubes, Part II: New phenomenological model [Journal]. - [s.l.] : International Journal of Heat and Fluid Flow, 2007. - 5 : Vol. 28.

Salko R [et al.] CTF 4.0 Theory Manual [Report]. - [s.l.] : CASL-A DOE Energy Innovation Hub, 2019.

Salko R [et al.] Development of preliminary VERA-CS crud-induced localized corrosion modeling capability [Conference] // International Topical Meeting on Advances in Thermal Hydraulics 2018. - Orlando : American Nuclear Society, 2018.

Shah M Mohammaed Improved general correlation for critical heat flux during upflow in uniformly heated vertical tubes [Journal]. - [s.l.] : Heat and Fluid Flow, 1987. - 4 : Vol. 8.

Son Gyumin and Bang In Cheol R134a flow boiling analysis with modified thermodynamic property file of MARS code [Conference] // Transactions of the Korean Nuclear Society Autun Meeting. - Gyeongju : Korea Nuclear Society, 2016.

U.S Department of Commerce NIST: National Institute of Standards and Technology [Online]. - 2021. - https://www.nist.gov/.